

INVESTIGATION OF DYNAMIC BEHAVIOR OF ALUMINUM ALLOY  
ARMOR MATERIALS

A THESIS SUBMITTED TO  
THE GRADUATE SCHOOL OF NATURAL AND APPLIED SCIENCES  
OF  
MIDDLE EAST TECHNICAL UNIVERSITY

BY

MEHMET MACAR

IN PARTIAL FULFILLMENT OF THE REQUIREMENTS  
FOR  
THE DEGREE OF DOCTOR OF PHILOSOPHY  
IN  
MECHANICAL ENGINEERING

SEPTEMBER 2014



Approval of the thesis:

**INVESTIGATION OF DYNAMIC BEHAVIOR OF ALUMINUM ALLOY  
ARMOR MATERIALS**

submitted by **MEHMET MACAR** in partial fulfillment of the requirements for the degree of **Doctor of Philosophy in Mechanical Engineering Department, Middle East Technical University** by,

Prof.Dr. Canan Özgen  
Dean, Graduate School of **Natural and Applied Sciences** \_\_\_\_\_

Prof.Dr. Suha Oral  
Head of Department, **Mechanical Engineering** \_\_\_\_\_

Prof.Dr. R.Orhan Yıldırım  
Supervisor, **Mechanical Engineering Dept., METU** \_\_\_\_\_

Assoc.Prof.Dr.Murat Vural  
Co-supervisor, **Mechanical, Materials & Aerospace Eng. Dept., IIT** \_\_\_\_\_

**Examining Committee Members:**

Prof. Dr. Metin Akkök  
Mechanical Engineering Dept., METU \_\_\_\_\_

Prof. Dr. R.Orhan Yıldırım  
Mechanical Engineering Dept., METU \_\_\_\_\_

Prof. Dr. Bilgehan Ögel  
Metallurgical and Materials Engineering Dept., METU \_\_\_\_\_

Prof. Dr. Ömer Anlağan  
Mechanical Engineering Dept., Bilkent University \_\_\_\_\_

Assoc.Prof.Dr. Lütfullah Turanlı  
Civil Engineering Dept., METU \_\_\_\_\_

Date: 04 September 2014

**I hereby declare that all information in this document has been obtained and presented in accordance with academic rules and ethical conduct. I also declare that, as required by these rules and conduct, I have fully cited and referenced all material and results that are not original to this work.**

Name, Last Name: MEHMET MACAR

Signature :

## **ABSTRACT**

### **INVESTIGATION OF DYNAMIC BEHAVIOR OF ALUMINUM ALLOY ARMOR MATERIALS**

Macar, Mehmet

Ph.D., Department of Mechanical Engineering

Supervisor :Prof. Dr. R. Orhan Yıldırım

Co-Supervisor :Assoc.Prof.Dr. Murat Vural

September 2014, 152 pages

The main objective of this research is to investigate the dynamic behavior of aluminum alloys (such as 5083-H131, 7039-T64 and 2139-T8) commonly used in lightweight armored military vehicles in a comparative manner and establish a robust experimental database as well as constitutive models for their dynamic response over a wide range of strain rates and temperatures typically encountered in penetration and impact events.

Unlike quasi-static deformation processes, impact and dynamic penetration events often involve high strain rates, large strains and rapid changes in temperature due to severe thermoplastic heating and adiabatic deformation conditions. Therefore, any reliable simulation and/or design of armor systems require the development of rate and temperature dependent predictive constitutive models that heavily rely on extensive experimentation at high strain rates and elevated temperatures.

In the first phase of study, high strain rate experiments were conducted by using split-Hopkinson pressure bar (SHPB) apparatus at both room temperature and elevated temperatures to understand and document the constitutive behavior of

selected aluminum alloys. Quasi-static experiments were also conducted to establish a basis for comparison and more comprehensive analysis of the constitutive response. Then, building on the experimental results and observations, the competition between strain hardening, strain rate hardening and thermal softening mechanisms were evaluated for each alloy to develop a comprehensive analysis of their dynamic deformation and failure behavior. In the second phase, the emphasis was placed on developing predictive constitutive models and finding the model parameters. Both phenomenological (Johnson-Cook, Modified Johnson-Cook) and physics based (Zerilli-Armstrong, Modified Zerilli-Armstrong, Turkkan-Vural Modified Zerilli-Armstrong) models were utilized and their performances were evaluated. According to these results, a new modified model was proposed by combining Modified Johnson-Cook and Turkkan-Vural Modified Zerilli-Armstrong models depending on their ability in capturing the experimental data. The new proposed model eliminates the weakness of the existing models and fits the experimental data better, especially at elevated temperatures.

This study has also led to an advanced understanding of aluminum alloy armor materials' tendency to shear localization in the form of adiabatic shear banding (ASB) by using shear-compression specimens (SCS) in controlled dynamic experiments followed by detailed microstructural examination.

**Keywords:** High Strain Rate, Dynamic Behavior, Constitutive Modeling, Aluminum Alloy Armor, Split Hopkinson Pressure Bar, Kolsky Bar, Impact Mechanics

## ÖZ

### ALÜMİNYUM ALAŞIMLI ZIRH MALZEMELERİNİN DİNAMİK DAVRANIŞLARININ İNCELENMESİ

Macar, Mehmet

Doktora, Makina Mühendisliği Bölümü

Tez Yöneticisi :Prof. Dr. R. Orhan Yıldırım

Ortak Tez Yöneticisi :Doç.Dr. Murat Vural

Eylül 2014, 152 sayfa

Bu tez çalışmasının ana amacı, hafif zırhlı araçlarda yaygın kullanılan alüminyum alaşımlı zırh malzemelerinin (5083-H131, 7039-T64 and 2139-T8 gibi) karşılaştırmalı olarak dinamik davranışını incelemek, zırhın penetrasyonunda meydana gelen gerinim hızlarında ve sıcaklıklarında söz konusu malzemelerin dinamik davranışının belirlenmesi amacıyla bünye modelleri ile birlikte doğrulanmış deneysel veri tabanı oluşturmaktır.

Yarı statik deformasyonlardan farklı olarak, yüksek gerinim hızlarına neden olan darbe ve dinamik penetrasyon olaylarında çarpışma esnasında oluşan adiyabatik deformasyona bağlı termoplastik ısınmadan dolayı ani yüksek sıcaklıklar ve yüksek gerinimler oluşur. Bundan dolayı güvenilir simülasyon ve/veya zırh sistem tasarım yazılımları, yüksek gerinim hızlarında ve yüksek sıcaklıklarda yapılmış ayrıntılı deneysel sonuçlara dayanan bünye modellerinin geliştirilmesine gereksinim duyar.

Söz konusu çalışmanın birinci aşamasında, seçilen alüminyum zırh malzemelerinin yüksek gerinim hızında deneyleri, bünye davranışını anlamak ve dokümanete etmek için hem oda hem de yüksek sıcaklıklarda Split Hopkinson Basınç Çubuğu (SHPB) deney düzeneği kullanılarak yapılmıştır. Malzemelerin dinamik davranışının daha

kapsamlı analiz edilmesi ve karşılaştırılması için temel teşkil edecek yarı statik gerinim hızlarında da deneyler yapılmıştır. Böylece, deneysel sonuçlara ve gözlemlere dayanarak, gerinim sertleşmesi, gerinim hızı sertleşmesi ve termal yumuşama mekanizmaları her bir malzeme için ayrı ayrı değerlendirilerek dinamik deformasyonları ayrıntılı bir şekilde analiz edilmiştir. İkinci aşamada ise bünye modelleri geliştirmek ve model parametrelerini bulmak üzerine yoğunlaşmıştır. Bu çerçevede, hem fenomenolojik (Johnson-Cook, modified Johnson-Cook) hem de fiziksel tabanlı (Zerilli-Armstrong, Modified Zerilli-Armstrong, Turkkan-Vural Modified Zerilli-Armstrong) modeller kullanılmış ve bunların performansı değerlendirilmiştir. Ayrıca, bu modellerin eksiklikleri ve zayıf yönleri tespit edilmiştir. Bunun sonucunda deneysel verilerle uyumlu olan ve bu modellerin yüksek sıcaklıklardaki eksik yönlerini gideren yeni bir model önerisi yapılmıştır.

Bu çalışmada aynı zamanda, alüminyum alaşımlı zırh malzemelerinden basınç altında kayma gerilmesi numuneleri (SCS-Shear Compression Specimen) hazırlanmış, bu numunelerin kontrollü dinamik deneyleri yapılmış, belirli gerinimlerde dinamik deformasyona maruz kalmış bu numunelerin mikroyapıları incelenmiş ve bu malzemelerde adiyabatik kayma bandlarının oluşum eğilimi belirlenmiştir.

Anahtar Kelimeler: Yüksek Gerinim Hızı, Dinamik Davranış, Bünye Modelleme, Alüminyum Alaşımlı Zırh, Split Hopkinson Basınç Çubuğu, Kolsky Çubuğu, Darbe Mekaniği



To the mirror of my soul ,  
my daughter, Esra,  
my son, Kemal,  
junior Mehmet,  
and my parents.

## ACKNOWLEDGMENTS

I would like to thank my supervisor, Professor Orhan Yıldırım for his knowledge, guidance and support during my graduate studies starting from 2006 to the end of my thesis and also for giving me the opportunity to study in Illinois Institute of Technology (IIT) as a visitor researcher. I am so grateful to my co-supervisor, Professor Murat Vural for giving me a chance to study as a visitor researcher as part of his research group and his knowledge, guidance and support during my graduate studies.

I would like to thank Dr. Celal Evcı for his guidance, support and help in developing the test method employed in this work and for doing a countless number of high strain rate testing and installing strain gauges. He also helps me in various experiments including quasi-static and microstructure observation while we have many difficulties during finding a proper etching method for different type of alloys. He puts his deepest and friendship effort during my research period in IIT.

Thanks to Omer Anıl Turkkın for his help in understanding various aspects of the split Hopkinson bar and in developing a method for calibration of constitutive models. A special thanks to Dr. Satya Emani for his invaluable support in my metallographic work. I am grateful to laboratory technicians, including Russell Janota for his guidance in setting up and maintaining complex testing apparatuses, and Craig Johnson, in machining specimens for my experiments.

I also thank TUBITAK and TLFC for aiding me financially during my research period as a visitor researcher at IIT.

And finally and most especially, thank you to my wife Sema, my daughter Esra, my son Kemal and junior Mehmet. They gave their full support and understanding to me during my local and abroad study. Lastly, I don't think this would have been possible without their invokes of my mother, Gülizar and my Father, Mehmet.

## TABLE OF CONTENTS

ABSTRACT.....	v
ÖZ .....	vii
ACKNOWLEDGMENTS.....	x
TABLE OF CONTENTS .....	xi
LIST OF TABLES .....	xiv
LIST OF FIGURES.....	xv
LIST OF SYMBOLS .....	xx
LIST OF ABBREVIATIONS .....	xxiii
CHAPTERS .....	1
1. INTRODUCTION.....	1
2. THEORITICAL BACKGROUND.....	11
2.1 High Strain Rate (Dynamic) Deformation .....	11
2.1.1 Thermally Activated Dislocation Motion .....	15
2.1.2 Dislocation Drag Mechanism.....	17
2.1.3 Adiabatic Shear Localization .....	19
2.2 High Strain Rate (Dynamic) Experiments .....	23
2.2.1 Split Hopkinson Pressure Bar (SHPB).....	23
2.2.2 Shear Compression Specimen (SCS).....	32
2.3 Material Modeling.....	33
2.3.1 Phenomenological (Empirical) Models.....	34
2.3.2 Physically Based Models .....	38
2.3.2.1 Zerilli-Armstrong (ZA) Model.....	42
3. EXPERIMENTAL WORK.....	51
3.1 Materials.....	51

3.2 Aluminum Alloys .....	53
3.3 Test Specimens.....	55
3.4 Uniaxial and Shear Compression Loading Experiments.....	57
3.4.1 Quasi-static Loading Experiments .....	58
3.4.2 High Strain Rate Experiments .....	62
3.4.3 Instrumentation.....	63
3.4.4 Constructing Dynamic Stress-Strain Plots from SHPB Data.....	65
3.5 Metallographic Preparation and Etching of Aluminum Alloys .....	68
3.6 Test Matrix .....	69
4. EXPERIMENTAL RESULTS .....	71
4.1 Quasi-static and Dynamic Experimental Results and Discussion.....	71
4.1.1 Quasi-static Experiments.....	71
4.1.2. Dynamic (High Strain Rate) Experiments .....	81
4.2 Propensity to Adiabatic Shear Localization .....	89
4.2.1 Occurrence of adiabatic shear band (ASB).....	89
4.2.2 Parameter Fitting for SCS Dynamic Experiments .....	90
4.2.3 SCS Dynamic Experiments .....	93
4.3 Microstructural Observation .....	98
5. CALIBRATION OF MATERIAL MODELS.....	103
5.1 Phenomenological (Engineering or empirical) Constitutive Models.....	104
5.1.1 Johnson-Cook (JC) Model .....	104
5.1.2 Modified Johnson-Cook (MJC) Model.....	109
5.2 Physical based Constitutive Models.....	113
5.2.1 Zerilli-Armstrong (ZA) Model.....	113
5.2.2 Modified Zerilli-Armstrong (MZA) Model .....	116
5.2.3 Turkkan -Vural Modifications to MZA (TVMZA) Model .....	120
5.2.4 Proposed Model by combining MJC and TVMZA Model .....	124
6. SUMMARY AND CONCLUSIONS.....	133
6.1 Quasi-static and High Strain Rate Experiments .....	133
6.2 Constitutive Modeling.....	136
6.3 Adiabatic Shear Localization .....	137

6.4 Concluding Remarks .....	139
7. RECOMMENDATIONS FOR FUTURE WORK.....	141
REFERENCES.....	143
CIRRICULUM VITAE.....	152

## LIST OF TABLES

### TABLES

Table 3.1 Chemical compositions of aluminum alloys (values in wt.%).....	52
Table 3.2 Mechanical properties of aluminum alloys .....	52
Table 3.3 Major alloying elements and strengthening mechanisms .....	52
Table 3.4 Basic temper designations per ANSI H.35.1 standard .....	53
Table 3.5 Basic temper designations per ANSI H.35.1 . .....	54
Table 3.6 Basic temper designations per ANSI H.35.1 . .....	54
Table 3.7 Double Etching Composition and Procedure .....	69
Table 3.8 Test Matrix (Number of experiments carried out) .....	70
Table 4.1 Thermal softening rates, thermal and athermal flow stresses .....	75
Table 4.2 The flow stress at various strain rate and 10% offset strain.....	82
Table 4.3 Compression dynamic flow stress at 220 °C and 10% offset strain.....	86
Table 4.4 Comparison of critical strains, stresses and softening rates obtained from SCS experiments of 5083, 7039, 2519 and 2139. Note that all specimens had the same gage width (w=0.1 in) and were tested at the same strain rate ( $5 \times 10^3 \text{ s}^{-1}$ ) and temperature (RT).....	94
Table 4.5 Pre-determined strain values for SCSs for each alloy with respect to three distinct stages.....	97
Table 5.1 JC Material Model Parameters for 5083 and 2139 Alloys.....	106
Table 5.2 MJC Material Model Parameters for 5083 and 2139 Alloys .....	110
Table 5.3 ZA Material Model Parameters for 5083 and 2139 Alloys.....	114
Table 5.4 MZA Material Model Parameters for 5083, and 2139 Alloys .....	117
Table 5.5 TVMZA Material Model Parameters for 5083and 2139 Alloys.....	121
Table 5.6 Parameters of Proposed Model for 5083, 7039, 2519 and 2139 Alloys .	127
Table 5.7 Coefficient of drop in flow stress in dynamic regime.....	131

## LIST OF FIGURES

### FIGURES

Figure 1.1 Milne and de Marre Graph .....	2
Figure 1.2 (a) M113 APC having 5083 structure (b) Scorpion Combat Vehicle having 7039 structure (c) The Bradley Fighting Vehicle having both 7039 (upper half) and 5083 (lower half) (d) Expeditionary Fighting Vehicle (EFV) having 2519 structure. ....	4
Figure 1.3 Microstructure of (a) 5083 (b) 7039 (c) 2519 (d) 2139 aluminum alloys. ....	6
Figure 1.4 Strength and Ballistic Performance of 1 inch thick AA2139-T8 plate as compared to other aluminum armor alloys .....	6
Figure 1.5 Stress-strain curves for depleted uranium at strain rates of $5000 \text{ s}^{-1}$ and $0.001 \text{ s}^{-1}$ .....	8
Figure 2.1 Effects of temperature and strain rate on the yield stress of iron. ....	13
Figure 2.2 Three Regions of Strain Rate Sensitive Behavior for En3B Steel. The labels and vertical dashed lines were added by [22]. ....	14
Figure 2.3 Flow stress measurements (compression) at $\epsilon = 0.15$ in OFE copper as a function of strain rate. ....	14
Figure 2.4 Peierls-Nabarro force: applied stress vs. distance. ....	15
Figure 2.5 (a) Thermal energy needed to overcome short range obstacles (b) Stress as a function of temperature needed to overcome obstacles. ....	16
Figure 2.6 Schematic of a long-range obstacles overcome by a dislocation on its way .....	17
Figure 2.7 Failure modes of material subjected to high velocity impact. ....	20
Figure 2.8 (a) Optical metallographic views of ASB formation and incipient plug [36] (b) Plug formation in penetration of 5083 by 20 mm FSP .....	21
Figure 2.9 A typical stress-strain curve showing the three stages of plastic deformation. ....	21
Figure 2.10 Geometry of a hat-shaped specimen .....	22

Figure 2.11 A schematic of SHPB set-up. ....	24
Figure 2.12 Stress wave propagation on striker and incident bars of SHPB just after impact.....	24
Figure 2.13 Propagation of an elastic compressive wave in a thin cylindrical bar ...	25
Figure 2.14 Stress wave propagation in the striker bar of SHPB.....	28
Figure 2.15 Stress wave propagation on incident bar of SHPB .....	29
Figure 2.16 Stress wave propagation on incident bar, specimen and transmitted bar of SHPB after impact of incident bar on specimen.....	29
Figure 2.17 Effect of temperature on the rate sensitivity of flow stress at 0.2% and 5% offset for AA 2139-T8. Solid lines are the predictions of MJC model. ....	37
Figure 2.18 Shear produced by passage of (a) a dislocation (b) dislocation array . .	38
Figure 2.19 Different shapes of barriers: rectangular, hyperbolic, and sinusoidal ..	40
Figure 3.1 Test specimens cut from plate in rolling direction .....	55
Figure 3.2 Specimens used in experiments (a) cylindrical compression specimen and shear compression specimen (SCS). All dimensions are in inches (b) A picture of samples specimens of all kinds with different aspect ratios and gage widths. ....	56
Figure 3.3 A view of stop rings (a) alone (b) installed on SHPB (c) sketch.....	57
Figure 3.4 MTS 793 Servo Hydraulic test machine with installed heating chamber. ....	59
Figure 3.5 Repeatability check results of MTS 793 Servo Hydraulic Machine .....	59
Figure 3.6 Specimen and silicone O-ring configuration to attach the thermocouple to the specimen.....	60
Figure 3.7 A view of SHPB at Dynamic Testing Laboratory of IIT.....	63
Figure 3.8 Wheatstone half- bridge.....	64
Figure 3.9 Raw and filtered stress wave data recorded by digital oscilloscope.....	66
Figure 3.10 Stress waves after time shifting and filtering raw data obtained from digital oscilloscope .....	66
Figure 3.11 (a) True stress-true strain curves after analysis (b) Time resolved evaluation of strain rate and strain .....	67



Figure 3. 12 Tools used in metallographic preparation and etching of aluminum alloys (a) grinding (b) polishing (c) etching (d) inverse metal optical microscopy .....	68
Figure 4.1 True stress-true strain curves at various temperatures at a reference strain rate of $10^{-3} \text{ s}^{-1}$ for 5083, 7039, 2519 and 2139 .....	73
Figure 4.2 Flow stresses of 5083, 7039, 2519 and 2139 alloys as a function of temperature at 10% offset plastic strain at a strain rate of $10^{-3} \text{ s}^{-1}$ . .....	74
Figure 4.3 Flow stress of an idealized material as a function of temperature; thermal and athermal components of stress indicated.....	76
Figure 4.4 True stress-true strain curves of aluminum alloys at low strain rates ( $10^{-3}$ - $10^0 \text{ s}^{-1}$ ) at RT (room temperature) for 5083, 7039, 2519 and 2139.....	77
Figure 4.5 True stress-strain curves for aluminum alloys at low strain rates ( $10^{-3}$ - $10^0 \text{ s}^{-1}$ ) and at elevated temperature ( $220 \text{ }^{\circ}\text{C}$ ).....	80
Figure 4.6 The influence of temperature and strain rate on the yield and strain hardening of pure FCC materials such as Ni, Al, and Cu. ....	81
Figure 4.7 Dynamic compression true stress-true strain curves of 5083, 7039, 2519 and 2139 at strain rates of ( $10^2$ - $10^4 \text{ s}^{-1}$ ) at RT, full scale (left) and low strain (right) .....	83
Figure 4.8 Dynamic stress-strain curves for 5083, 7039, 2519 and 2139 for strain rates ( $10^2$ - $10^4 \text{ s}^{-1}$ ) at a temperature of $220 \text{ }^{\circ}\text{C}$ , full scale (left) and low strain (right).....	85
Figure 4.9 Variation of flow stress 10% offset strain with strain rate at both RT and $220 \text{ }^{\circ}\text{C}$ for 5083, 7039, 2519 and 2139.....	88
Figure 4.10 Calibration experiments to determine fitting parameters for 5083, 7039, 2519 and 2139 .....	91
Figure 4.11 A Typical shear localization curve showing the three stages of shear deformation .....	93
Figure 4.12 Shear localization curves of 5083, 7039, 2519 and 2139 .....	95
Figure 4.13 Dynamic experiment result with stop rings embedded on shear localization curves for 5083, 7039, 2519 and 2139 .....	96
Figure 4.14 Microstructural image (a) a complete view (b) a detail section .....	99
Figure 4.15 Evolution of localized shear band for 5083.....	100

Figure 4.16 Evolution of localized shear band for 7039 .....	100
Figure 4.17 Evolution of localized shear band for 2519 .....	101
Figure 4.18 Evolution of localized shear band for 2139 .....	101
Figure 5.1 Flow stress as a function of temperature for 5083 and 2139 at 10% offset strain and at a strain rate of $10^{-3} \text{ s}^{-1}$ : experimental data versus the prediction of JC model .....	106
Figure 5.2 Flow stress versus plastic strain for 5083 and 2139 at different temperatures and at a strain rate of $10^{-3} \text{ s}^{-1}$ : experimental data (solid lines) versus the predictions of JC model (dashed lines) .....	107
Figure 5.3 Flow stress at 10% offset strain versus strain rate for 5083 and 2139 alloys at both RT and elevated temperature: experimental data versus the prediction of JC model. ....	107
Figure 5.4 Flow stress versus plastic strain for 5083 and 2139 at different strain rates and temperatures: experimental data versus the prediction of JC model.....	108
Figure 5.5 Flow stress as a function of temperature for 5083 and 2139 at 10% offset strain and at a strain rate of $10^{-3} \text{ s}^{-1}$ : experimental data versus the prediction of MJC model.....	110
Figure 5.6 Flow stress versus plastic strain for 5083 and 2139 at different temperatures and at a strain rate of $10^{-3} \text{ s}^{-1}$ : experimental data (solid lines) versus the prediction of MJC model (dashed lines) .....	111
Figure 5.7 Flow stress at 10% offset strain versus strain rate for 5083 and 2139 alloys at RT and elevated temperature: experimental data versus the prediction of MJC model.....	111
Figure 5.8 Flow stress versus strain for 5083 and 2139 at different strain rates and RT and elevated temperature: experimental data versus the prediction of MJC model.....	112
Figure 5.9 Flow stress as a function of temperature for 5083 and 2139 at 10% offset strain and at a strain rate of $10^{-3} \text{ s}^{-1}$ : experimental data versus the prediction of ZA model .....	114
Figure 5.10 Flow stress at 10% offset strain versus strain rate for 5083 and 2139 alloys at RT and elevated temperature: experimental data versus the prediction of ZA model. ....	114

Figure 5.11 Flow stress versus strain for 5083 and 2139 at different strain rates and temperatures: experimental data versus the prediction of ZA model.....	115
Figure 5.12 Flow stress as a function of temperature for 5083 and 2139 at 10% offset strain and a strain rate of $10^{-3} \text{ s}^{-1}$ : experimental data versus the prediction of MZA model .....	117
Figure 5.13 Flow stress versus strain rate for 5083 and 2139 alloys at RT and elevated temperature: experimental data versus the prediction of MZA model .....	118
Figure 5.14 Flow stress versus strain for 5083 and 2139 at different strain rates and temperatures: experimental data versus the prediction of MZA model.....	118
Figure 5.15 Flow stress as a function of temperature for 5083 and 2139 at 10% offset strain and at $10^{-3} \text{ s}^{-1}$ : experimental data versus the prediction of TVMZA model.....	121
Figure 5.16 Flow stress at 10% offset strain versus strain rate for 5083 and 2139 alloys at RT and elevated temperature: experimental data versus the prediction of TVMZA model. ....	121
Figure 5.17 Flow stress versus strain for 5083 and 2139 at different strain rates and temperatures: experimental data versus the prediction of TVMZA model.....	122
Figure 5.18 Flow stress versus strain rate without considering thermal softening in dynamic regime .....	125
Figure 5.19 Flow stress at 10% offset strain as a function of temperature for 5083, 7039, 2519 and 2139 at a strain rate of $10^{-3} \text{ s}^{-1}$ : experimental data versus the prediction of combined MJC and TVMZA model.....	128
Figure 5.20 Flow stress at 10% offset strain versus strain rate for 5083, 7039, 2519 and 2139 alloys at RT and elevated temperature: experimental data versus the prediction of combined MJC and TVMZA model.....	128
Figure 5.21 Flow stress versus strain for 5083 and 2139 at different strain rates and temperatures: experimental data versus the prediction of combined MJC and TVMZA model. ....	130

## LIST OF SYMBOLS

### SYMBOLS

$A$	Cross-section of the bar, Thermal activation area
$A_0$	Initial cross-section area, Thermal activation area at $T=0$ K
$A(T)$	Material specific temperature dependent parameter
$a$	Lattice parameter
$B, B_0$	Strain hardening coefficient, Viscous damping coefficient
$b$	Burgers vector
$C$	Wave propagation speed, Strain rate sensitivity (SRS) parameter
$c$	Lattice spacing
$C_0$ and $C_1$	SRS parameter for quasi-static regime
$C_2$	SRS parameter for high strain rate regime, drop rate in strain rate hardening in dynamic regime due to the temperature effects
$D$	Diameter, Drop in flow stress
$d$	Average grain diameter
$e$	Engineering strain
$E$	Elastic (Young's) modulus
$f_v$	Viscous force
$f_0$	Vibrational frequency of the dislocation
$G$	Shear modulus
$\Delta G$	Thermal energy
$\Delta G_0$	Reference activation energy at $T=0$ K
$H(\dot{\epsilon}, \dot{\epsilon}_1, k)$	Heaviside step function
$k$	Microstructural stress intensity, scaling factor
$k_1$ and $k_2$	Constants
$L$	Length

$L_s$	Specimen length
$L_0$	Initial gage length
$l$	Distance traveled by each dislocation
$l^*$	Distance between the barriers, spacing of the forest dislocations
$M$	Orientation factor
$m$	Thermal softening parameters
$N$	Number of dislocations
$n$	Strain hardening exponent
$T$	Temperature
$T_m$	Melting temperature
$T_r$	Reference temperature
$T^*$	Homologous temperature
$t_w$	Waiting time in front of barrier
$t_m$	Moving time between the dislocations
$P$	Force
$R$	Resistance
$\Delta R$	Change of resistance
$S$	Engineering stress
$s^{-1}$	Per second
$u$	Displacement
$V_E$	Excitation voltage
$V_{data}$	Reading voltage from the oscilloscope
$v$	Velocity of the fluid, dislocation velocity, particle speed
$\theta$	Deflection angle
$\Omega$	Omega precipitate
$\beta$	Thermo-mechanical coupling strength
$B, B_0, \beta_0$ and $\beta_1$	Experimental parameters based on thermal dislocation mechanism of two different crystal lattice structures
$\delta x$	Length of the cross-section which the wave is passing through
$\varepsilon$	True strain

$\varepsilon_{eq}$	Equivalent strain
$\dot{\varepsilon}$	Strain rate
$\dot{\varepsilon}_t$	Transition strain rate
$\lambda$	Width of the barrier
$\kappa$	Boltzman's constant
$\rho$	Density of the bar, density of dislocation, probability that a dislocation will overcome a barrier
$\rho C$	Mechanical impedance of the material property
$\sigma$	True stress
$\sigma_0$	Yield stress
$\sigma_a$	Athermal flow stress
$\sigma_{eq}$	Equivalent stress
$\sigma_r$	Reference stress
$\sigma_R$	Reflected wave
$\sigma_I$	Incident wave
$\sigma_T$	Transmitted wave
$\sigma_s$	Stress increase due to solutes and
$\sigma^*$	Thermal flow stress
$\tau_{\tau h}$	Thermal component of the shear stress

## LIST OF ABBREVIATIONS

### ABBREVIATIONS

AA	Aluminum Alloy
Al	Aluminum
ANSI	American National Standards Institute
AP	Armor Piercing
APC's	Armor Personnel Carriers
ARL	Army Research Laboratory
ASB	Adiabatic Shear Band
ASM	American Society of Materials
BCC	Body Centered Cubic
CA	Cyanoacrylate
DSA	Dynamic Strain Aging
DRV	Dynamic Recovery
DRX	Dynamic Recrystallization
EFV	Expeditionary Fighting Vehicle
ET	Elevated Temperature
FCC	Face Centered Cubic
FE	Finite Element
FEA	Finite Element Analysis
FSP	Fragment Simulating Projectile
GF	Gage Factor
HCP	Hexagonal Close Packed
IIT	Illinois Institute of Technology
JC	Johnson Cook
LAV	Lightweight Armor Vehicle
LVDT	Linear Variable Differential Transducer
MJC	Modified Johnson Cook
MICV's	Mechanized Infantry Combat Vehicles

MZA	Modified Zerilli-Armstrong
nSRS	Negative Strain Sensitivity
TVMZA	Turkkan-Vural Modified Zerilli-Armstrong
PID	Proportional Integral Derivative
PLC	Portevin–Le Chatelier
RT	Room Temperature
SHPB	Split Hopkinson Pressure Bar
SCC	Stress Corrosion Cracking
SCS	Shear Compression Specimen
SRS	Strain Rate Sensitivity
ZA	Zerilli-Armstrong



## CHAPTER 1

### INTRODUCTION

Lightweight military vehicles such as personnel carriers and combat vehicles are being increasingly used to improve mobility and deployability of armed forces. High performance aluminum (Al) alloys are typically used in fabricating these vehicles to provide both structural strength and ballistic resistance against projectile and fragment impacts as well as blast loadings. To analyze and improve the performance of these alloys against threats in battle field requires a fundamental understanding and modeling of their dynamic deformation behavior.

Light armored vehicles (LAV's), being designed with air-transportability and air-droppability for rapid deployment, need to be fabricated from materials which should have as much thin thickness and low density as possible while providing ballistic protection against military threats in the field. In order to figure out a better protection/weight ratio, Milne and de Marre graph [1] given in Figure 1.1 is often used.

Milne and de Marre graph [1] shows the kinetic energy (KE) of penetration for various armor materials, plotting projectile energy to penetrate versus the thickness of the armor. Note that the scales are logarithmic and that thickness scale is stated in terms of areal density (the mass of 1 m<sup>2</sup> of the armor) [1].

According to the graph, at plate thickness greater than 25 mm “steel equivalent” that corresponds to 75 mm thick aluminum the same areal density, steel armor provides a better protection/weight ratio against KE impact than aluminum alloy armor materials. Therefore, steel armor is used for main battle tanks that need thicker armor plate for structural stiffness. However, at plate thickness below this crossover

point (75 mm for aluminum, 25 mm for steel), aluminum alloy armor materials are superior to steel since the projectile energy required to penetrate the aluminum alloy plates is higher. Therefore, aluminum alloy armor has a great advantage for LAV's such as armor personnel carriers (APC's) and mechanized infantry combat vehicles (MICV's). However, these vehicles provide ballistic resistance only against small arms, they have no protection against long rod penetrators and shaped charged warheads.

While pure aluminum is very soft, aluminum alloys can have a yield stress that easily compete with some of the steel alloys. Some strengthening mechanisms such as solid solution strengthening and age hardening have been developed to strengthen aluminum alloys. Although the range of strengths obtained in steels is very large, and there are no aluminum alloys that can be compared with the highest strength steels in terms of yield strength, as one considers the specific strength (that is, the strength per unit weight;  $\sigma_y/\rho$ ), some of the aluminum alloys can be very competitive [2].

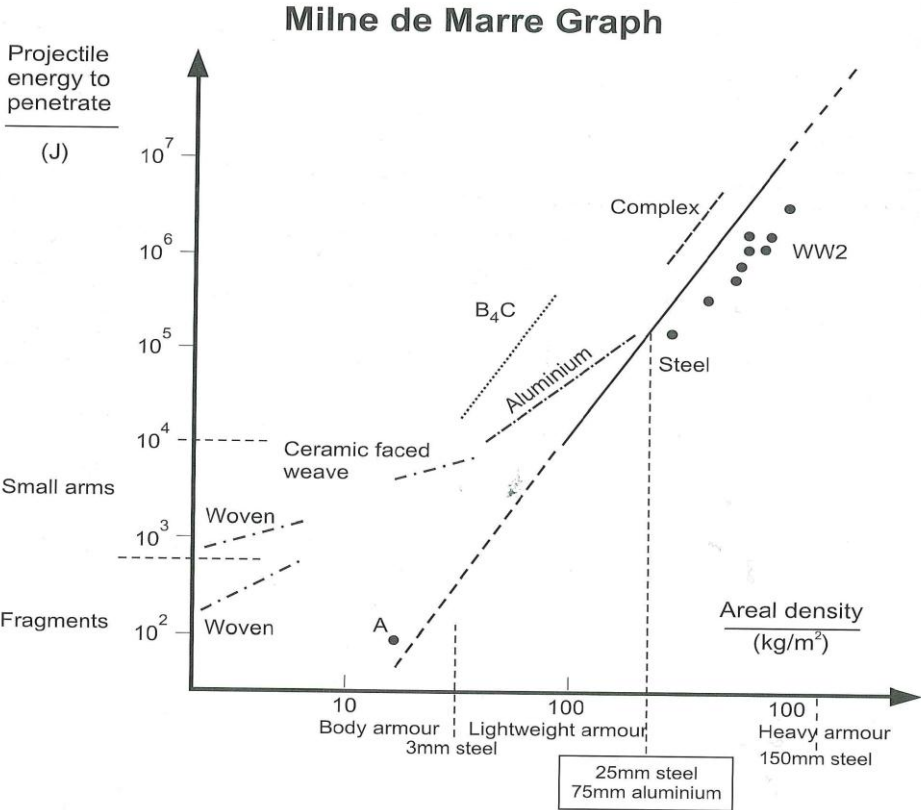


Figure 1.1 Milne and de Marre Graph [1]

Another critical question for choosing which metals meet both structural and ballistic performance in vehicles involves weldability, since it is more important in manufacturing of these vehicles on both production cost and maintenance. Although the welding technology of steels is well known and definite, the weldability of aluminum alloys is much more variable. Hence, the aluminum alloys that are easily weldable are preferred in armor applications, even if there is some decrease in terms of strength and ballistic performance [2].

A good optimization between weight, structural performance, ballistic performance, ease of production, and ease of maintenance (including resistance to corrosion) play a very significant role in the choice of alloy for vehicular applications. Aluminum alloys which have been used so far as armor material in combat vehicles are mainly AA5083, AA7039 and AA2519. Increasing threats in current operations have driven the development of new aluminum alloys for armor applications. Among all the aluminum alloys used in army applications, aluminum 2139-T8 has gained considerable attention and this alloy is extensively being studied in recent years due to its great potential for improved mechanical properties such as higher strength, fracture toughness and fatigue life and high impact performance [2-4]. New commercial alloy, aluminum 2139 with significant strength (around 600 MPa at high strain rates) and reasonable ductility has a significant potential for future combat vehicles [2].

The American M113 APC in Figure 1.2(a) was the first armored vehicle that was fabricated from aluminum alloy in early 1950s. The hull structure of M113 is made up of AA5083 alloy, Al-5%Mg, which is a non-heat-treatable (meaning non precipitation hardenable), strain hardened (%20 cold rolled condition) aluminum-magnesium alloy. It has a 255 MPa yield strength derived from Mg solid solution strengthening and %20 cold rolling that results in elongated work hardened grains as shown in Figure 1.3(a) [1].

Its lighter weight, ease of weldability for manufacturing purposes, the level of ballistic performance against fragmentation threats and excellent corrosion resistance made it most preferable [5]. The dominant characteristics that made 5083-H131 most widely used aluminum alloy in military vehicles are the lower stress

corrosion cracking (SCC), low cost, and ease of fabrication in addition to its ballistic performance [6].



(a)

(b)



(c)

(d)

Figure 1.2 (a) M113 APC having 5083 structure (b) Scorpion Combat Vehicle having 7039 structure (c) The Bradley Fighting Vehicle having both 7039 (upper half) and 5083 (lower half) (d) Expeditionary Fighting Vehicle (EFV) having 2519 structure [7].

Scorpion and Bradley combat vehicles shown in Figure 1.2 (b,c) were developed after M113 and manufactured by using AA 7039 as an armor material which is Al-4Zn-2Mg alloy driving its high strength from precipitation hardening by heat treatment (age hardening) [1].

This heat treatable aluminum-magnesium-zinc alloy (7039) has a better damage resistance than 5083 aluminum alloy since its ultrafine Zn-Mg precipitates, within the grains shown in Figure 1.3(b), highly contribute to a yield strength of 350 MPa by blocking dislocation motion. It is registered as Aluminum alloy AA7039-T64

(MIL-A-46063). Its ballistic performance against ball and armor piercing (AP) threats is higher than that of 5083-H131. But it is more susceptible to SCC.

Hence it is not planned to be used in future vehicles. Therefore, 7039 alloy has been applied only to upper half of Bradley Fighting Vehicle in addition to Scorpion. Due to this shortcoming of SCC, numerous researches have been done to develop a new aluminum alloy in order to have high strength as much as 7039 and as low SCC as 5083. Under a self-propelled howitzer developing program (Crusader), a heat treatable aluminum-copper-manganese alloy registered, as AA2519-T87 (MIL-DTL-46192), was developed and considered as a good candidate aluminum armor material. It has a higher yield strength of 400 MPa mainly due to Al-Cu ( $\text{Al}_2\text{Cu}$ ) precipitation strengthening. But with the cancellation of this program, it was used in another vehicle, Expeditionary Fighting Vehicle (EFV) shown in Figure 1.2(d) [7-8].

Most recently 2139-T8 (MIL-DTL-32341) alloy was developed for aircraft industry in order to be used in damage critical applications. It has been found out that the new alloy had a better ballistic performance as compared to previous aluminum armor alloys; 5083, 7039 and 2519 as it can be clearly seen in Figure 1.4 [3]. This superior ballistic performance of 2139 alloy is generally attributed to the formation of fine and uniform dispersion of  $\Omega$  precipitates on  $\{111\}$  planes [9-10].

Recent studies related to new Al 2139 alloy (Al-Cu-Mg-Ag) show that ballistic performance and high strain rate response of this alloy strongly depends on the microstructure of material. Clayton [11] concluded in impact simulations that ballistic performance can be improved by grain texturing to increase shear strength or by increasing dynamic energy storage mechanisms that essentially reduce thermo-mechanical coupling strength ( $\beta$ ). This coupling strength signifies the ratio of the rate of plastic energy dissipated as heat during dynamic deformation process. Low thermo-mechanical coupling strength, therefore, effectively delays the occurrence of deformation instabilities in the form of adiabatic shear bands by reducing thermo-plastic heating and local thermal softening.

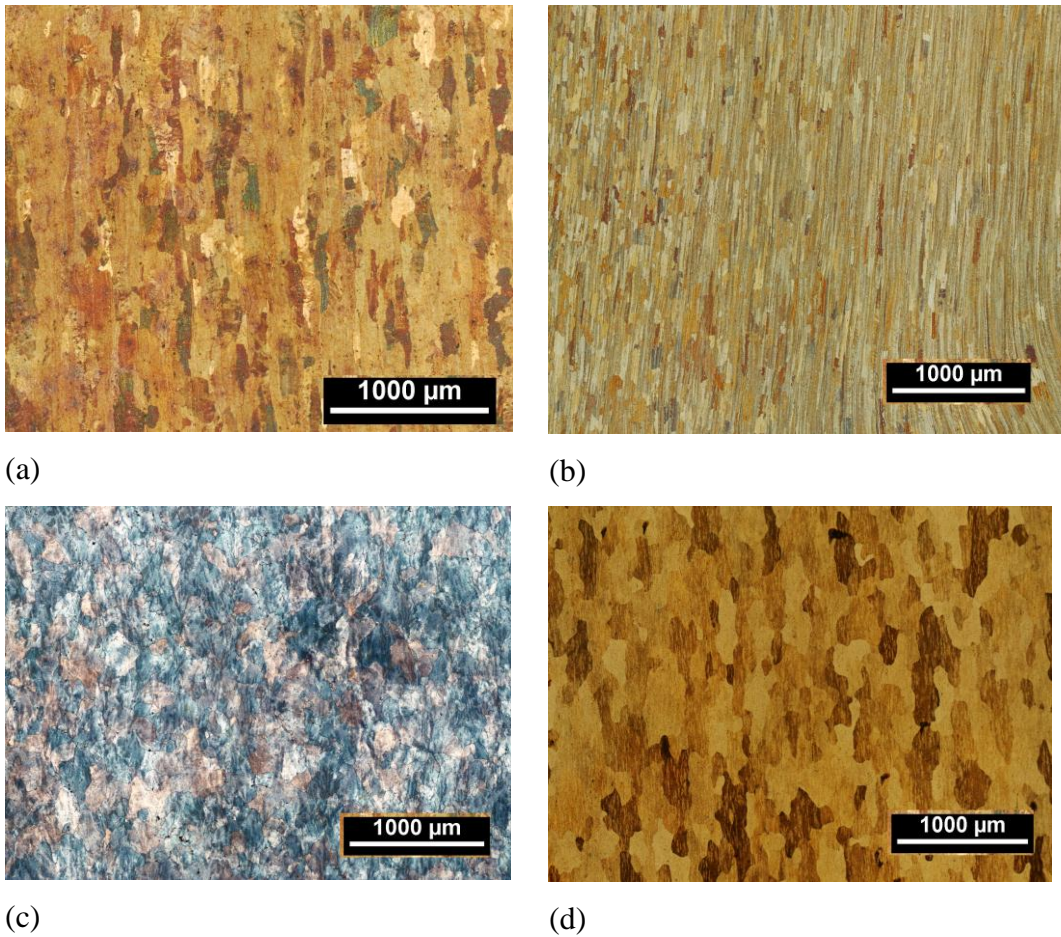


Figure 1.3 Microstructure of (a) 5083 (b) 7039 (c) 2519 (d) 2139 aluminum alloys.

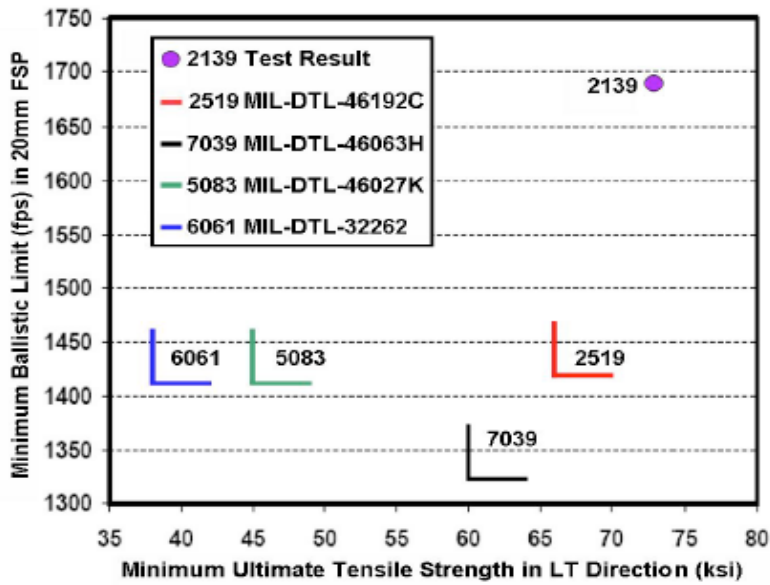


Figure 1.4 Strength and Ballistic Performance of 1 inch thick AA2139-T8 plate as compared to other aluminum armor alloys [3]

Although the superior ballistic performance of AA 2139 is commonly believed to come from the uniform dispersion of  $\Omega$  precipitates, it is still not clear which aspects of microstructure cause the significant ductility and lower susceptibility to shear localization under high strain rates as stated by Elkhodary et al. [12]. But their unique study covers only computational simulation which is based on a limited number of grains and precipitates. It provides a detailed understanding of underlying mechanism responsible for 2139 alloy's susceptibility to shear localization over a wide range of strain rates.

In summary, the aluminum alloys used as armor in lightweight armor vehicles are 5083, 7039 and 2519 according to their emerging and application period, respectively. Although the most well-known and the oldest ones are 5083 and 7039, ironically, they are also among the least studied in open literature [13]. Pérez-Bergquist et al. [14] studied dynamic and quasi-static mechanical response of 5083 and 7039 at only room temperature. Dannemann et al. [15] compared the mechanical and constitutive response of 5083 and 2139 at  $1500 \text{ s}^{-1}$  strain rate. Fisher et al. [8] tested 2519 at elevated temperatures as a function of low strain rate in order to define thermal softening effects. Zhang et al. [16] investigated the impact behavior of aluminum alloy 2519 at strain rates of  $600\text{--}7000 \text{ s}^{-1}$  and elevated temperatures.

Material properties and deformation behavior of aforementioned aluminum alloys depend on the rate at which the material is strained, and realistic analysis of armor-penetrator impact events requires predictive modeling of both quasi-static and dynamic material behavior. Quasi-static properties are easily measurable. Moreover, they can serve as a starting point for an analysis of the material dynamic properties that can only be understood by measuring properties at high strain rates.

Within the scope of this study, in order to determine the material properties over a wide range of extreme conditions (strain rates and temperatures), a series of static and dynamic tests were performed with high precision using the laboratory infrastructure in Mechanical, Materials and Aerospace Engineering Department of Illinois Institute of Technology (IIT). Several test techniques such as quasi-static

and Split Hopkinson pressure bar (SHPB) with unique specimen configurations at room and elevated temperatures were used to measure the dynamic behavior of materials up to  $10^5$  per second ( $s^{-1}$ ) of strain rates. Experimental data corresponding to four aluminum alloys (AA 5083, AA 7039, AA 2519, AA 2139) are obtained by using quasi-static and dynamic tests in a wide range of strain rates at various temperatures. Then, these data are analyzed in a comprehensive manner to understand the failure behavior under impact loading and to develop temperature, strain and strain rate dependent predictive constitutive models.

The Figure 1.5 shows that the materials at high strain rates have significantly higher flow stress and higher initial strain hardening. But as strain increases up to a critical strain, the material thermally softens. Then the slope of the curve actually becomes negative. Such factors must be well analyzed if one is to fully understand the performance of a material during ballistic impact [17-18].

One of the main goals of this study is to develop robust constitutive relations that describe the stress- strain behavior of materials over a wide range of strain rates, strains, and temperatures. Such relations will increase the ability to predict the behavior of particular armor systems under a variety of conditions [17] .

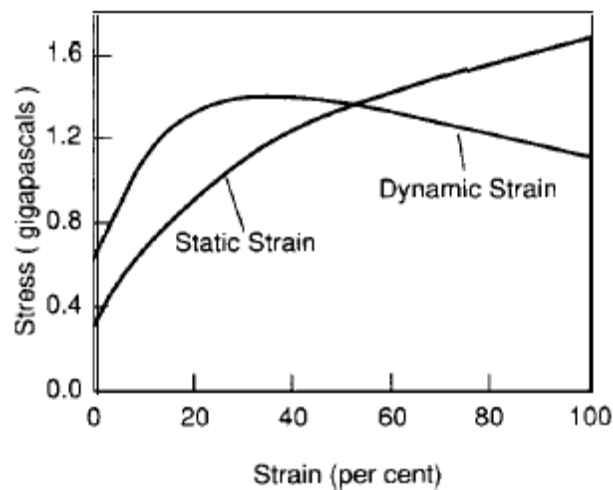


Figure 1.5 Stress-strain curves for depleted uranium at strain rates of  $5000 s^{-1}$  and  $0.001 s^{-1}$  [18].



Terminal ballistics involving kinetic energy ammunitions include high-velocity impact of projectiles ranging from small-caliber bullets to large-caliber tank ammunition, onto targets ranging from body armor for soldiers to heavy armor for main battle tanks. In the design and analysis of armor systems, the use of numerical methods with appropriate material and fracture models is much more efficient and cheaper than carrying out field tests. For these applications, constitutive equations are used to describe the dynamic response of materials mathematically under intense loading conditions. These equations must be able to accurately predict the response of the materials subjected to large strains, high strain rates, and high temperatures. Therefore material modeling is very important for high speed impact applications, and it is often the most important component of the reliability of a computational simulation. There are available models for a wide range of metals such as aluminum alloys, steel alloys and copper, concrete, ceramics, fabrics and composites that are common materials for targets, or armors. Generally, different type of materials models must be used for these different types of materials and their response can be characterized by model parameters that must be experimentally determined for each material. Determining model parameters requires numerous quasi-static and dynamic experiments to quantify the effects of strain, strain rate and temperature during dynamic deformation process [17].

In this perspective, all aluminum alloy armor materials, starting from the first emerged one, 5083, to the latest one, 2139, need to be further analyzed through comprehensive high strain rate experiments not only to develop predictive rate and temperature dependent constitutive models but also to understand their adiabatic shear localization behaviors. Unfortunately, the dynamic deformation responses of forementioned aluminum alloys are not well documented in open literature.

Therefore, the main objective of this research study is to investigate the dynamic behavior these aluminum alloys: 2139-T8, 2519-T87, 5083-H131 and 7039-T64, commonly used in lightweight armored military vehicles in a comparative manner and establish a robust experimental database as well as constitutive models for their dynamic response over a wide range of strain rates and temperatures typically encountered in penetration and impact events.

Unlike quasi-static deformation processes, dynamic impact and penetration events often involve high strain rates, large strains and rapid changes in temperature due to severe thermoplastic heating and adiabatic deformation conditions. Therefore, any reliable simulation and/or design of armor systems require the development of predictive constitutive models that heavily rely on extensive experimentation at high strain rates and elevated temperatures.

In the first phase of study, high strain rate experiments were conducted by using split-Hopkinson pressure bar (SHPB) apparatus at both room temperature and elevated temperatures to understand and document the constitutive behavior of selected aluminum alloys. Quasi-static experiments were also conducted to establish a basis for comparison and more comprehensive analysis of the constitutive response.

In the second phase, the emphasis was placed on developing predictive constitutive models and finding model parameters. Both phenomenological (Johnson-Cook, Modified Johnson-Cook) and physics based (Zerilli-Armstrong, Modified Zerilli-Armstrong, Turkkan-Vural Modified Zerilli-Armstrong) models were utilized and their performances were evaluated. According to these results, a new modified model was proposed by combining Modified Johnson-Cook and Turkkan-Vural Modified Zerilli-Armstrong Models depending on their ability in capturing the experimental data.

This study has also led to an advanced understanding of aluminum alloys armor materials' tendency to shear localization in the form of adiabatic shear banding (ASB) by using shear-compression specimens (SCS) in controlled dynamic experiments followed by detailed microstructural examination. Then, building on the experimental results and observations, the competition among strain hardening, strain rate hardening and thermal softening mechanisms were evaluated for each alloy to develop a comprehensive analysis of their dynamic deformation and failure behavior.

## CHAPTER 2

### THEORITICAL BACKGROUND

#### 2.1 High Strain Rate (Dynamic) Deformation

Unlike quasi-static behavior of materials at typical quasi-static strain rates of  $10^{-4} - 10^{-3} \text{ s}^{-1}$ , dynamic behavior deformation occurs under 10 to 100 million times faster strain rates (typically in  $10^3 - 10^4 \text{ s}^{-1}$  range). Therefore, hardening due to strain rate of material cannot be ignored in constitutive models in dynamic range. In addition, dynamic plastic deformation occurs in very short time scale (impact time) that is typically 1-to-3 orders of magnitude shorter than critical time scale for heat dissipation. As it is often assumed that 90% of plastic deformation is converted to heat, dynamic deformations therefore occur under adiabatic conditions where thermoplastic heating cannot dissipate away as in quasi-static conditions. This leads to rapid temperature increase proportional to the amount of local plastic deformation. Therefore, thermal softening coupled with strain rate hardening and strain hardening should be carefully included in constitutive models. It is obvious that building predictive constitutive models in dynamic range requires extensive experiments at varying high strain rates as well as temperatures [19].

Additionally, most of the deformations at high strain-rates occur at velocities sufficiently large to cause inelastic (and particularly plastic) deformations that may also lead to large strains and high temperatures [20].

Considering all these, the flow stress of materials during high strain rate plastic deformation of materials should be described as a function of strain ( $\varepsilon$ ), strain rate ( $\dot{\varepsilon}$ ) and temperature ( $T$ ) as follows;

$$\sigma = f(\varepsilon, \dot{\varepsilon}, T)$$

In order to describe the dynamic behavior of materials as a function of strain ( $\varepsilon$ ), strain rate ( $\dot{\varepsilon}$ ) and temperature ( $T$ ), many models have been proposed by many researchers and some of them has been successfully used in computational simulations. The main objective in modeling the flow stress is to predict the data of Figures 2.1-2.3 along with the variation of strain hardening in one single equation [19].

The materials are known to exhibit strain hardening at quasi-static strain rates and at room temperature which is often approximated by well-known parabolic hardening relation[19];

$$\sigma = \sigma_0 + B\varepsilon^n \quad (2.1)$$

where  $\sigma_0$  is the yield stress,  $n$  and  $B$  are the strain hardening parameters.

At elevated temperatures, the effect of temperature on flow stress can be expressed separately as;

$$\sigma = \sigma_r \left[ 1 - \left( \frac{T - T_r}{T_m - T_r} \right)^m \right] \quad (2.2)$$

where  $T_m$  is the melting temperature, and  $T_r$  is the reference temperature at which the reference stress,  $\sigma_r$ , is measured [19].

The effect of strain rate can be expressed simply as follows;

$$\sigma \propto \ln \dot{\varepsilon}$$

This relation although affected by temperatures, generally hold at low and medium strain rates as shown in Figures 2.1-2.3 [19, 21-23]. As it can be seen in these figures, however, this linear relationship breaks down at a certain strain rate between  $10^2 \text{ s}^{-1}$  and  $10^3 \text{ s}^{-1}$ , which is later named as the transition strain rate by Vural et al [10].

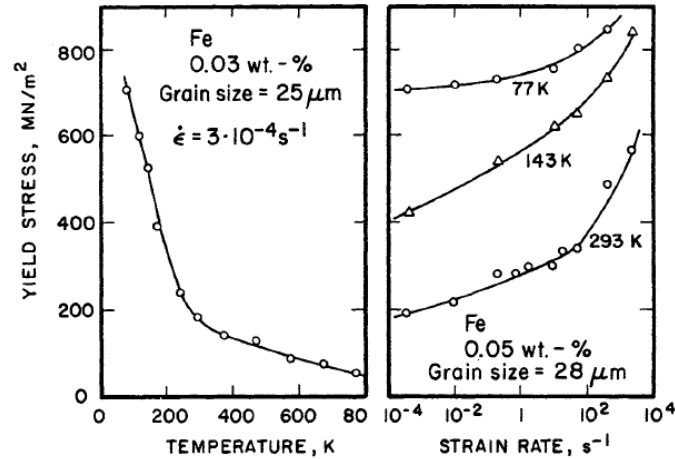


Figure 2.1 Effects of temperature and strain rate on the yield stress of iron (from [21].) [19].

According to Follansbee and Kocks [24] rate controlling mechanism are responsible for this change in strain rate sensitivity. Thermal activation mechanism is the rate controlling at low (quasi-static) strain rate regime and intermediate high strain rate regime (below  $10^4 \text{ s}^{-1}$ ) while dislocation drag control [25-27] is effective at high strain rate above  $10^4 \text{ s}^{-1}$ . Depending on the material, flow stresses in this strain rate range have different strain rate sensitivities such that at around a strain rate of  $10^3 \text{ s}^{-1}$ , many materials show a considerable upturn in the flow stress value [28] as it is shown in Figures 2-1-2.3. The transition strain rate for this upturn is different for each material. Dislocation drag control mechanisms cause the flow stress to increase drastically after this upturn point that is defined as the transition strain rate by Vural et al. [10]. Further increase in strain rate, the dislocation speed is close to the sound of speed waves and relativistic effects take place. Thus three regimes of strain rate behavior shown in Figure 2.2 are defined by three different mechanics governing plastic flow [19, 22, 23, 25, 27, 28]. In region I, thermally activated dislocation motion is the controlling mechanism, while regions II and III are considered to be governed by drag mechanisms and relativistic effects, respectively [22].

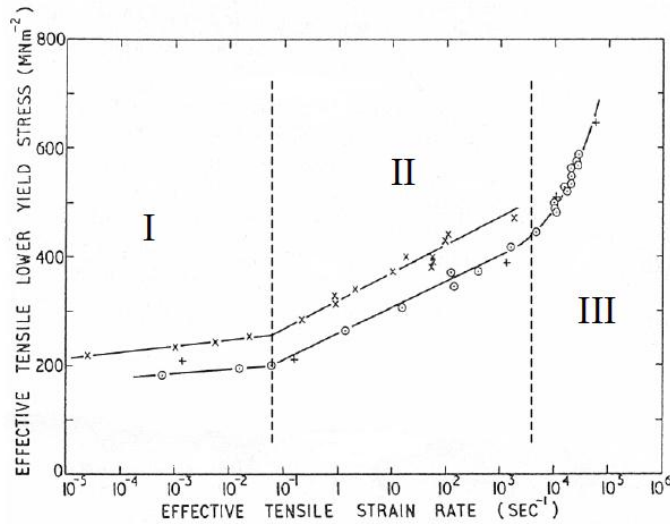


Figure 2.2 Three Regions of Strain Rate Sensitive Behavior for En3B Steel [26]. The labels and vertical dashed lines were added by [22].

However, Follansbee [23] showed two regions illustrated in Figure 2.3, where flow stress values of OFHC copper are plotted as a function of strain rate. According to the Follansbee [23], the transition occurs between  $10^3 \text{ s}^{-1}$  and  $10^4 \text{ s}^{-1}$  strain rates.

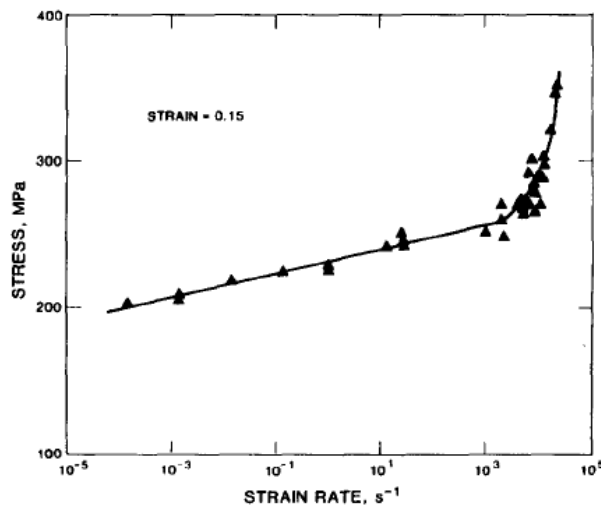


Figure 2.3 Flow stress measurements (compression) at  $\epsilon = 0.15$  in OFE copper as a function of strain rate [23].

Hence, thermally activated dislocation motion and dislocation drag mechanisms can be considered as the governing mechanisms below  $10^3$ - $10^4 \text{ s}^{-1}$  and above  $10^3$ - $10^4 \text{ s}^{-1}$  respectively.

### 2.1.1 Thermally Activated Dislocation Motion

A dislocation meets obstacles as it moves under plastic deformation. The flow stress is the required macroscopic stress to overcome these obstacles. Some examples of these obstacles are solute atoms, vacancies, small angle boundaries, vacancy clusters, inclusions and precipitates. Dislocations can also act as an obstacle themselves. As a dislocation moves from one equilibrium atomic position to the next, it has to overcome an energy barrier [19].

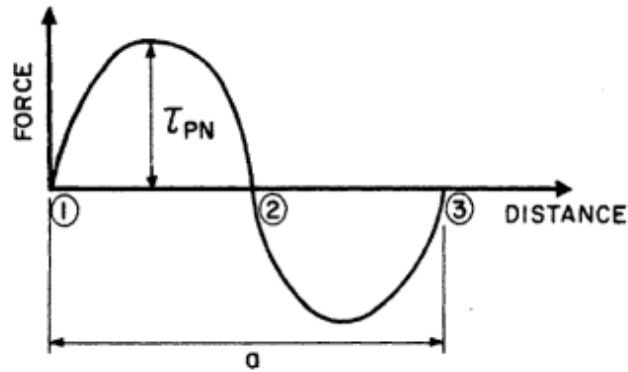


Figure 2.4 Peierls-Nabarro force: applied stress vs. distance [19].

Peierls-Nabarro barrier is the stress necessary for a dislocation to move by one atomic space without any other additional external help as shown in Figure 2.4 and Equation 2.3 where  $G$  is the shear modulus,  $b$  is the Burgers vector,  $c$  is the lattice spacing, and  $a$  is the lattice parameter [19].

$$\tau_{PN} = \frac{Gb}{2c} \exp(-\pi a/c) \sin(2\pi x/c) \quad (2.3)$$

Therefore, a dislocation encounters periodic barriers of different spacing and length scales. Figure 2.5 shows schematically a short-range barrier and the effect of thermal energy on overcoming these obstacles. The smaller and narrower barriers such as the lattice structure itself are called short-range barriers and larger, wider barriers such as point defects, precipitates, grain/twin boundaries, etc. are called long-range barriers. Thermal energy increases the amplitude of the vibration of atoms, increasing the probability of an atom to jump over short-range barriers. This thermal energy thus act to decrease the stress required to move a dislocation over

the barrier as depicted in Figure 2.6. The shaded area shows the thermal energies  $\Delta G_1$ ,  $\Delta G_2$  and  $\Delta G_3$  available at increasing temperatures. As the temperature increases, the increased thermal energy causes the height of the barrier to decrease as it is shown in Figure 2.5. The strain rate (i.e., dislocation velocity) has a similar but opposite effect to that of temperature. As strain rate increases less time is available for the dislocation to overcome the short-range barriers provided by lattice atoms. This decreases the effect of thermal energy, resulting in an increased stress required for dislocation motion. On the other hand, long-range barriers depicted in Figure 2.6 differ from short-range barriers because changes in thermal energy do not greatly affect the ability of dislocations to move past them. This occurs because atomic vibration amplitude has little effect on the size of the long-range energy barrier presented to dislocation. Consequently, the amount of energy required to move a dislocation past these large obstacles is orders of magnitude larger than that provided by the increased lattice vibration that results from increases in temperature. As a result, it is concluded that short-range barriers are thermally activated and long-range barriers are not thermally activated. Therefore the material flow stress can be expressed by the following Equation 2.4 [19].

$$\sigma = \sigma_a(\text{structure}) + \sigma^*(T, \dot{\epsilon}, \text{structure}) \quad (2.4)$$

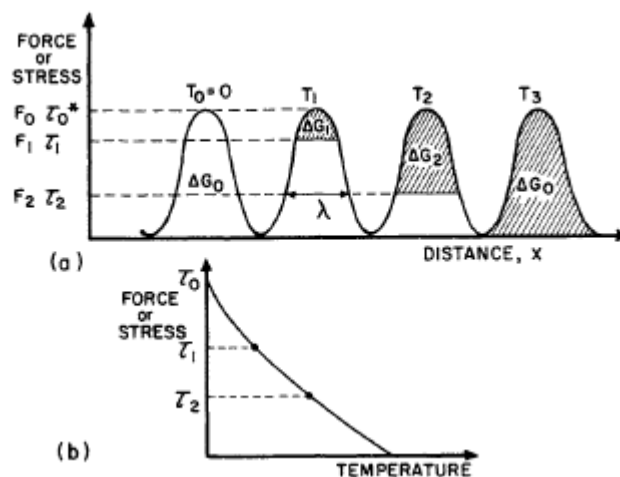


Figure 2.5 (a) Thermal energy needed to overcome short range obstacles  
 (b) Stress as a function of temperature needed to overcome obstacles [19].



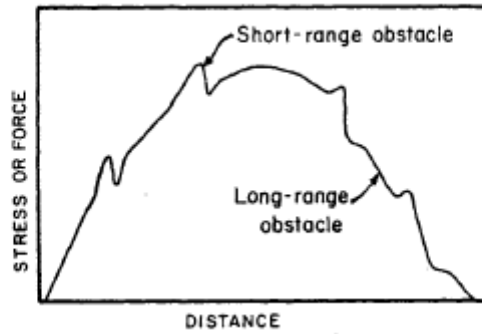


Figure 2.6 Schematic of a long-range obstacles overcome by a dislocation on its way [19].

The first term  $\sigma_a$  is due to the athermal or the long-range barriers to dislocation motion and it is specific property of material structure. The second term  $\sigma^*$  describes the action of thermally activated short-range barriers. The short-range barriers include Peierls-Nabarro stress and dislocation forests. Peierls-Nabarro stresses (lattice friction stresses) are the controlling short-range barriers in BCC metals while dislocation forest structures are the controlling short-range barriers in FCC and HCP metals. This difference is responsible for the difference in strain rate sensitivity between BCC and FCC metals [19].

### 2.1.2 Dislocation Drag Mechanism

At relatively low deformation rates, dislocations overcome short-range barriers under the combined action of the applied stress and thermal fluctuations as discussed in preceding section. For a high-rate deformation, it is necessary to apply higher stresses. At a deformation rate that exceeds a certain threshold value, i.e., transition strain rate, the acting stresses are sufficient to provide a dynamic overcoming of obstacles (such as Peierls barriers) without additional contribution from thermal fluctuations. In this case, the dominant mechanism resisting the dislocation motion is dislocation drag which involves the transfer of dislocation energy into crystal lattice vibrations or, depending on the temperature, into electronic subsystems. In dislocation drag mechanism, the material can be effectively considered to have a viscous behavior against dislocation motion at high strain rates over  $10^3$ - $10^4$   $s^{-1}$  range. Therefore, the concepts of Newtonian viscosity can be borrowed to understand the evolution of flow stress in a material subjected to

deformation rates beyond the transition strain rate. In a Newtonian viscous material, the viscous drag force is given by [19];

$$f_v = Bv \quad (2.5)$$

where  $B$  is the viscous damping (drag) coefficient and  $v$  is the velocity of the fluid, which will be replaced by dislocation velocity for dislocation drag. The flow shear force, therefore, can be approximated by the following relation.

$$\tau b = Bv \quad (2.6)$$

Furthermore, the dislocation velocity is related to shear strain rate and the density of mobile dislocations through the following relationship;

$$\dot{\gamma} = \rho b v \quad (2.7)$$

where  $\dot{\gamma}$  is shear strain rate which is expressed by mobile dislocation density ( $\rho$ ), Burgers vector ( $b$ ) and dislocation velocity ( $v$ ).

In the dislocation mechanics, the shear strain can be converted to normal strain by adding an orientation factor  $M$  such that strain rate can be related to dislocation velocity via;

$$\dot{\epsilon} = \frac{1}{M} \rho b v \text{ and } \tau = \frac{1}{2} \sigma \quad (2.8)$$

Now, by using Equations 2.6 and 2.8, flow stress can be expressed by;

$$\sigma = \frac{2BM}{\rho b^2} \dot{\epsilon} \quad (2.9)$$

Therefore, the flow stress is proportional to the strain rate under dislocation drag mechanisms. This causes the flow stress to rise drastically beyond a transition strain rate which is typically within  $10^3$ - $10^4$   $s^{-1}$  range [19].

### **2.1.3 Adiabatic Shear Localization**

When metals and other materials are subjected to extreme dynamic loads such as encountered in ballistic penetration, high speed machining and explosive loading events, they undergo large strains in a very limited time scale typically measured in tens or hundreds of microseconds. A large fraction of the plastic work done by these dynamic loadings is converted into heat. This fraction is typically as much as 90% of the plastic work. Therefore, large plastic deformations under dynamic loading conditions also involve high temperatures and resulting thermal softening. Competition among strain hardening, strain rate hardening and thermal softening might result in localized deformation instabilities in the form of intense localized shearing which often leads catastrophic fracture in the material subjected to dynamic loading [29].

This localized shear band was called as adiabatic shear band (ASB) by Zener and Hollomon [30] because the short time scale of the dynamic deformation does not allow any thermoplastic heating to dissipate away such that all of the locally generated heat is used to increase local temperature, making the ideal conditions of an adiabatic process in thermodynamic sense without any heat loss. However, after the localized shear bands occur, a rapid quenching phenomena takes place from high temperature. That is because it leads a martensitic microstructure accompanying with micro cracks within the ASB's. This phenomenon is often referred to as "catastrophic thermoplastic shear" by Rogers [31] and Bai et al [32].

ASB's can lead to brittle or ductile fracture in materials. The failure modes of a material are shown in Figure 2.7 [33]. The ductile alloys such as aluminum alloys mostly subjected to failure in the shape of plugging as the projectile impact velocity

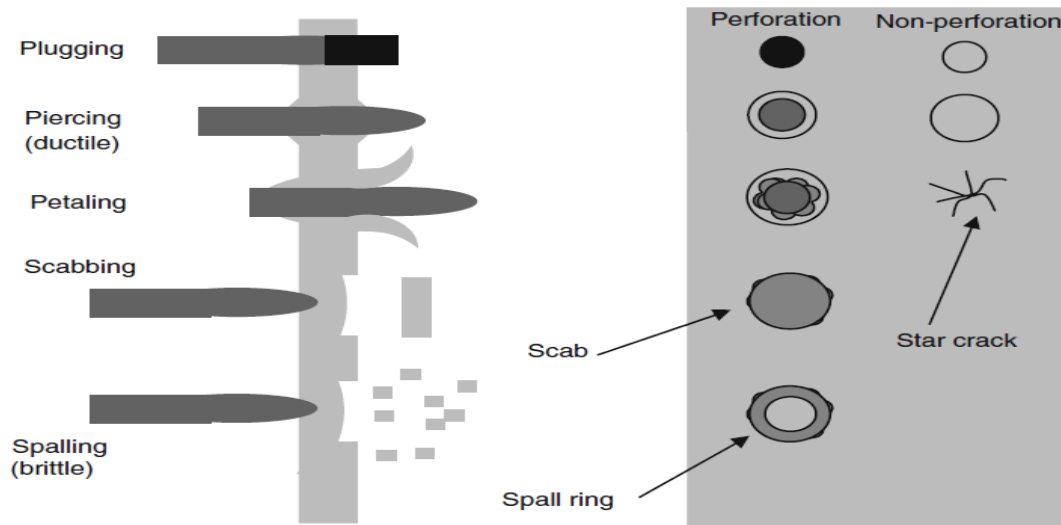


Figure 2.7 Failure modes of material subjected to high velocity impact [33].

is very close to ballistic limit as it seen in Figure 2.8. It shows complete penetration of 5083 aluminum armor alloy where ASB's were encountered in the impact zone where a plug has been formed [33-34]. Chen et al. [35] called this phenomena as adiabatic shear plugging, which occurs as a result of high localization of the strains, strain rates and temperature at the "plug" location, accompanied by a developing process of the deformed-type shear band zones, transformed-type shear band zones, and adiabatic cracking fracture zones. The adiabatic shear plugging is a failure following highly localized shear strains where shear bands occur first inside the plate and propagate to the surface forming a macro-crack [36].

### 2.1.3.1 Evolution of Adiabatic Shear Bands

Duffy [37] stated that the shear localization can be divided into three consecutive stages depending on the value of strain according to the reference [38]. These stages were called as 1<sup>st</sup>, 2<sup>nd</sup> and 3<sup>rd</sup> stage as shown in Figure 2.9. In the 1<sup>st</sup> stage, the shear bands are inclined but essentially straight meaning a homogenous shear deformation. In the 2<sup>nd</sup> stage, the shear bands appear curved uniformly around the gage length indicating onset of an inhomogeneous deformation. Lastly, in the 3<sup>rd</sup> stage, the shear lines become discontinuous showing the presence of a shear band or a crack. In this stage, shear strain locally goes up to very high values such as 4-5 depending on the macroscopic strain. This local large shear strains cause the

temperature within the shear band to increase and resulting thermal softening provides the flow stress to drop first gradually and then sharply as it transforms to a shear crack [37].

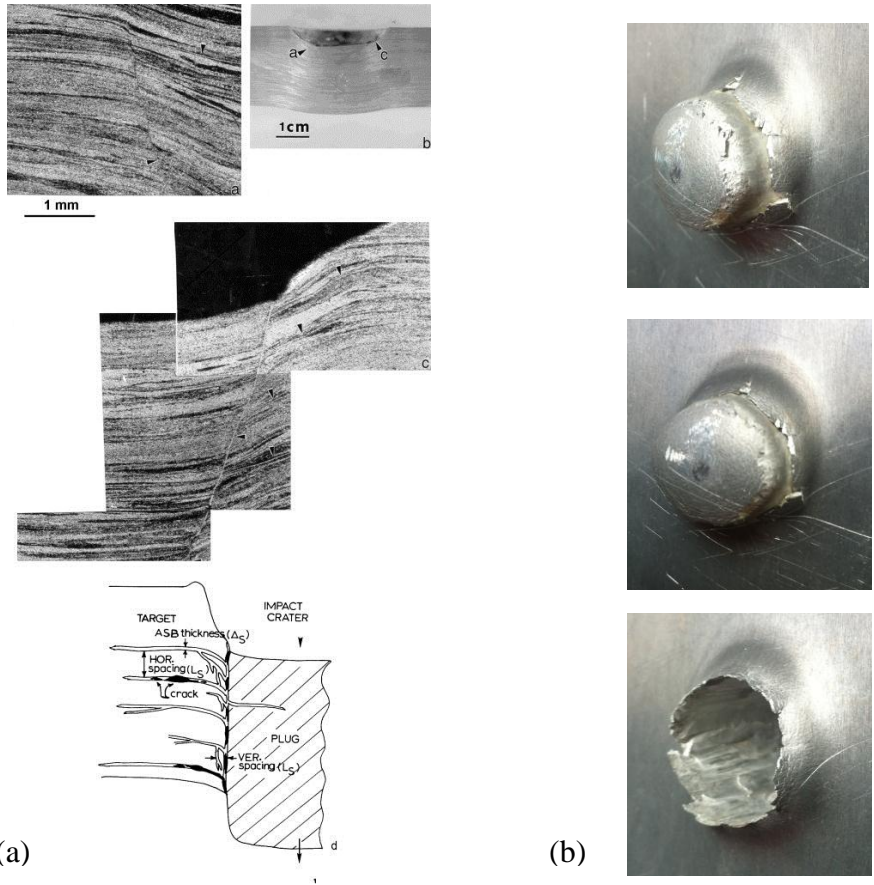


Figure 2.8 (a) Optical metallographic views of ASB formation and incipient plug [34]  
 (b) Plug formation in penetration of 5083 by 20 mm FSP

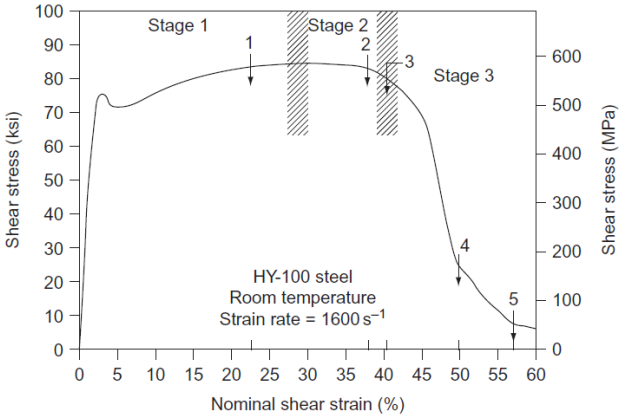


Figure 2.9 A typical stress-strain curve showing the three stages of plastic deformation [29].

### 2.1.3.2 Experimental methods for Adiabatic Shear Bands

There are different type of experiments which are used to determine the propensity of the materials to fail under adiabatic shear localization with their advantages and disadvantages. The most widely used ones are torsion, hat-shaped specimen and shear compression specimen (SCS). Torsion test techniques are lathe torsion testing, a torsional hydraulic, impact torsion techniques and Split Hopkinson torsion bar systems. In these techniques a strain rate range between  $10^2$  and  $10^4$   $s^{-1}$  can be provided. The specimen used can be made of solid bars or thin-walled tubes. In most cases, Split Hopkinson torsion bar systems [39] have been used to investigate torsional behavior of materials. In this technique, a simple loading condition, a uniform stress state and good measurement of signals of stress-strain data can be obtained while it is not possible to get high strain rates. Additionally, the test results can be affected by buckling.

The second technique is the hat-shaped specimen technique, which was invented in 1977 by Meyer and Hartmann (Figure 2.10), that is often used in a Split Hopkinson Pressure Bar (SHPB) setup. The hat-shaped specimen is located between incident and transmitted bars in a compression SHPB setup. The advantages are that it can be used to obtain shear bands even in very ductile materials and at very high strain rates. However the shear-stress measurement is influenced by edge effects due to the geometry shown in Figure 2.10 and the calculation of the shear strain is not so straight forward because the size of the shear zone is not easily predictable without post-mortem metallographic examination [29].

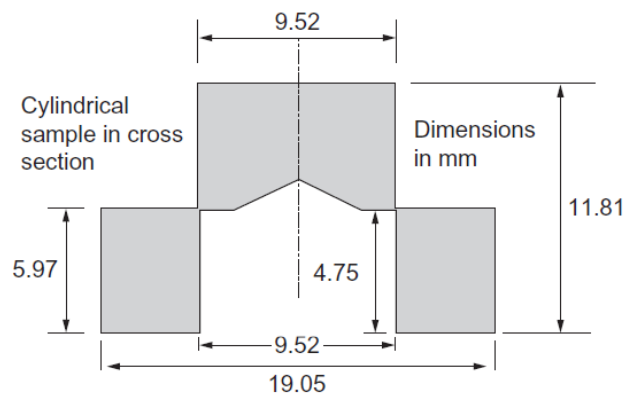


Figure 2.10 Geometry of a hat-shaped specimen [29].

The latest unique design to investigate the propensity to adiabatic shear failure was invented by Rittel et al. [40]. Due to the buckling, bending problems in torsion specimen and non-homogeneous stress-strain field in hat-shaped specimen, it is more advantageous to use SCS's than the other specimen geometries (for a review, Bai and Dodd [29]).

## **2.2 High Strain Rate (Dynamic) Experiments**

### **2.2.1 Split Hopkinson Pressure Bar (SHPB)**

The most widely used technique in investigating dynamic behavior (stress-strain curves) of the materials is Split Hopkinson Pressure Bar (SHBP). Its fundamental concept of one dimensional wave propagation in bars was first developed by John Hopkinson (1849-1898) and his son, Bertram Hopkinson (1874-1918) [41]. Four decades after the inception of this concept, Davies [42] and Kolsky [43] developed the final form of SHPB setup which is still in use today. Davies originally used the electric technology to measure the pulse length and the displacements in the pressure bar. Kolsky developed Compression SHPB that is still being used.

SHPB is a unique experimental apparatus that is used to obtain stress-strain behavior of materials at high strain rates from  $10^2$  to  $10^4$  s<sup>-1</sup>. It consists of two coaxially installed bars, called incident (input) bar and transmitted (output) bar, which are essentially used to guide one dimensional wave propagation. The specimen to be tested is placed in between these two bars as schematically shown in Figure 2.11. A striker bar of the same diameter and material is launched from a gas gun and generates a compressive stress wave when it impacts on the incident bar. When this compressive wave propagates along the incident bar and reach the specimen, part of the compressive stress wave reflects back as a tension wave and the part is transmitted through specimen to output bar as a compressive wave. During this process the specimen is dynamically compressed at very high strain rates.

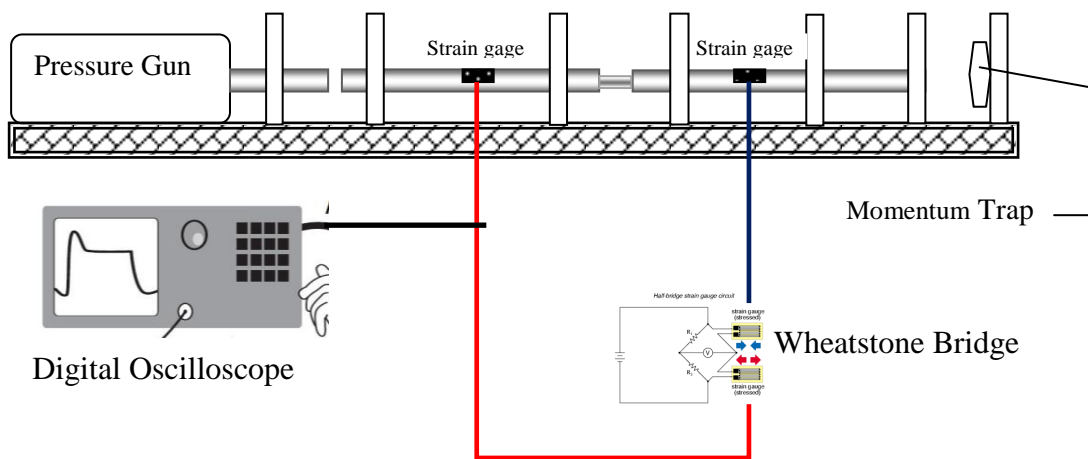


Figure 2.11 A schematic of SHPB set-up.

Time resolved profiles of incident, reflected and transmitted stress waves are detected by the strain gages glued on input and output bars and recorded by using a high-speed digital storage oscilloscope. These stress waves are then post-processed to construct dynamic stress-strain behavior of specimen and time resolved evolution of strain rate during the experiment.

### 2.2.1.1. Propagation of Compressive Pulse:

After firing the gas gun, the striker bar coaxially impacts the incident bar that have the same diameter and material with the striker bar. Upon impact, a compressive stress pulse in the form of one dimensional wave propagates along both the incident bar and striker bar with longitudinal wave propagation speed ( $C$ ) as shown in Figure 2.12.

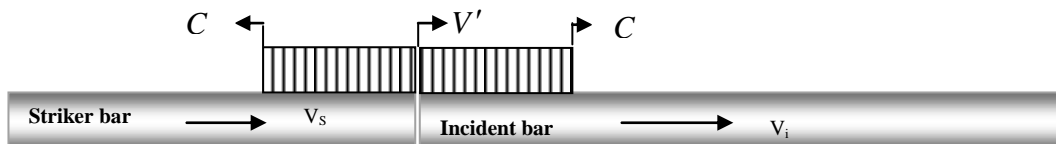


Figure 2.12 Stress wave propagation on striker and incident bars of SHPB just after impact



The analysis of the equation of motion on an infinitesimal material element in the bar yields the following relations:

$u$  : displacement

$v$  : particle speed

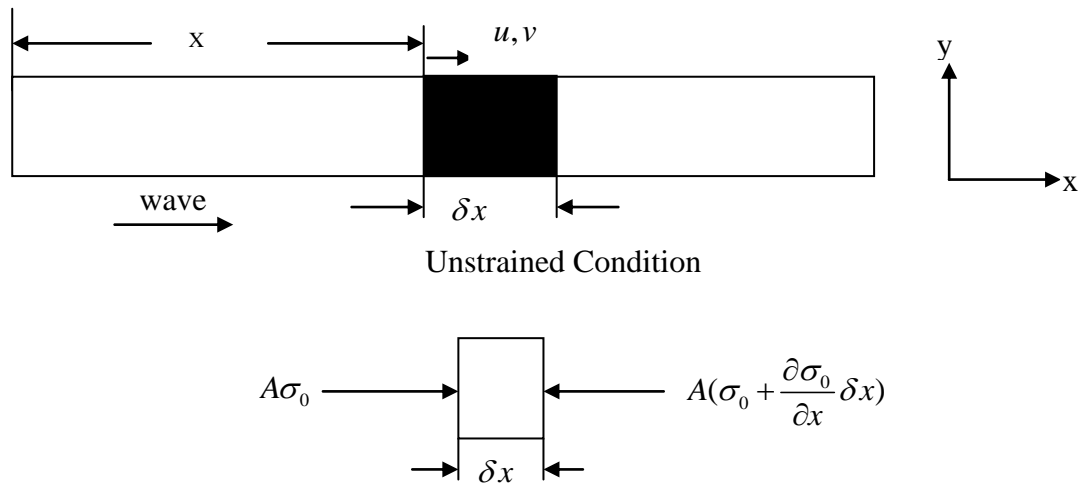


Figure 2.13 Propagation of an elastic compressive wave in a thin cylindrical bar

Assuming an elastic compressive wave of propagating velocity  $C$  is induced throughout the cylindrical bar in a longitudinal direction as shown in Figure 2.13 and considering the Newton's 2<sup>nd</sup> law as an equation of motion;

$$F_x = ma$$

$$\underbrace{-A\left(\sigma_0 + \frac{\partial \sigma_0}{\partial x} \delta x\right) + A\sigma_0}_{\sum F_x} = \underbrace{A\delta x \rho}_{ma} \frac{\partial^2 u}{\partial t^2} \quad (2.10)$$

where  $A$  is the cross-sectional area of the bar,  $\rho$  is the density of the bar,  $\delta x$  is the length of the infinitesimal cross-section element considered which the wave is passing through,  $u$  is the displacement of particles in the cross-section, and  $\sigma_0$  is the stress at the left side of the cross-section. Then the result will be;

$$\frac{\partial \sigma_0}{\partial x} = -\rho \frac{\partial^2 u}{\partial t^2} \quad (2.11)$$

The negative sign appears because we have implicitly defined compressive wave to be positive in Figure 2.13.

Using the one dimensional (longitudinal direction) Hooke's Law and the strain in a length of  $\partial x$  as  $\frac{\partial u}{\partial x}$ . Then,

$$\begin{aligned}\sigma &= E.\varepsilon \\ \sigma_0 &= -E.\frac{\partial u}{\partial x}\end{aligned}\tag{2.12}$$

Here  $E$  is the elastic (Young's) modulus of the bar and  $\varepsilon$  is the elastic strain. Combining equations 2.11 and 2.12;

$$\sigma = -E \partial u / \partial x \xrightarrow{\text{After differentiating}} \frac{\partial \sigma_0}{\partial x} = -E \frac{\partial^2 u}{\partial x^2}\tag{2.13}$$

and using Equation 2.12 in Equation 2.13,

$$\rho \frac{\partial^2 u}{\partial t^2} = E \frac{\partial^2 u}{\partial x^2}\tag{2.14}$$

By using the definition of wave speed;

$$C = \sqrt{\frac{E}{\rho}} \Rightarrow \text{material properties}\tag{2.15}$$

where  $C$  is the stress wave propagation speed.

Combining Equations 2.14 and 2.15;

$$\frac{\partial^2 u}{\partial t^2} = C^2 \frac{\partial^2 u}{\partial x^2}\tag{2.16}$$

This is a partial differential equation of the second order describing the propagation of longitudinal waves along the bar with velocity  $C$ . Using a solution developed by D'Alembert we have:

$$u = \underbrace{f(x-Ct)}_{\text{forward moving waves}} + \underbrace{F(x+Ct)}_{\text{backward moving waves}} \quad (2.17)$$

where  $f$  and  $F$  are arbitrary functions of the quantities  $(x-Ct)$  and  $(x+Ct)$  respectively,  $u$  is the displacement,  $f$  is the wave travelling in the direction of increasing  $x$ ,  $F$  is the wave travelling in the direction of decreasing  $x$ .

Additionally, the stress wave is propagating without changing its shape, its intensity and speed, i.e. there is no dispersion. Considering only the backward moving wave,

$$u = F(Ct+x) \quad (2.18)$$

$$\frac{\partial u}{\partial x} = \frac{\partial F}{\partial (Ct+x)} \frac{\partial (Ct+x)}{\partial x} = F' \quad (2.19)$$

$$\frac{\partial u}{\partial t} = \frac{\partial F}{\partial (Ct+x)} \underbrace{\frac{\partial (Ct+x)}{\partial t}}_c = CF' \quad (2.20)$$

after relating Equation 2.19. and 2.20:

$$\frac{\partial u}{\partial x} = \frac{1}{C} \frac{\partial u}{\partial t} \quad (2.21)$$

$\varepsilon \qquad \qquad \qquad v$

Recalling that strain is  $\varepsilon = \frac{\partial u}{\partial x}$  change in particle velocity  $v = \frac{\partial u}{\partial t}$ , and substituting them into Equation 2.21 together with the Hooke's law:

$$\frac{\sigma_0}{E} = \frac{1}{C} v \Rightarrow \boxed{\sigma_0 = \rho C v} \quad (2.22)$$

where  $\rho C$  is the acoustic impedance and is a material property. This last relationship means that a stress wave of amplitude  $\sigma_0$  induces a particle velocity  $v$  in the bar inversely proportional to the acoustic impedance of bar. This is an important relationship because it allows us to calculate particle velocity if we can measure the amplitude of stress wave.

Now, considering the schematics of Figure 2.12, just after the impact,  $V$  is the common velocity of the interface between the striker and input bars.

In the regions of the bars where the waves are present,  $(V_s - V')$  is the velocity change in the striker bar and  $(V' - 0)$  is the velocity change in the incident bar. Therefore, we can calculate the stresses in both bars by using the conservation of momentum expressed by Equation 2.22 as follows:

$$\text{The stress in the striker bar} \quad \sigma_s = \rho C (V_s - V') \quad (2.23)$$

$$\text{The stress in the incident bar} \quad \sigma_i = \rho C (V' - 0) \quad (2.24)$$

Since  $F_1 = F_2$  and  $A_1 = A_2$  then  $\sigma_s = \sigma_i$  and the material is the same.

$$\rho C (V_s - V') = \rho C (V' - 0) \Rightarrow V' = \frac{V_s}{2} \quad (2.25)$$

This means that the particle velocity induced in the input bar right after the striker impact is half of the striker bar velocity when the material and the cross section of the striker and incident bar are the same. After the striker coaxially impacts the incident bar, a compressive stress pulse is generated as shown in Figure 2.14.

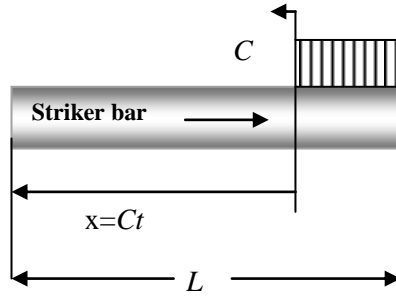


Figure 2.14 Stress wave propagation in the striker bar of SHPB

When the stress wave reaches the free end of the striker after the time  $t = \frac{L}{C}$ ; the compressive stress wave reflects as a tensile (unloading) wave with the same amplitude. Then after a time period of  $2t = \frac{2L}{C}$  the unloading wave reaches the impact point while the stress waves on the incident bar is propagating as a compressive wave. As a result, a compressive wave of  $2t$  length (in time domain)

propagates along the input (incident) bar as shown in Figure 2.15. Pulse length depends on the striker bar length ( $L$ ).

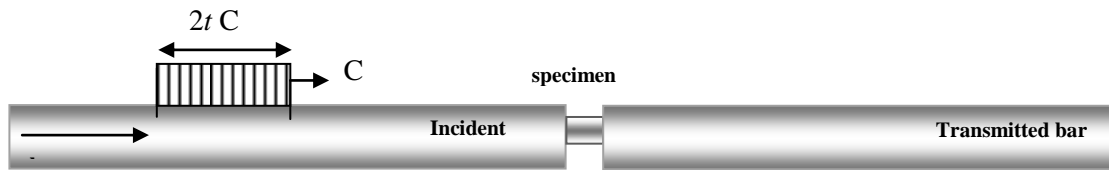


Figure 2.15 Stress wave propagation on incident bar of SHPB

### 2.2.1.2. Specimen Stress and Strain Calculation

When the compressive stress wave in incident bar (i.e., incident wave,  $\sigma_I$ ) reaches the specimen, part of it is reflected (i.e., reflected wave,  $\sigma_R$ ) and the part is transmitted (i.e., transmitted wave,  $\sigma_T$ ) over specimen to the transmitted bar as depicted in Figure 2.16.

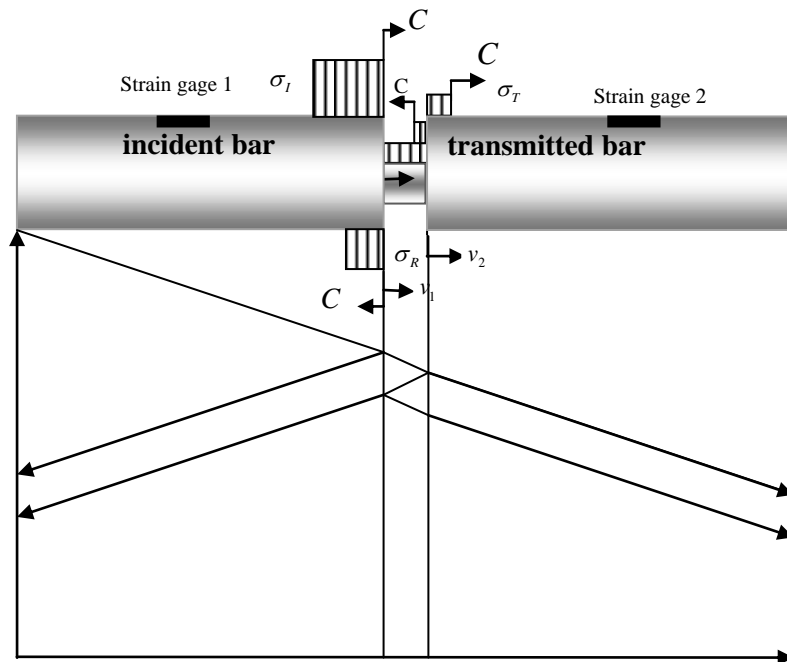


Figure 2.16 Stress wave propagation on incident bar, specimen and transmitted bar of SHPB after impact of incident bar on specimen

The terms  $v_1$  and  $v_2$  shown in Figure 2.16 are the interface velocities at in incident bar and transmitted bar respectively. Since  $v_1 > v_2$ , the specimen length ( $L_s$ ) decreases as it is compressed in between the incident and transmitted bars. Compressive strain rate  $\dot{\epsilon}$  can, therefore, be described as follows:

$$\dot{\varepsilon} = \frac{d\varepsilon}{dt} = \frac{v_1 - v_2}{L_s} \quad (2.26)$$

where  $L_s$  is the initial length of the specimen. The velocities can be expressed as a function of strains measured on the incident and transmitted bars via strain gages glued on them. From Equation 2.23,

$$\begin{aligned} \sigma &= \rho C v \\ \frac{\sigma}{E} &= \varepsilon \end{aligned} \quad (2.27)$$

Therefore the velocities of the ends of incident and transmitted bars, when the waves reach these sections, can be calculated as;

$$\begin{aligned} v_1 &= C \varepsilon_I \\ v_2 &= C \varepsilon_T \end{aligned} \quad (2.28)$$

When the incident wave reflects back at the interface between the end of incident bar and the specimen, the velocity of the interface ( $v_I$ ) can be calculated by superposing incident and reflected pulses. Hence,

$$v_I = C(\varepsilon_I - \varepsilon_R) \quad (2.29)$$

Note that  $\varepsilon_R$  has an opposite sign to that of  $\varepsilon_I$  because the reflected tension pulse induces a particle velocity in a direction opposite to its direction of propagating. Then,

$$\dot{\varepsilon} = \frac{d\varepsilon}{dt} = \frac{C(\varepsilon_I - \varepsilon_R) - C\varepsilon_T}{L_s} = \frac{C(\varepsilon_I - \varepsilon_R - \varepsilon_T)}{L_s} \quad (2.30)$$

One must note that all strain pulses (waves) that appear in this equation are functions of time, and each one is measured and recorded via a digital storage oscilloscope. The strain can be derived after integrating both sides from 0 to  $t$ :

$$\begin{aligned} \varepsilon &= \int \dot{\varepsilon} dt \\ \varepsilon &= \frac{C}{L_s} \int_0^t (\varepsilon_I - \varepsilon_R - \varepsilon_T) dt \end{aligned} \quad (2.31)$$

The forces at the incident-specimen and specimen-transmitted bar interfaces are computed as follow;

$$\begin{aligned} F_1 &= AE(\varepsilon_I + \varepsilon_R) \\ F_2 &= AE\varepsilon_T \end{aligned} \quad (2.32)$$

And the average stress in the specimen is simply given by;

$$\sigma_s = \frac{F_1 + F_2}{2A_s} \quad (2.33)$$

Then this leads to;

$$\sigma_s = \frac{A E}{2A_s} (\varepsilon_I + \varepsilon_R + \varepsilon_T) \quad (2.34)$$

where  $A_s$  and  $A$  are the cross-sectional area of the specimen and bar respectively.

The calculation of stress and strain rate in specimen like this is done with using three wave of incident, transmitted and return waves. Using these entire waves in calculation produces noise and is not always reliable because of the practical problems in obtaining clean signal recording of the reflected pulse. It must be noted at this point that both the incident pulse and the reflected pulse are measured by the same strain gages on the incident bar. Although the length of the incident pulse is kept short enough for incident pulse to completely pass over the strain gage location before the reflected wave arrives at the same location, it is often observed that incident pulse is followed by a non-zero tail noise which interferes with the measurement of reflected pulse. As a remedy to this practical problem, the condition of dynamic stress equilibrium is invoked. When the part of incident stress wave is transmitted over the specimen to the output bar just after an initial ringing up period (which is typically a few microseconds), dynamic stress equilibrium is achieved, and the stresses (as well as forces) on both side of specimen becomes equal. Then, the specimen is assumed to deform uniformly. Under these conditions, strain rate experienced by the specimen can be calculated in an alternative way as follows, which lead to what is called two-wave and one-way analyses [44].

Dynamic force equilibrium at both sides of the specimen surfaces requires that;

$$F_1 = F_2 \quad (2.35)$$

$$(\varepsilon_I + \varepsilon_R = \varepsilon_T)$$

Thus, substituting Equation 2.35 into Equation 2.34 gives,

$$\sigma_s = \frac{AE}{2A_s}(\varepsilon_I + \varepsilon_R + \varepsilon_T) = \frac{AE}{2A_s} 2\varepsilon_T \quad (2.36)$$

$$\sigma_s = \frac{AE}{A_s} \varepsilon_T$$

Then three waves can be reduced to one wave, by substituting  $\varepsilon_I + \varepsilon_R = \varepsilon_T$  into Equation 2.30;

$$\dot{\varepsilon} = \frac{-2C}{EL_s}(\sigma_T - \sigma_I) \Rightarrow \text{Two waves.} \quad (2.37)$$

$$\dot{\varepsilon} = \frac{-2C}{EL_s} \sigma_R \Rightarrow \text{One wave}$$

It must be obvious that two wave analyses is preferred since it allows calculation of strain rate without using often noisy reflected wave signals.

### 2.2.2 Shear Compression Specimen (SCS)

SCS, which has a specialized specimen geometry, has been developed by Rittel *et al* [45-46] to investigate the mechanical behavior of materials at large strains over a wide range of strain rates under a predominantly shear state of stress. Therefore, SCS geometry has been commonly used to investigate the susceptibility of different materials/microstructures to the formation of adiabatic shear bands (ASB), which are narrow bands of intense plastic shear strain typically observed in dynamic failure modes [33, 46]. The SCS is a cylindrical specimen geometry (See Figure. 3.2(b)), with two diametrically symmetric slots oriented with a specific angle to the axis of specimen to stimulate uniform shear strain and stress distribution along the narrow gage section where higher strain rates over  $10^4 \text{ s}^{-1}$  can be easily achieved as stated by Vural *et al* [47]. They also improved the specimen geometry by demonstrating that a slot angle of 35.26 degrees (See Figure 3.2(a)) promotes a uniform shear strain distribution in the gage section. All dimensions in Figure 3.2(a) are in inches. The terms  $d$ ,  $h$ ,  $t$  and  $w$  are the main geometrical constants used to determine scalar



measures of equivalent stress and equivalent strain from load-displacement measurements.

This unique specimen geometry was used in dynamic experiments to investigate the occurrence of ASB based on dynamic plastic behavior of the alloys.

### 2.3 Material Modeling

An equation which describes the flow stress of material as a function of material properties as well as the applied strain, strain rate and temperature is defined as constitutive equation/model.

Constitutive models can be categorized into phenomenological (e.g. Johnson-Cook) and physically based (e.g. Zerilli-Armstrong) models. Both phenomenological and physically based models require significant number of experiments to determine model parameters. Physically based models generally use dislocation mechanics to relate thermal and strain rate effects to the flow stress of material and tend to be significantly more complex than phenomenological counterparts. Although it sounds counter intuitive, it is not uncommon to have physics based constitutive models with more number of model parameters. On the other hand, phenomenological constitutive models tend to have a simpler form and commonly available in commercial Finite Element (FE) codes. The general form of phenomenological constitutive models can be expressed as follows:

$$\sigma = f(\varepsilon, \dot{\varepsilon}, T) \quad (2.38)$$

where  $\varepsilon$  is the strain,  $\dot{\varepsilon}$  is the strain rate and  $T$  is the temperature [19].

Therefore, rate and temperature dependent mechanical behavior of materials is described by both phenomenological and physically based models. In these models, the stress and strain are reduced to von Mises effective stress and strain by using the relations which are given below. Therefore, constitutive models are formulated by using the scalar measures of stress and strain although they are a second-order tensors [19].

$$\sigma_{eff} = \frac{\sqrt{2}}{2} [(\sigma_1 - \sigma_2)^2 + (\sigma_2 - \sigma_3)^2 + (\sigma_1 - \sigma_3)^2]^{\frac{1}{2}}$$

$$\varepsilon_{eff} = \frac{\sqrt{2}}{3} [(\varepsilon_1 - \varepsilon_2)^2 + (\varepsilon_2 - \varepsilon_3)^2 + (\varepsilon_1 - \varepsilon_3)^2]^{\frac{1}{2}}$$
(2.39)

### 2.3.1 Phenomenological (Empirical) Models

#### 2.3.1.1 Johnson-Cook (JC)

Among this type of constitutive models, Johnson-Cook model (JC) [10, 48] is the most widely used plastic flow stress model, particularly in commercial FE codes. In this model, flow stress is defined as a multiplicative decomposition of strain hardening, strain rate hardening and thermal softening terms as shown below;

$$\sigma = (\sigma_0 + B\varepsilon^n) \left( 1 + C \ln \frac{\dot{\varepsilon}}{\dot{\varepsilon}_0} \right) [1 - (T^*)^m]$$
(2.40)

where  $\varepsilon$  is the plastic strain,  $\dot{\varepsilon}$  is the strain rate,  $\dot{\varepsilon}_0$  is a reference strain rate and the homologous temperature  $T^*$  is defined as:

$$T^* = \left( \frac{T - T_0}{T_m - T_0} \right)$$
(2.41)

In this equation,  $T_0$  is the reference temperature at which  $\sigma_0$  is measured and  $T_m$  is the reference (or effective) melting temperature for the material.

This equation has five experimentally determined model parameters ( $\sigma_0$ ,  $B$ ,  $n$ ,  $C$ ,  $m$ ) that describe yield stress, strain hardening parameter, strain hardening exponent, strain rate sensitivity (SRS) and thermal softening parameters, respectively.

Since phenomenological constitutive models are empirical equations as described above their experimentally determined parameters are obtained by a "curve-fitting" procedure and each research group develops its own procedure [19]. However, JC model has some shortcomings in spite of its simplicity as stated in [10-19]:

- i. Flow stress is linearly proportional to the logarithm of strain rate. But the experiments show a marked increase in the dependence of flow stress on strain rate above a certain transition strain rate typically in  $10^3 - 10^4 \text{ s}^{-1}$  range.

ii. Since strain hardening, strain rate hardening and thermal softening terms are multiplied with each other, the stress-strain curves stretch upward by an increase in strain rate and downward by an increase in the temperature in a self-similar manner, which is not in complete agreement with the experimental observations.

iii. Vural et al. [10] experimentally show that strain hardening parameter ( $B$ ) and strain rate sensitivity (SRS) parameter ( $C$ ) have a much more complex dependence to temperature than predicted by JC model for 2139 aluminum alloy.

iv. SRS parameter ( $C$ ) is not coupled with temperature and is assumed a constant value for quasi-static and dynamic regime of plastic deformation.

To overcome all these shortcomings in standard JC model, Vural et al.[10] proposed a modified JC model (MJC), which will be discussed in the following section.

### **2.3.1.2 Modified Johnson-Cook Model (MJC)**

Different from the JC model which determines the strain hardening and SRS parameters independent of temperature, Vural et al. [10] firstly modified strain hardening parameter ( $B$ ) and SRS parameter ( $C$ ) to better model the impact of temperature variations on these parameters.

JC model implicitly assumes that the thermal softening acts on the magnitude of flow stress, i.e., that thermal softening influences both yield stress and strain hardening by the same factor. However, experimental results suggest that the strain hardening is affected by thermal softening at a higher rate than the yield stress. Therefore, at the beginning, the following modification is made to the strain hardening parameter by coupling it with normalized temperature ( $T^*$ ).

$$B = B_0 (1 - (T^*))^m \quad (2.42)$$

This relation emphasizes that thermal softening is more effective on strain hardening parameter than on the yield stress.

Next, SRS parameter ( $C$ ) was modified to reflect the influence of temperature on strain rate hardening in quasi-static regime. Experiments show that SRS of metallic

materials increases with temperature in low strain rate regime, which is in fact expected because the flow stress is largely governed by the thermal activation of dislocation glide in an Arrhenius manner. Therefore, the following modification to the SRS parameter ( $C$ ) was proposed in compliance with physical reasoning as well as experimental results. Since quasi-static regime and high strain rate regime behaviors of the materials have different strain rate dependence, it is introduced two different SRS parameters,  $C_1$  and  $C_2$  for quasi-static and high strain rate regimes, respectively.

$$C = C_1(T_r^*)^p + C_2H(\dot{\epsilon}, \dot{\epsilon}_t, k) \quad (2.43)$$

where

$$T_r^* = \left( \frac{T - T_0}{T_r - T_0} \right) \quad (2.44)$$

and

$$H(\dot{\epsilon}, \dot{\epsilon}_t, k) = \frac{1}{2} + \frac{1}{2} \tanh \left( k \ln \frac{\dot{\epsilon}}{\dot{\epsilon}_t} \right) = \frac{1}{1 + e^{-2k \ln(\ln \dot{\epsilon} / \dot{\epsilon}_t)}} \quad (2.45)$$

In these equations,  $T_0$  is the reference temperature and  $T_r$  is room temperature,  $H(\dot{\epsilon}, \dot{\epsilon}_t, k)$  is a smoothed and continuous Heaviside step function which was set up to give 1 when ( $\dot{\epsilon} > \dot{\epsilon}_t$ ) and 0 when ( $\dot{\epsilon} < \dot{\epsilon}_t$ ),  $C_1$  is the SRS parameter when ( $\dot{\epsilon} < \dot{\epsilon}_t$ ) and  $C_2$  is SRS parameter when ( $\dot{\epsilon} > \dot{\epsilon}_t$ ).

With this modification, the strain rate in quasi-static ( $\dot{\epsilon} < \dot{\epsilon}_t$ ) and high strain rate ( $\dot{\epsilon} > \dot{\epsilon}_t$ ) regimes have different slopes and represented by  $C_1$  and  $C_2$ , respectively, as shown in Figure 2.17. Here,  $\dot{\epsilon}_t$  is the transition strain rate that separates quasi-static deformation regime from dynamic one and is typically within  $10^3$  to  $10^4$  s<sup>-1</sup> range. Heaviside step function described by Equation 2.45 yields a smooth and continuous variation around the transition strain rate  $\dot{\epsilon}_t$ , which is the intersection point of two slopes seen in Figure 2.17. It is important to note that this step function ensures a smooth transition between the two different strain rate regimes, and the value of parameter  $k$  defines this transition interval. Then, a relation was described to obtain

continuity in the flow stress of material at the end of quasi-static regime and at the beginning of the dynamic regime as follows [10];

$$\hat{\sigma}_{qs}(\varepsilon_p, \dot{\varepsilon}_t |_{\dot{\varepsilon}_0}, T) = \hat{\sigma}_{dyn}(\varepsilon_p, \dot{\varepsilon}_t |_{\dot{\varepsilon}_0}, T) \quad (2.46)$$

By which, the following relation was obtained for a reference strain rate  $\dot{\varepsilon}_0$ .

$$\dot{\varepsilon}_0 = \dot{\varepsilon}_{01} \left\{ 1 + \left[ \left( \frac{\dot{\varepsilon}_t}{\dot{\varepsilon}_{01}} \right)^{(c_2)/(c_1(T_r^*)^p + c_2)} - 1 \right] H(\dot{\varepsilon}, \dot{\varepsilon}_t, k) \right\} \quad (2.47)$$

Here  $\dot{\varepsilon}_{01}$  is the reference strain rate chosen for quasi-static regime, commonly around  $10^{-4} \text{ s}^{-1}$ . With these modifications, the modified Johnson-Cook (MJC) model is expressed by following set of equations:

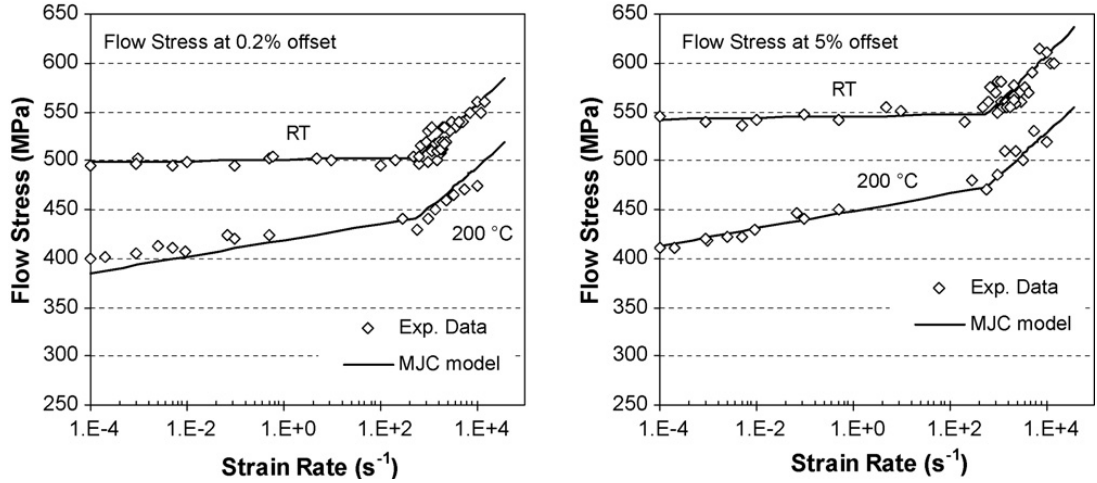


Figure 2.17 Effect of temperature on the rate sensitivity of flow stress at 0.2% and 5% offset for AA 2139-T8. Solid lines are the predictions of MJC model [10].

$$\sigma = (A + B\varepsilon^n) \left( 1 + C \ln \frac{\dot{\varepsilon}}{\dot{\varepsilon}_0} \right) [1 - (T^*)^m] \quad T^* = \left( \frac{T - T_0}{T_m - T_0} \right)$$

$$B = B_0 (1 - (T^*)^m) \quad C = C_1 (T_r^*)^p + C_2 H(\dot{\varepsilon}, \dot{\varepsilon}_t, k) \quad (2.48)$$

$$H(\dot{\varepsilon}, \dot{\varepsilon}_t, k) = \frac{1}{2} + \frac{1}{2} \tanh \left( k \ln \frac{\dot{\varepsilon}}{\dot{\varepsilon}_t} \right) = \frac{1}{1 + e^{-2k \ln(\dot{\varepsilon}/\dot{\varepsilon}_t)}} \quad T_r^* = \left( \frac{T - T_0}{T_r - T_0} \right)$$

$$\dot{\varepsilon}_0 = \dot{\varepsilon}_{01} \left\{ 1 + \left[ \left( \frac{\dot{\varepsilon}_t}{\dot{\varepsilon}_{01}} \right)^{(c_2)/(c_1(T_r^*)^p + c_2)} - 1 \right] H(\dot{\varepsilon}, \dot{\varepsilon}_t, k) \right\}$$

**2.3.2 Physically Based Models**

The dislocations are the most important carriers of plastic deformation in metals. Therefore, the constitutive models that largely rely on dislocation mechanics and thermal activation mechanisms are named as physically based models.

As a dislocation moves, a unit shear displacement  $b$  (Figure 2.18) occurs. When a set of edge dislocations move on, they produce a shear strain which is equal to the tangent of the deflection angle  $\theta$  as shown in Figure 2.18b. The mathematical representation of this process is called as Orowan equation, which is given below [19-49];

$$\gamma = \tan \theta = \frac{Nb}{l} = \frac{Nbl}{l^2} \tag{2.49}$$

where  $N$  is the number of dislocations,  $b$  is Burgers vector and  $l$  is the distance traveled by each dislocation. Taking  $\rho$  as the density of dislocations;

$$\rho = \frac{N}{l^2} \tag{2.50}$$

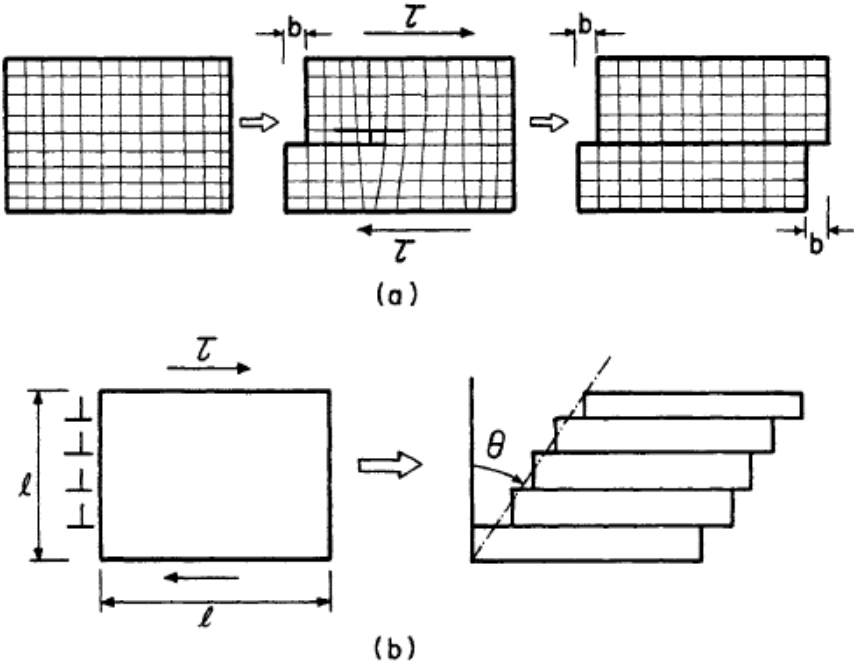


Figure 2.18 Shear produced by passage of (a) a dislocation (b) dislocation array [19-49].

Then the shear strain is described as follows [49];

$$\gamma = \tan \theta = \rho b l \quad (2.51)$$

This Orowan equation is the most important equations in micromechanics that defines the plastic shear strain as a function of the physical quantities of mobile dislocations in the microstructure of material. If it is differentiated with respect to time, the equation becomes;

$$\dot{\gamma} = \rho b v \quad (2.52)$$

where  $v$  is the dislocation velocity. On the other hand, a relationship between the shear strain and the normal strain can be obtained by adding an orientation factor  $M$  (see Meyers and Chawla [50]). Thus;

$$\gamma = M \varepsilon \quad (2.53)$$

Differentiating the above equation with respect to time gives;

$$\begin{aligned} \dot{\gamma} &= M \dot{\varepsilon} \\ \dot{\varepsilon} &= \frac{1}{M} \rho b v \end{aligned} \quad (2.54)$$

So, the strain rate can be related to the dislocation velocity ( $v$ ).

The thermal energy that increases the amplitude of vibration of atoms can cause dislocation to overcome the barriers as shown in Figure 2.5. As the temperature increase the thermal energies  $\Delta G$  increase and dislocation easily overcome the barrier (obstacle) since the effective height of barriers as seen in Figure 2.19 decreases with temperature [19].

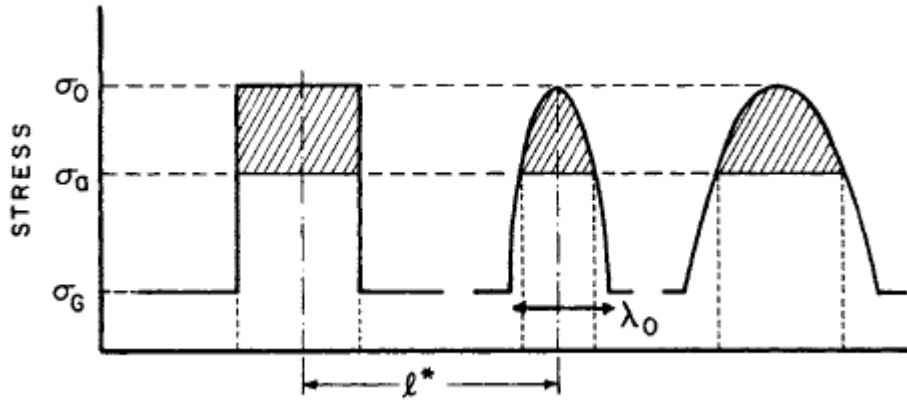


Figure 2.19 Different shapes of barriers: rectangular, hyperbolic, and sinusoidal [19-49]

The probability of a dislocation having thermal energy greater than a given thermal energy  $\Delta G$  in order to overcome the barrier is given by statistical mechanics as:

$$p = \exp\left(-\frac{\Delta G}{\kappa T}\right) \quad (2.55)$$

where  $p$  is the probability that a dislocation will overcome a barrier,  $\kappa$  is Boltzmann's constant,  $\Delta G$  is the thermal activation energy required to overcome the barrier,  $T$  is the temperature. Physically based constitutive equations are generally based on this Arrhenius expression. As the temperature increases, the probability of successful jump increases since thermal energy  $\Delta G$  provide the "kick" that increases the ratio of the number of successful jumps over the barrier divided by the number of attempts. If it is assumed that  $f_1$  is the frequency of these successful jumps and  $f_0$  is the vibrational frequency of the dislocation, then probability ( $\rho$ ) of jumping over the barrier is equal to  $f_1/f_0$  [19-49]. Thus,

$$f_1 = f_0 \exp\left(-\frac{\Delta G}{\kappa T}\right) \quad (2.56)$$

Thus, using Equation 2.54,

$$\frac{d\varepsilon}{dt} = \frac{\Delta\varepsilon}{\Delta t} = \frac{1}{M} \rho b \frac{\Delta l}{\Delta t} \quad (2.57)$$



In this equation,  $\Delta t$  is the time taken by a dislocation to move a distance  $\Delta l$  between two obstacles. The time  $\Delta t$  is decomposed into a waiting time ( $t_w$ ) in front of an obstacle and a moving time ( $t_m$ ) between the obstacles.

$$\Delta t = t_w + t_m \quad (2.58)$$

The waiting time ( $t_w$ ) can be expressed in terms of the probability ( $\rho$ ) that a dislocation will overcome a barrier using the frequency of these successful jumps  $f_1$  as follows;

$$t_w = \frac{1}{f_1} = \frac{1}{f_0} \exp\left(\frac{\Delta G}{\kappa T}\right) \quad (2.59)$$

Assumed that  $t_w \gg t_m$  as suggested by Meyer [19], then  $\Delta t \cong t_w$ .

Thus substituting Equation 2.59 and 2.57 yields,

$$\dot{\epsilon} = \frac{v_0 \rho b \Delta l}{M} \exp\left(-\frac{\Delta G}{\kappa T}\right) \quad (2.60)$$

where  $\Delta l$  is the distance between dislocation barriers. If the  $\frac{v_0 \rho b \Delta l}{M}$  term is called reference strain rate ( $\dot{\epsilon}_0$ ), the following equation is obtained,

$$\dot{\epsilon} = \dot{\epsilon}_0 \exp\left(-\frac{\Delta G}{\kappa T}\right) \quad (2.61)$$

If it is expressed in terms of thermal activation energy;

$$\Delta G = \kappa T \ln \frac{\dot{\epsilon}_0}{\dot{\epsilon}} \quad (2.62)$$

This final expression shows that thermal activation energy decreases with increasing strain rate while it increases with increasing temperature [19-49].

### 2.3.2.1 Zerilli-Armstrong (ZA) Model

The Zerilli and Armstrong [51-53] proposed a constitutive model as a function of strain, strain rate and coupled temperature depending on the thermal activation mechanism of dislocation motion discussed in preceding section. They investigated the dynamic behavior of typical body centered cubic (BCC) and face centered cubic (FCC) metals in terms of the effect of strain rate and temperature on flow stress, and it was noticed that there was a significant difference between these materials [19]. Therefore, they developed two distinct constitutive equations to describe plastic flow stress in BCC and FCC materials [54].

$$\sigma = \sigma_a + B \exp[(-\beta_0 + \beta_1 \ln \dot{\varepsilon})T] \quad \text{for BCC structured materials} \quad (2.63)$$

$$\sigma = \sigma_a + B_0 \varepsilon^{1/2} \exp[(-\beta_0 + \beta_1 \ln \dot{\varepsilon})T] \quad \text{for FCC structured materials} \quad (2.64)$$

where  $\sigma_a = \frac{k}{\sqrt{d}} + \sigma_s$ ,  $T$  is temperature,  $\dot{\varepsilon}$  is strain rate,  $\varepsilon$  is strain,  $\sigma_a$  is the athermal flow stress,  $k$  is the microstructural stress intensity,  $d$  is the average grain diameter,  $\sigma_s$  is the stress increase due to solutes and  $B$ ,  $B_0$ ,  $\beta_0$  and  $\beta_1$  are the experimental parameters based on thermal activated dislocation mechanism of two different crystal lattice structures.

It was found out that BCC metals have a stronger dependence of flow stress on temperature and strain rate as compared to FCC metals. Additionally, they noticed that overcoming Peierls–Nabarro barriers is the principal thermal activation mechanism in BCC metals, and dislocation forests are the primary short-range barrier in FCC metals. Therefore, while the thermal activation area  $A$ , the area to be moved by dislocation during overcoming the barriers, decreased with increasing strain in FCC metals (because of increasing dislocation density), it is not dependent on strain in BCC metals since the lattice spacing is unaffected by plastic strain. The difference in the nature of these short-range barriers is responsible for the major differences in strain rate sensitivity between FCC and BCC metals [19].

This activation area  $A$  is the area swept by the dislocation in overcoming a barrier depicted in Figure 2.19. It is obtained from the activation volume  $V$  as follows [19];

$$V = Ab = l^* \lambda b \quad (2.65)$$

where  $l^*$  is the distance between the barriers,  $\lambda$  is the width of the barrier as shown in Figure 2.19.  $A$  is the thermal activation area swept by the dislocation in jumping a barrier.

Since the primary obstacle (barrier) is the dislocation forest in FCC metals, the spacing of the forest dislocations ( $l^*$ ) and the thermal activation area ( $A$ ) decrease with increasing strain in FCC metals. Meyers and Chawla [50] obtained a well-known relationship between dislocation density and spacing [19].

$$\rho = \frac{1}{l^{*2}} \quad (2.66)$$

Dislocation density increases with strain as described in Equation 2.51. Assuming  $l$  is constant and using Equation 2.51, 2.65, 2.66 and an orientation factor  $M$  (see Meyers and Chawla [50]), Meyer [19], the following relationship was obtained, ( $\gamma = M\varepsilon$  and  $M\varepsilon = \rho bl$ )

$$A = \lambda l^* = \lambda \left( \frac{bl}{M} \right)^{1/2} \varepsilon^{-1/2} \quad (2.67)$$

Zerilli and Armstrong [51-53] used Orowan equation  $\dot{\gamma} = \rho b v$  ( Equation 2.52) to determine the plastic shear strain rate [51].

The activation energy  $\Delta G$  was described using Equation 2.61 as follow,

$$\Delta G = \Delta G_0 - \int_0^{\tau_{th}} A_0 b d\tau_{th} \quad (2.68)$$

where  $\Delta G_0$  is the reference activation energy at  $T=0$  K,  $A_0$  is thermal activation area at  $T=0$  K,  $b$  is the Burgers vector and  $\tau_{th}$  is the thermal component of the shear stress. Mean value of  $Ab$  can be expressed as:

$$Ab = \left( \frac{1}{\tau_{th}} \right) \int_0^{\tau_{th}} A_0 b d\tau_{th} \quad (2.69)$$

Using Equation 2.52, 2.61, 2.62, 2.68 and 2.69 with an orientation factor  $M$  (see Meyers and Chawla [50]), Meyer [19], Zerilli and Armstrong [51] proposed thermal portion of flow stress as follows,

$$\sigma_{th} = \frac{M \Delta G_0}{A_0 b} e^{-\beta T} \quad (2.70)$$

After replacing  $\frac{M \Delta G_0}{A_0 b}$  by  $B$ , the thermal component of flow stress can be expressed as;

$$\sigma_{th} = B e^{-\beta T} \quad (2.71)$$

where

$$\beta = \left( \frac{1}{T} \right) \ln \left( \frac{A}{A_0} \right) - \left( \frac{1}{T} \right) \ln \left( 1 + \left( \frac{\kappa T}{G_0} \right) \ln \left( \frac{\dot{\epsilon}}{\dot{\epsilon}_0} \right) \right) \quad (2.72)$$

$A_0$  is the thermal activation area at  $T=0$  K, and  $\dot{\epsilon}_0 = \frac{v_0 \rho b \Delta l}{M}$  (Equation 2.61). The  $B$

term is the threshold stress and it is reduced by  $e^{-\beta T}$  factor to calculate the thermal component of flow stress. Zerilli and Armstrong [51] found  $\beta$  experimentally as;

$$\beta = \beta_0 - \beta_1 \ln(\dot{\epsilon}) \quad (2.73)$$

For the BCC metals, thermal activation area ( $A$ ) is assumed to be constant since  $A$  is not affected by strain while the spacing of the obstacles in FCC metals is strongly affected by strain. For FCC metals,  $A$  is proportional to the inverse square root of strain in Equation 2.67 and So;

$$B = B_0 \varepsilon^{1/2} \quad (2.74)$$

Thus, for the FCC case, thermal component of flow stress can be expressed as:

$$\sigma_{th} = B_0 \sqrt{\varepsilon} \exp(-\beta_0 T + \beta_1 T \ln \dot{\varepsilon}) \quad (2.75)$$

Since  $A$  is constant for BCC structures and is not proportional to strain, for BCC metals the thermal component of flow stress can be defined as;

$$\sigma_{th} = B \exp(-\beta_0 T + \beta_1 T \ln \dot{\varepsilon}) \quad (2.76)$$

Zerilli and Armstrong also added the effect of the grain boundaries on flow stress by using well-known Hall-Petch equation and a term expressing the athermal component of flow stress [19, 49, 51]. Thus, the overall flow stress is expressed as;

$$\sigma = \sigma_s + \sigma_{th} + \frac{k}{\sqrt{d}} \quad (2.77)$$

From here, athermal component of flow stress;

$$\sigma_a = \frac{k}{\sqrt{d}} + \sigma_s \quad (2.78)$$

where  $k$  is the microstructural stress intensity,  $d$  is the average grain diameter and  $\sigma_s$  is the stress increase due to solutes. Thus, the final form of the ZA model is:

$$\sigma = \sigma_a + B_0 \sqrt{\varepsilon} \exp(-\beta_0 T + \beta_1 T \ln \dot{\varepsilon}) \quad \text{For FCC} \quad (2.79)$$

$$\sigma = \sigma_a + B \exp(-\beta_0 T + \beta_1 T \ln \dot{\varepsilon}) \quad \text{For BCC} \quad (2.80)$$

The primary difference between two models is that the strain is uncoupled from strain rate and temperature in BCC metals.

Zerilli and Armstrong [53] modified this equation for dynamic behavior of Hexagonal Close Packed (HCP) materials and certain alloys to include both Peierls stress type interactions and forest-dislocations type interactions in a single equation.

$$\sigma = \sigma_a + B e^{-\beta T} + B_0 \varepsilon^{\frac{1}{2}} e^{-\alpha T} \quad (2.81)$$

where

$$\alpha = \alpha_0 - \alpha_1 \ln(\dot{\varepsilon})$$

$$\beta = \beta_0 - \beta_1 \ln(\dot{\varepsilon}) \quad (2.82)$$

$$\sigma_a = \frac{k}{\sqrt{d}} + \sigma_s$$

### 2.3.2.2 Modified Zerilli-Armstrong (MZA) Model

Zerilli and Armstrong [52-53] modified their first released model (Equation 2.81) to include dynamic recovery and consequent saturation of stress-strain curve at large strains. Their first released model (Equation 2.81) shows a strain hardening,  $B_0 \varepsilon^{\frac{1}{2}} e^{-\alpha T}$ , proportional to the square root of strain that is originally derived by Taylor [55]. Later Taylor and Quinney [56] noticed the saturation of stress-strain behavior in their experiments with copper. Therefore Zerilli and Armstrong extended Taylor strain hardening to include dynamic recovery.

They revised the Taylor strain hardening as;

$$B_0 \sqrt{\frac{1}{w} (1 - e^{-w\varepsilon})} \quad (2.83)$$

where  $w$  is the probability for remobilizing or annihilating a stopped dislocation.

Then the thermal component of the ZA model, Equation 2.81 becomes:

$$\sigma_{th} = \left[ B_0 \sqrt{\frac{1}{w} (1 - e^{-w\varepsilon})} \right] e^{-\alpha T} \quad (2.84)$$

where

$$\alpha = \alpha_0 - \alpha_1 \ln(\dot{\varepsilon}) \quad (2.85)$$

Finally, Zerilli and Armstrong [54] added dislocation drag effects into their model since Follansbee [57] and Kocks [24] observed increased strain rate sensitivity (Figure 2.3) typically occurring at strain rates exceeding  $10^3 \text{ s}^{-1}$  in copper and other metals of FCC structure. Additionally it was seen that there was no observable increase in the strain rate sensitivity at strain rates up to  $10^4 \text{ s}^{-1}$  [24].

Therefore, Zerilli and Armstrong modified the model again in order to capture the increased strain rate sensitivity of FCC alloys in the dynamic regime by proposing a new drag-affected thermal stress,  $\sigma^*$ .

$$\sigma^* = 0.5\sigma_{th} \left[ 1 + \left( 1 + \frac{4C_0\dot{\varepsilon}T}{\sigma_{th}} \right)^{\frac{1}{2}} \right] e^{-\alpha T} \quad (2.86)$$

where  $\sigma_{th}$  is the  $T$  and  $\dot{\varepsilon}$  dependent component of flow stress in Equation 2.77 and

$C_0$  is the coefficient in the order of  $10^{-5} \text{ MPa/K}$ . In the quasi-static regime,  $\frac{4C_0\dot{\varepsilon}T}{\sigma_{th}}$

term will be very small and negligible, and therefore  $\sigma^*$  will be almost equal to  $\sigma_{th}$ .

However, as  $\frac{4C_0\dot{\varepsilon}T}{\sigma_{th}}$  term gets bigger and bigger in the dynamic region, the ZA

model will show the desired increased rate sensitivity in the dynamic region [58].

$$\sigma = \sigma_a + \sigma^*$$

$$\sigma_{th} = B e^{-\beta T} + \left[ A \sqrt{\left( \frac{1}{w} (1 - e^{-w\varepsilon}) \right)} \right] e^{-\alpha T} \quad (2.87)$$

$$\sigma^* = 0.5 \sigma_{th} \left[ 1 + \left( 1 + \frac{4C_0 \dot{\varepsilon} T}{\sigma_{th}} \right)^{\frac{1}{2}} \right]$$

where;

$$\alpha = \alpha_0 - \alpha_1 \ln(\dot{\varepsilon})$$

$$\beta = \beta_0 - \beta_1 \ln(\dot{\varepsilon})$$

### 2.3.3.3. Vural-Turkkan Modifications to ZA Model

Vural and Turkkan [58] assumed that mean free path for the immobilization of mobile dislocations will be effectively altered by increasing temperature when the effect of diffusion process on threshold stress is taken into account. Thus the thermal component of stress was modified as:

$$\sigma_{th} = \left[ A(T) \sqrt{1 + \frac{1}{w} (1 - e^{-w\varepsilon})} \right] e^{-\alpha T} \quad (2.88)$$

where  $A(T)$  is a material specific temperature dependent parameter which decreases with increasing temperature.

Considering all modifications, they modified MZA model as:

$$\sigma = \sigma_a + \sigma^*$$

$$\sigma_{th} = \left[ A(T) \sqrt{1 + \frac{1}{w} (1 - e^{-w\varepsilon})} \right] e^{-\alpha T} \quad (2.89)$$

$$\sigma^* = 0.5 \sigma_{th} \left[ 1 + \left( 1 + \frac{4C_0 \dot{\varepsilon} T}{\sigma_{th}} \right)^{\frac{1}{2}} \right] e^{-\alpha T}$$



where

$$\alpha = \alpha_0 - \alpha_1 \ln(\dot{\epsilon})$$

$$A(T) = A \left( 1 - \left( \frac{T - T_0}{T_m - T_0} \right)^p \right) \quad (2.90)$$

With these modifications, they were able to capture the rate dependent behavior of flow stress at both room temperature and elevated temperatures for Al-Cu alloys.



## CHAPTER 3

### EXPERIMENTAL WORK

This chapter briefly discusses the materials used in this research, quasi-static and dynamic (high strain rate) compression experiments at conducted by using a servo hydraulic test machine and Split Hopkinson Pressure Bar (SHPB) setup, respectively.

#### 3.1 Materials

The four materials investigated in this study were 5083-H131 (MIL-A-46027), 7039-T64 (MIL-A-46063), 2519-T87 (MIL-DTL-46192) and 2139-T8 (MIL-DTL-32341), which will be referred to as 5083, 7039, 2519 and 2139, respectively throughout the remainder of thesis.

5083 and 7039 aluminum armor materials were ordered form a commercial vendor (Clifton Steel Company, Maple Heights, OH, USA) in plate form (1in. x 12in. x 12in.). The other two alloys, 2139 and 2519, were supplied from the U.S. Army Research Laboratory (ARL, Aberdeen Proving Ground, MD, USA) for ongoing research program in Mechanical, Materials and Aerospace Engineering Department of IIT. Specimens were machined from these plates in the machine shop of IIT, and quasi-static and dynamic experiments were performed at Fatigue and Dynamic Testing Laboratories of IIT, respectively.

The overall compositions and mechanical properties of the materials are summarized in Tables 3.1 and 3.2 based on suppliers' acceptance test documents or material's military specifications.

The major alloying element in 5083 is magnesium while 7039 contains magnesium and zinc as the principal alloying elements. On the other hand, 2519 and 2139 both

contain copper as the major alloying element. But they have differences in detail that 2519 additionally contains zirconium while 2139 has silver.

Table 3.1 Chemical compositions of aluminum alloys (values in wt.%)

Material <sup>1</sup>	Cu	Mg	Mn	Fe	Si	Cr	Zn	Ag
5083-H131		4.5	0.58	0.23	0.11	0.08	0.02	
7039-T64		2.8	0.58	0.12	0.04	0.19	3.9	
2519-T87 <sup>2</sup>	5.3	<0.4	<0.5	0.3	0.25		<0.25	
2139-T8 <sup>2</sup>	4.5	0.8	0.6	0.15	0.1		0.25	0.6

<sup>1</sup> The remainder of the composition for each alloy is aluminum.

<sup>2</sup> The composition is based on Military Specification of the alloy.

Table 3.2 Mechanical properties of aluminum alloys [55]

Mechanical property	5083	7039	2519	2139
Yield tensile stress (MPa)	255	351	400	441
Ultimate tensile stress (MPa)	310	413	469	461
Density	2.66	2.73	2.81	2.81
Ductility %	9.3	13.6	12.4	11.7

As a result, these four types of alloys have different major alloying elements and strengthening mechanisms. Table 3.3 summarizes the various major alloy chemistries and the strengthening mechanism employed in that alloy.

Table 3.3 Major alloying elements and strengthening mechanisms

Alloys	Alloying Elements	Strengthening Mechanism
5083	Al-Mg	Homogeneous solute solution
7039	Al-Zn-Mg	Heterogeneous $\eta'$ , $\eta$ (MgZn <sub>2</sub> ) precipitates
2519	Al-Cu	$\theta'$ (Al <sub>2</sub> Cu) precipitates
2139	Al-Cu-Mg-Mn-Ag	Homogeneous, Al <sub>20</sub> Cu <sub>2</sub> Mn <sub>3</sub> dispersoids, $\Omega$ (Al <sub>2</sub> Cu)

### 3.2 Aluminum Alloys

It is known that Aluminum alloy armor studies have started after the accidental discovery of aluminum alloys' heat-treatable capability by German researcher Alfred Wilm in 1908. He developed age hardenable alloy, duralumin which shows a high strength-to-weight ratio, toughness, and fatigue resistance as compared to the other materials. By this discovery, its applications spread more than expected from aircraft industry to the airships. This alloy was designated 2017 and is the ancestor of the 2xxx series of aluminum alloys. After this discovery, a number of heat treatable aluminum alloy systems were developed by a series of researches including aluminum-magnesium-silicon (6xxx series), aluminum-magnesium-copper (2xxx series) and aluminum-magnesium-zinc (7xxx series) [59-60]. As the new developments arose in the aluminum industry, uniform temper designations were established and described by the Aluminum Association according to its ANSI H35.1 standard. Basic temper designations of wrought aluminum alloys includes the letters of F, O, H, W and T indicating the general process of the product manufacturer or heat treatment as shown in Table 3.4. These letters follows the alloy by after a hyphen such as 2xxx-H. Subdivisions of the basic tempers are shown by one or more digits following the letter such as 5xxx-H131 for strain hardenable alloy and 2xxx-T87 for heat treatable alloys [61].

Table 3.4 Basic temper designations per ANSI H.35.1 standard [61-62].

Letter	Description
F	As fabricated and no mechanical properties specified
O	Annealed to obtain lowest strength temper
W	Strain-hardened wrought products with or without additional thermal treatment
H	Solution heat treatment
T	Thermally heat-treatment to produce stable tempers other than F, O or H

Wrought aluminum alloys of the 1xxx, 3xxx and 5xxx series are strain hardenable and but not heat treatable. Temper designation for wrought strain hardenable alloys are tabulated in Table 3.5 [61].

Table 3.5 Basic temper designations per ANSI H.35.1 [61].

Temper	Description
H1	Strain hardened only
H111	Annealed and cold worked by small amount
H112	Slightly strain hardened
H116	Specially fabricated, controlled strain, corrosion resistant temper
H11	Strain hardened by 1/8
H12	Strain hardened by 1/4
H3	Strain hardened and stabilized to improve ductility
H4	Strain hardened and lacquered or paint

Wrought aluminum alloys of the 2xxx, 6xxx and 7xxx series are heat treatable. Temper designation for wrought heat treatable alloys are tabulated in Table 3.6 [62].

Table 3.6 Basic temper designations per ANSI H.35.1 [62].

Temper	Description
T1	Cooled from an elevated temperature shaping process and naturally aged
T2	Cooled from an elevated temperature shaping process, cold worked and naturally aged
T3	Solution heat treatment, cold worked and naturally aged.
T4	Solution heat treatment, and naturally aged.
T5	Cooled from an elevated temperature shaping process, and artificially aged
T6	Solution heat treatment, and artificially aged.
T7	Solution heat treatment, and artificially overaged.
T8	Solution heat treatment, cold worked and artificially aged.
T9	Solution heat treatment, artificially aged and cold worked.
T10	Cooled from an elevated temperature shaping process, cold worked and artificially aged

### 3.3 Test Specimens

Both cylindrical compression specimen and shear compression specimens (SCS) were obtained by machining from as received plates of the dimensions, 12inch x 12inch x 1inch. All of the specimens were cut in in such a way that loading axis of specimen coincided with the rolling direction of aluminum plates as seen in Figure 3.1. This was done with great care to avoid any texture effects in experimental test results.

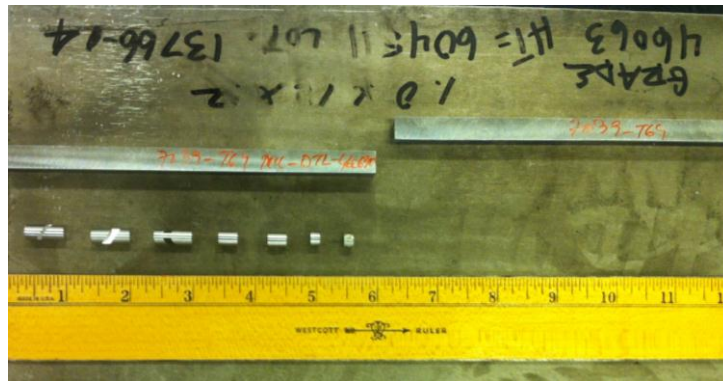


Figure 3.1 Test specimens cut from plate in rolling direction

Cylindrical compression specimens were machined to final dimensions of 7.62 mm and 3.81 mm in length and 6.35 mm in common diameter to obtain two different aspect ratios of 1.2 and 0.6, respectively as presented in Figure 3.1.

The aspect ratio (length (L)-to-diameter (D) ratio ) of 0.6 was only used in high strain rate (dynamic) experiments to achieve the highest possible strain rates close to  $10^4 \text{ s}^{-1}$ .

Three types of SCSs were machined to obtained strain rates from  $10^3$ - $10^5 \text{ s}^{-1}$  with different gage lengths ( $w$ ) and thickness ( $t$ ) such as 0.1, 0.05 and 0.025 inch.

These rather small specimen dimensions are used because of the size limitation in dynamic SHPB experiments and in order to provide consistency between dynamic and quasi-static experiments.

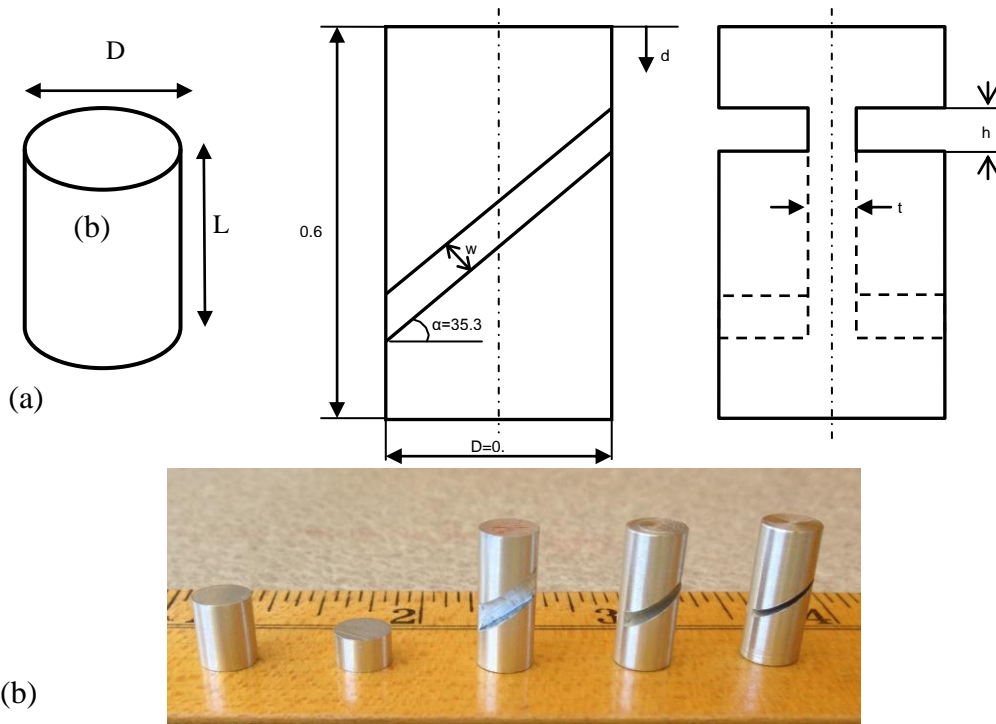


Figure 3.2 Specimens used in experiments (a) cylindrical compression specimen and shear compression specimen (SCS). All dimensions are in inches (b) A picture of samples specimens of all kinds with different aspect ratios and gage widths.

SCSs are obtained by machining from the aluminum armor plates in rolling direction. Their gage widths are measured by an optical comparator to determine the actual value after machining, which are later used in post-processing of experimental data. SCSs were deformed up to various equivalent strain levels such as 15%, 25%, 45% etc. under controlled loading conditions in order to quantitatively investigate the propensity of different microstructure to the formation of adiabatic shear banding (ASB) in SHPB. For this reason, special fixtures called stop rings (shown in Figure 3.3) were machined to specific dimensions to subject specimens gage sections to a predefined equivalent strain. Thus, minimum of three stop rings were prepared in order to obtain SCSs subjected to various levels of strains before and after the onset of shear localization of that alloy. The stop ring is a hollow tube made of C250 maraging steel with a length of tube slightly shorter than SCS length such that the maximum strain experienced by the specimen is limited to a predetermined value. When this predetermined strain level is achieved in a dynamic test, the rest of stress wave loading is transmitted through stop ring to the output bar without inducing any more strain in the specimen, which is the main and only



function of the stop ring. The stop ring was strengthened by heat treatment at 500 °C for 12 hours and then air cooled to room temperature. After annealing, the stop ring was placed on to the end of the transmitted bar using CA (Cyanoacrylate) adhesive. This type of adhesive was needed to minimize the inertial effects between stop ring and transmitted bar. When the SCS which is placed within stop ring as shown in Figure 3.3 deforms to a predetermined displacement ( $\delta$ ), the incident bar comes into contact with the stop ring. Once the contact is made, the remaining compressive stress pulse is elastically transmitted through the stop ring to the transmitted bar in order not to cause any further plastic deformation in the SCS.

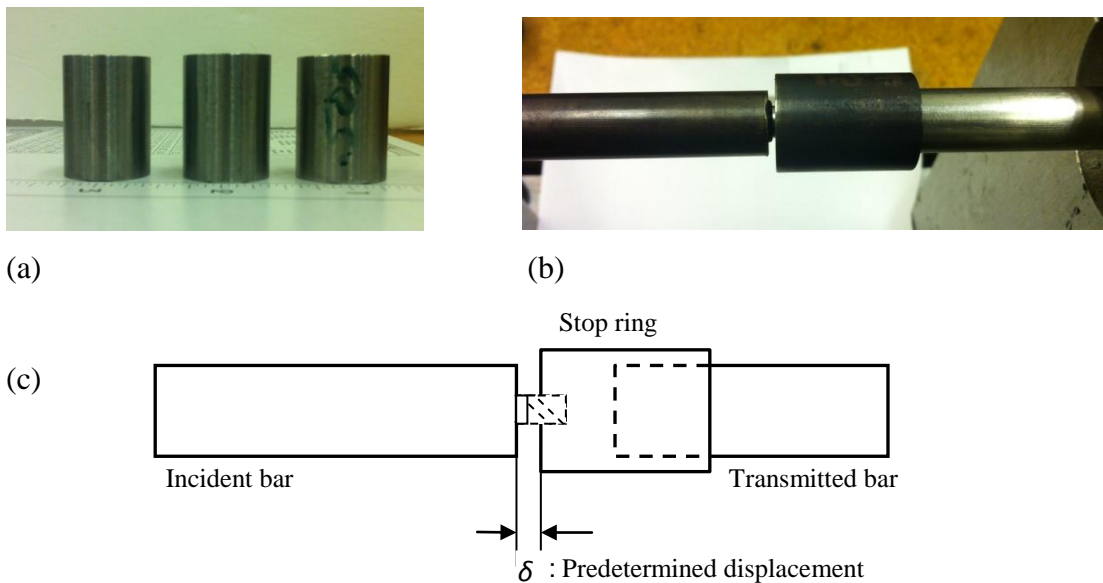


Figure 3.3 A view of stop rings (a) alone (b) installed on SHPB (c) sketch

### 3.4 Uniaxial and Shear Compression Loading Experiments

Specimens were subjected to both quasi-static and high strain rate deformations through uniaxial and shear compression separately in order to understand and evaluate the interaction between microstructure and deformation substructure under various states of stress such as compression and shear-compression.

The uniaxial quasi-static and high strain rate experiments are planned as compressive tests instead of tensile tests to take advantage of compressive tests in achieving larger strains and strain rates as compared to tensile test because of geometric instability problems (such as necking) inherently encountered in tension tests. Compressive tests are the convenient method for determining the dynamic

behavior of materials at large strains and high strain rates as stated in ASM Metals Handbook [63].

### 3.4.1 Quasi-static Loading Experiments

The quasi-static experiments at room and elevated temperatures were conducted by using MTS 973 Servo Hydraulic Test Frame (with load capacity of 535kN and Flex Test SE Controller) shown in Figure 3.4 over a range of quasi-static strain rates from  $10^{-3}$  to  $10^0$  s<sup>-1</sup>(from low to medium strain rate). In order to establish a controlled experimental set-up,

- Tungsten carbide rods which were used to ensure the loading rods are aligned perfectly with each other in order to minimize any unwanted shear forces on the specimen-loading rod interfaces.

- A high temperature extensometer, MTS 632.53E-14 Extensometer, was attached to the rods to measure the displacement directly from these rods in all quasi-static strain rates. The gage length of the extensometer whose accuracy meets ISO 9513 Class 0.5 is 0.5 inch while its maximum travel is between -0.05 in. and +0.1 in.

- Displacement data was collected via both the extensometer and crosshead LVDT (Linear Variable Differential Transducer) of the loading machine. Displacement data obtained from the extensometer is more accurate than the LVDT data from the crosshead, however the former is limited to smaller strains (up to 17%) while the latter has a much larger range.

Therefore, extensometer data is used for the strains less than 17%, and the data is combined with LVDT data in experiments where strain exceeded the range of extensometer. In some experiments, especially at the strain rates of  $10^{-1}$  and  $10^0$  s<sup>-1</sup>, some slippage has been observed between the two legs (alumina rods) of extensometer. Therefore, the displacement data is carefully examined after each test for this situation by plotting a linear graph of displacement measured from extensometer vs. displacement measured from crosshead LVDT. If there wasn't any linearity between these values, then crosshead's displacement was used. For the other cases, the data from the extensometer was used directly or used after making some correlation.

- The load was measured via load cell built in the loading frame.

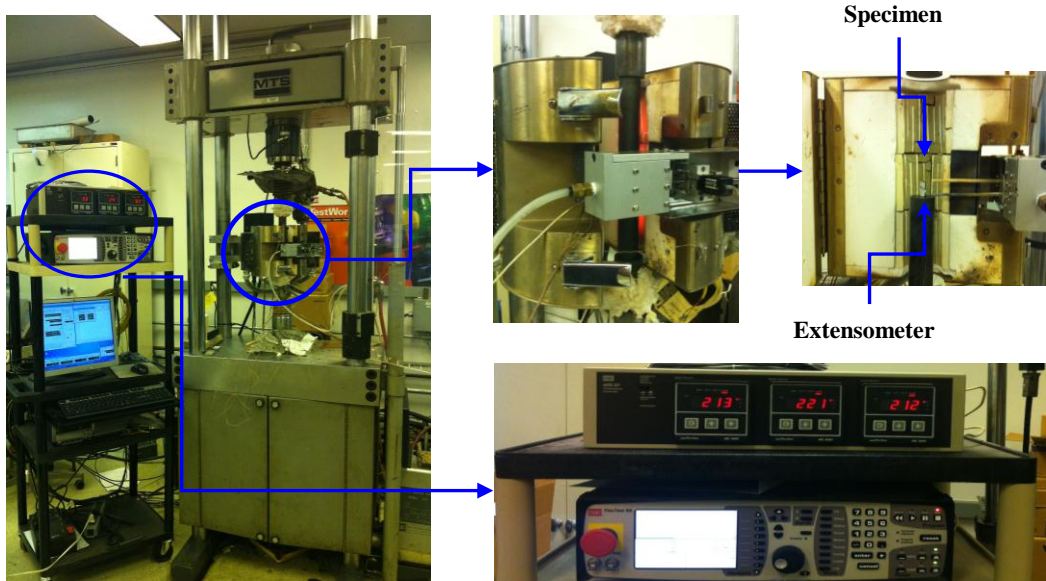


Figure 3.4 MTS 793 Servo Hydraulic test machine with installed heating chamber.

As a result, the machine was well calibrated to achieve good repeatability accuracy. In order to check repeatability accuracy of the machine, several experiments were conducted at various strains rates. The results are shown in Figure 3.5 that exhibits good repeatability accuracy.

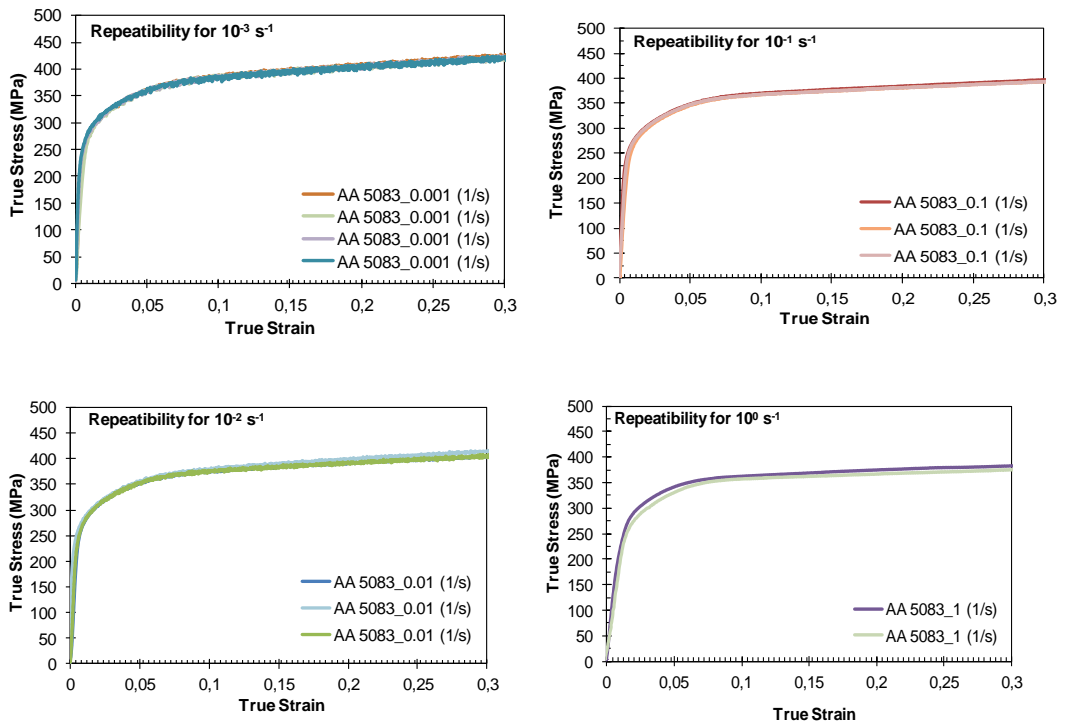


Figure 3.5 Repeatability check results of MTS 793 Servo Hydraulic Machine

All these repeatability experiments ensured that test procedure, material response and the machine calibration were consistent.

For elevated quasi-static experiments, a heating chamber that was made up of three ceramic heaters group( located as lower, middle and upper) was used to heat the specimens to elevated temperatures and these three heating units were controlled by a Proportional Integral Derivative (PID) controller through three thermocouples. One of the thermocouples was directly attached to the specimen through a high temperature silicone O-ring as it is shown in Figure 3.6. The other two were attached directly to the ends of the tungsten carbide rods near the specimen. By this configuration, it took approximately 6 minutes to reach 120 °C and 11 minutes to reach 220 °C.



Figure 3.6 Specimen and silicone O-ring configuration to attach the thermocouple to the specimen

Before each experiment, molybdenum disulfide ( $\text{MoS}_2$ ) grease was applied to the top and bottom surfaces of the specimens to minimize the friction between the crosshead anvils and the specimen.

The length ( $L$ ) and diameter ( $D$ ) of specimen were measured before each experiment to later use in true stress and true strain calculations via Equations 3.9 and 3.10 as outlined below:

$$\text{Engineering Stress} \quad S = \frac{P}{A_0} \quad (3.1)$$

$$\text{Engineering Strain} \quad e = \frac{\Delta L}{L_0} \quad (3.2)$$

where  $A_0$  is the initial cross-sectional area,  $L_0$  is the initial gage length, and  $P$  is the force measured from load cell of the machine. Then, true stress and strain was calculated as follows:

True stress is computed by dividing the load  $P$  by current cross-sectional area  $A$ . By following the assumption that volume is preserved during plastic deformation, then;

$$AL = A_0L_0$$

$$A = \frac{A_0L_0}{L} \quad (3.3)$$

at any given time, the true stress is;

$$\sigma = \frac{P}{A} \quad (3.4)$$

Then after substituting Equation 3.3 into Equation 3.4,

$$\sigma = \frac{PL}{A_0L_0} = \frac{P}{A_0}(1+e) = S(1+e) \quad (3.5)$$

True strain is the strain obtained by summing up the ratios of infinitesimal length change to the current gage length. True strain, which is also referred to as natural or logarithmic strain, is defined in incremental form as follows:

$$\frac{dL}{L} = d\varepsilon \quad (3.6)$$

The total true strain is obtained simply by integrating both sides;

$$\varepsilon = \int_0^\varepsilon d\varepsilon = \int_{L_0}^L \frac{dL}{L} = \ln \frac{L}{L_0} \quad (3.7)$$

Since engineering strain rate is infinitesimal change of strain with respect to infinitesimal time, it is defined as follows;

$$\dot{\epsilon} = \frac{de}{dt} = \frac{dL/dt}{L_0} = \frac{V}{L_0} \quad (3.8)$$

In conclusion, true compression strain ( $\epsilon$ ) and true compression stress ( $\sigma$ ) is computed after each compressive experiment by using the engineering strain ( $e$ ) and engineering stress ( $S$ ) as follows :

$$\epsilon = \ln(1 - |e|) \quad \text{for compression strain} \quad (3.9)$$

$$\sigma = S(1 - |e|) \quad \text{for compression stress} \quad (3.10)$$

Here, in Equations 3.9 and 3.10,  $e$  is engineering compression strain which is inserted in the equations with an absolute value in order to avoid possible mistakes in the sign.

### 3.4.2 High Strain Rate Experiments

Dynamic compression experiments were conducted using Split Hopkinson Pressure Bar (SHBP) setup located in Dynamic Testing Laboratory of IIT, which is shown in Figure 3.7. The striker, incident and transmitted bar lengths in the SHPB are 460 mm, 1270 mm and 980 mm, respectively, with a common diameter of 12.7 mm. The material of all bars are precision ground high-strength C350 maraging steel (with a tensile yield strength of 2275 MPa) in accordance with MIL-S-46850D. In each dynamic experiment, molybdenum disulfide ( $\text{MoS}_2$ ) grease was applied to both ends of the specimen to minimize the frictional effects. Additionally, a piece of tissue paper was used as a pulse shaper by putting it between the striker bar and incident bar before each test. For the elevated temperatures, a homemade split furnace was used to heat the specimen. The temperature of the specimen was directly measured by thermocouples on the specimen which were cemented with high temperature chemical set cement (Omegabond 700). The heating process is controlled and set to elevated temperatures by a PID controller.



Figure 3.7 A view of SHPB at Dynamic Testing Laboratory of IIT

### 3.4.3 Instrumentation

In order to measure the incident, transmitted and reflected stress pulses; axial strains on the bars should be correctly measured and decoupled from potential bending waves that might result from the misalignment and/or imperfect straightness of the bars.

For this reason, a pair of foil type strain gages (WK-06-250BF-10C) were used on the diametrically opposite faces of bars in SHPB setup to record only the axial strains associated with the stress waves in the bars. The strain gages are connected in Wheatstone half-bridge configuration shown in Figure 3.8 to cancel any bending effects.

The strain gages used in the system were  $1000 \pm 0.3$  Ohms with  $2.03 \pm 0.3$  gage factor. In Wheatstone half-bridge configuration; two strain gages were mounted on the opposite sides of bridge so that the voltage output reading will be doubled to increase signal-to-noise ratio, yet any possible bending effect will be automatically eliminated.

Such that;

$$R_1 = R_3 = R_{sg} = R - \Delta R \quad (3.11)$$

here  $R = R_2 = R_4$

The resistance of the dummy resistors ( $R_2$  and  $R_4$ ) on the other legs of the bridge was almost the same as the resistance of the strain gages. During the dynamic SHPB tests, compression of the bars results in a the change of resistance,  $\Delta R$ , in the strain gages [64].

The relation between the voltage output  $V_{data}$  in the Wheatstone bridge and the excitation voltage  $V_E$  from the power supply, which is generally 18 Volts, is

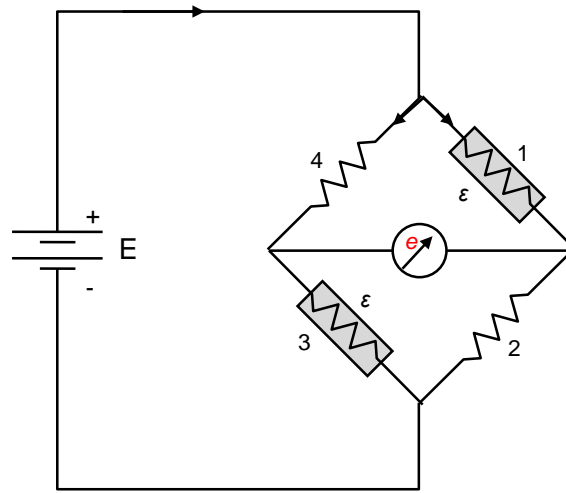


Figure 3.8 Wheatstone half- bridge

$$V_{data} = \left( \frac{R_1}{R_1 + R_2} - \frac{R_4}{R_3 + R_4} \right) V_E \quad (3.12)$$

Substituting Equation 3.11 into Equation 3.12, then the relation in terms of resistance of strain gages and the change in resistance of this value due to the compression or tension waves in bars were obtained;

$$V_{data} = \frac{\Delta R/R}{2 + \Delta R/R} V_E \approx \frac{1}{2} \frac{\Delta R}{R} V_E \quad (3.13)$$

Recalling the gage factor ( $GF$ ) of the strain gage as;

$$GF = \frac{\Delta R}{R} \frac{1}{\varepsilon} \quad (3.14)$$



where  $\varepsilon$  is the strain, then substituting the gage factor ( $GF$ ) definition into Equation 3.13 gives;

$$\varepsilon = \frac{2.V_{data}}{GF.V_E} \quad (3.15)$$

where  $V_E$  is the excitation (supply) voltage from the power supply while  $V_{data}$  is the voltage output measured from the Wheatstone bridge through a high bandwidth (5 MHz), high resolution (14-bit) digital storage oscilloscope (Nicolet Odyssey XE with OD-200 differential amplifier/acquisition cards). Finally the magnitude of elastic stress wave was calculated as;

$$\sigma = \frac{2.E_{bar}.V_{data}}{GF.V_E} \quad (3.16)$$

The stresses in both bars were calculated by Equation 3.16 where  $E_{bar}$  is the elastic modulus of the bar (194 GPa),  $V_E$  is the excitation (supply) voltage from power supply,  $V_{data}$  is the reading voltage from the oscilloscope and the  $GF$  is the gage factor of the strain gage.

#### **3.4.4 Constructing Dynamic Stress-Strain Plots from SHPB Data**

Dynamic tests conducted on the SHPB setup were done at a strain rate range of  $10^2$  to  $10^4$   $s^{-1}$  by adjusting the striker bar speed. Raw stress wave data recorded by digital storage oscilloscope in a typical SHPB experiment is shown in Figure 3.8. The blue curve contains the incident and reflected stress waves detected by the strain gages on the input bar while the red curve is transmitted stress wave recorded by the strain gages on output bar.

The raw data shown below in Figure 3.9 have high frequency noise superimposed on the real data while the test was running. Hence, they must be filtered. Typical stress wave signals that were obtained after filtering are shown in Figure 3.10.

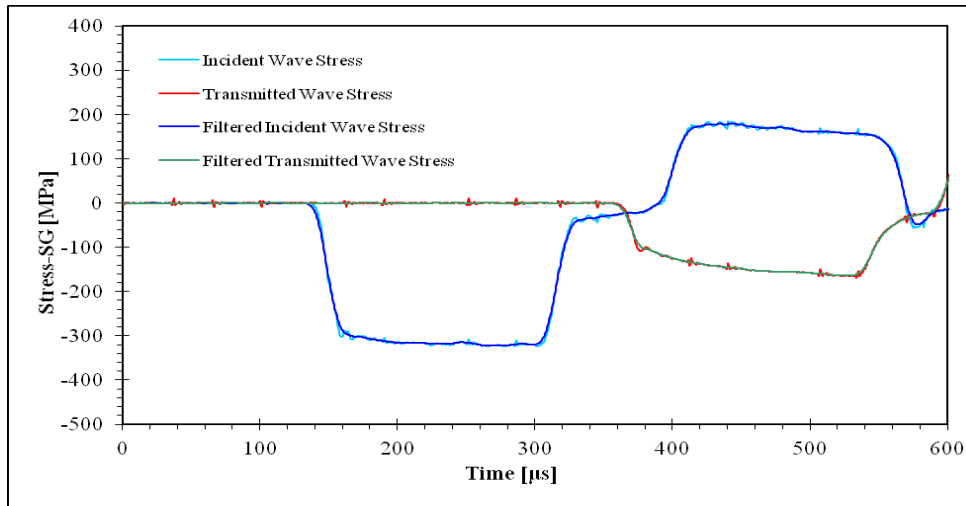


Figure 3.9 Raw and filtered stress wave data recorded by digital oscilloscope

It must be noted that incident stress wave shown in Figure 3.9 is recorded before the stress wave arrived at the specimen. Similarly, reflected and transmitted waves are recorded with a certain time lag after they emerged from the specimen. These stress signals must be time shifted to obtain the picture when they are interacting with the specimen and causing dynamic deformation as shown in Figure 3.10. The time shifted stress wave signals were calculated by the Equation 3.16 and are given in Figure 3.9 where reflected stress wave is proportional to strain rate and transmitted stress wave signal is proportional to time-resolved stress experienced by the specimen.

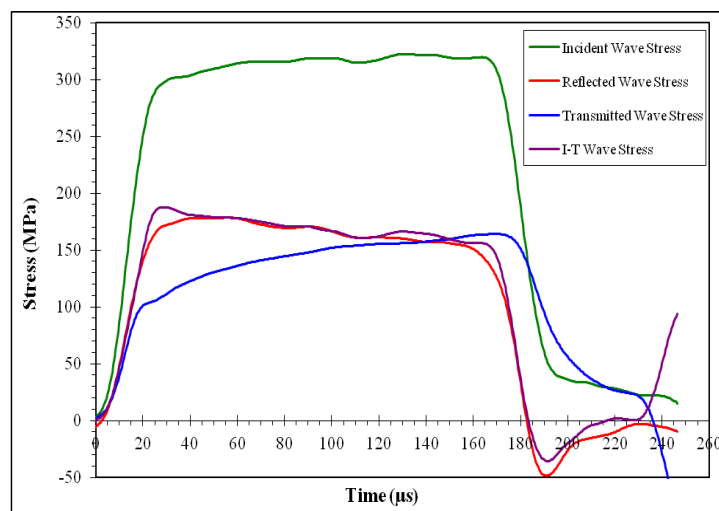
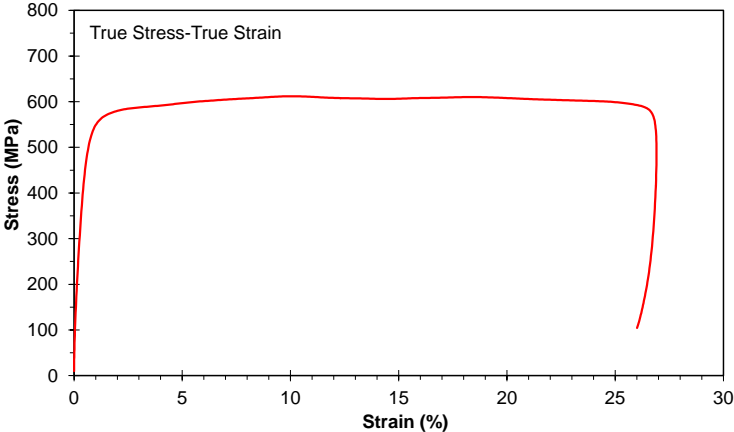


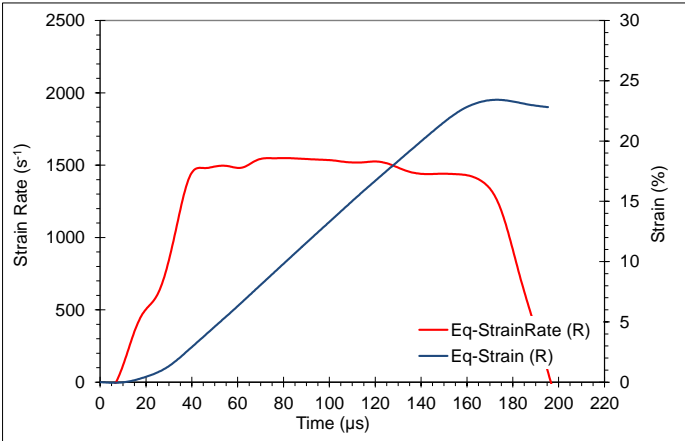
Figure 3.10 Stress waves after time shifting and filtering raw data obtained from digital oscilloscope

A typical true dynamic stress-strain plot which was obtained using the Equations 2.34 and 2.35 is shown in Figure 3.11.

In order to determine strain rate and flow stresses at %2, %5,%10 and %15 offset strains, the intersection points of the line were taken parallel to the unloading part of the of true stress-true strain rather than the loading part of this curve. This is because the dynamic stress equilibrium is not established and the strain rate is not constant at the beginning of deformation where the strain rate starts from zero and increases in a very short period of time and then becomes almost constant throughout the deformation as it is seen in Figure 3.11(b).



(a)



(b)

Figure 3.11 (a) True stress-true strain curves after analysis (b) Time resolved evaluation of strain rate and strain

### 3.5 Metallographic Preparation and Etching of Aluminum Alloys

After these controlled experiments, the recovered SCS's were sectioned in half across the gage section in order to quantitatively investigate the propensity of different microstructures to formation of adiabatic shear banding. To this end, 18 stop rings of varying dimensions were used to obtain minimum three different total strains in the gage section of SCSs of different slot widths for each alloy.

The recovered SCSs were carefully sectioned parallel to the axis of deformation by machining. For metallographic preparation and etching of aluminum alloys, there are many methods discussed in literature. Although all the methods specified in [65] were tried in all alloys, some of them worked only for one or two alloys simultaneously. For the materials used in this work, after many trials and errors, a common metallographic preparation and etching method for 5000, 7000 and 2000 series aluminum alloys was developed. Then, this procedure outlined below was applied to all alloys used in this work and it worked well in all.

Firstly, the plane grinding as shown in Figure 3-12(a) was done by using 240, 320, 400 and finally 600 grit silicon carbide grinding papers. Then the surfaces of samples were polished in high speed mode by suspension solution with approximately 1  $\mu\text{m}$  size alumina particles. Finally, a double etching technique developed by Zwieng [66] which is defined in Table 3.7 was used to prepare specimen surfaces for optical microscopy and explore the deformation substructure in the gage section of SCSs.



(a)



(b)

Figure 3. 12 Tools used in metallographic preparation and etching of aluminum alloys (a) grinding (b) polishing (c) etching (d) inverse metal optical microscopy



(c)



(d)

Figure 3. 12 Continued

Table 3.7 Double Etching Composition and Procedure [66]

Parameter	1 <sup>st</sup> Etch	2 <sup>nd</sup> Etch
Etchant	100 ml distilled water + 2 g sodium hydroxide	4 g potassium permanganate +1 g sodium hydroxide dissolved in 100 ml distilled water
Temperature	Room temperature	Room temperature
Time	1 min	15 seconds
Comments	Immersion etching.	Immersion etching. Dry etching. Always fresh etchant was used. Etching was complete when the specimen has a yellow-green color. But the immersion time was defined by trial and error depending on the deformation of SCS.

### 3.6 Test Matrix

The following Table 3.8 summarizes the test matrix used to investigate the dynamic behavior of aluminum alloys (5083, 7039, 2519 and 2139) and establish a robust experimental database to be used for developing constitutive models over a wide range of strain rates and temperatures.

Almost every test was done several times to get robust results and minimize the experimental errors coming from the test parameters' conditions.

Table 3.8 Test Matrix (Number of experiments carried out)

Test Type	Specimen Type	$\dot{\epsilon}$ (s <sup>-1</sup> )	Temp. °C	5083	7039	2519	2139
Quasi-static	Cylindrical L/D=1.2	10 <sup>-3</sup> -10 <sup>0</sup>	RT, 170, 220, 270, 320, 370	123	86	112	113
	Cylindrical L/D=1.2 L/D=0.6	10 <sup>2</sup> -10 <sup>4</sup>	RT and 220				
High Strain Rate	SCS*(w=0.1")	10 <sup>-3</sup>	RT and 220	65	59	42	56
	SCS(w=0.05")	10 <sup>3</sup> -10 <sup>5</sup>					
	SCS(w=0.025")						
ASB	SCS (w=0.1")	5X10 <sup>-3</sup>	RT	4	3	3	3
Total Number of Experiments				669			

For a given test condition, i.e., at a given strain rate and temperature, almost every test was done several times to get robust results, continuously monitor the repeatability of results, and minimize potential experimental errors.

## CHAPTER 4

### EXPERIMENTAL RESULTS

In this chapter, the results of quasi-static and high strain rate experiments performed at both room and elevated temperatures are discussed for each alloy to understand and characterize their thermal softening, strain hardening and strain rate sensitivity behaviors. Finally, based on the experimental results and observations, each one of these mechanisms will be evaluated to develop a comprehensive analysis of the dynamic deformation behavior of these alloys.

#### 4.1 Quasi-static and Dynamic Experimental Results and Discussion

All experiments needed to characterize and model the constitutive behavior of 5083, 7039, 2519 and 2139 aluminum alloys have been completed at various strain rates and elevated temperatures according to the test matrix presented in Table 3.8. All data presented for compression experiments were obtained from cylindrical specimens deformed to medium strains (typically below 20%) where low barreling and uniform deformation conditions prevailed. All stress-strain curves were plotted as true strain and true stress (in MPa). Experimental results for these materials under uniaxial quasi-static and dynamic loadings were discussed in following subsections.

##### 4.1.1 Quasi-static Experiments

###### 4.1.1.1 Thermal Softening

The true compressive stress-strain curves for aluminum alloys deformed at various temperatures at a reference strain rate of  $10^{-3} \text{ s}^{-1}$  are shown in Figure 4.1. The effect of increasing temperature on facilitating dislocation motion is quite apparent in these graphs as it significantly decreases the flow stress of all aluminum alloys. As the deformation temperature rises, the thermal activation energy that favors overcoming

short-range barriers to dislocation motion increases, while the stress needed to overcome these obstacles decreases monotonically as expected. It also affects the strain hardening behavior of alloys by decreasing and eventually completely eliminating strain hardening capacity.

For example, it is not observed any strain hardening at 220 °C degree for 5083 and 7039 and similarly at 170 °C degree for 2519 and 2139 where a transition from strain hardening to almost elastic-perfectly plastic behavior occurs. Such a transition indicates the onset of dynamic recovery at the beginning of plastic deformation at these temperatures leading to an equilibrium between the rates of dislocation multiplication and annihilation, which results in a stress plateau. As the temperature goes up to 370 °C degrees, increased thermal energy further helps dislocation motion, thereby further reducing the flow stress. Some strain softening observed particularly in 2519 and 2139 alloys above 170 °C degree indicates the existence of severe dynamic recovery of the dislocations and even dynamic recrystallization (DRX), which effectively decreases the density of dislocations with increasing strain.

Temperature dependent flow stress curves presented in Figure 4.1 also provides the necessary data to model the thermal softening behavior of these aluminum alloys. To this end, flow stress at 10% offset plastic strain is extracted from each stress-strain curve at varying temperatures to construct the thermal softening plots. The resulting thermal softening behavior for each alloy is presented in Figure 4.2, which will later be instrumental in modeling the thermal softening component of constitutive modeling effort.

The flow stress of the metals is determined by the resolved shear stress that is required to make the dislocations glide in their slip planes. If it is assumed hypothetically that there are no obstacles in the microstructure, the flow stress would be so small since the dislocations would move under infinitesimally small stresses. However, in reality, even the lattice structure itself presents an obstacle (short-range barrier) to dislocation motion, and the nature and distribution of obstacles determines the flow stress in metals [67].



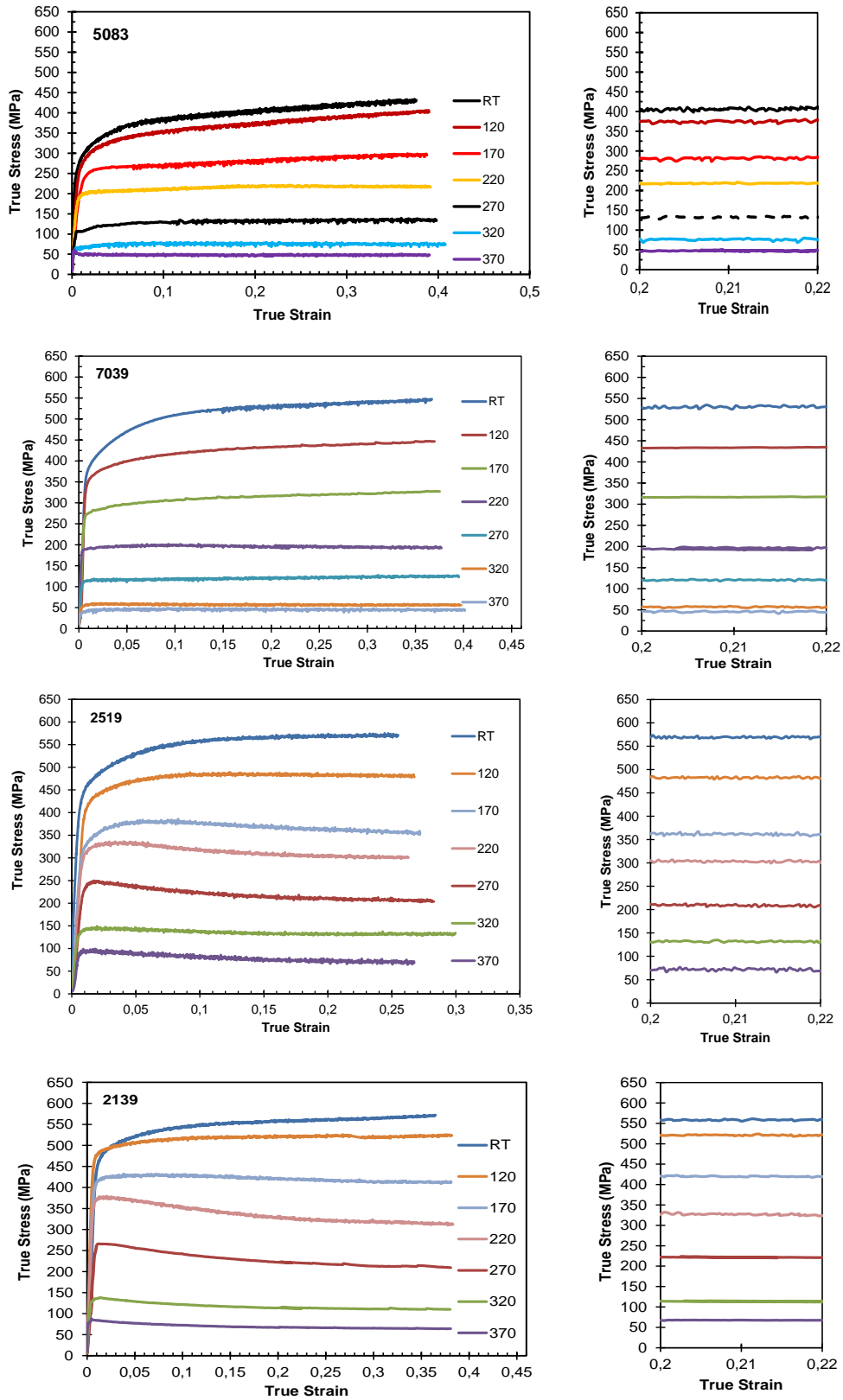


Figure 4.1 True stress-true strain curves at various temperatures at a reference strain rate of  $10^{-3} \text{ s}^{-1}$  for 5083, 7039, 2519 and 2139

The flow stress required to deform a metal ( $\sigma$ ) can be divided into two parts: (i) thermal stress component  $\sigma^*$ , which is dependent on the strain rate and temperature of the material, and (ii) athermal stress component  $\sigma_a$ , which is a function of microstructure. Thus,

$$\sigma = \sigma_a + \sigma^* \quad (4.1)$$

This can be expressed in functional form as;

$$\sigma = \sigma_a(G) + \sigma^*(T, \dot{\epsilon}) \quad (4.2)$$

It is known that the elastic properties ( $E$ ,  $G$  and  $\nu$ ) are slightly dependent on the temperature. The temperature causes the amplitude of vibration of the atoms to increase (but the frequency remains constant at approximately  $10^{13} \text{ s}^{-1}$ ). This increase in the amplitude separates the atoms somewhat and changes their equilibrium positions and interatomic forces, resulting in a decrease in elastic and shear moduli. This effect of temperature on elastic properties slightly affects the athermal component of stress, which is often considered to be a function of the shear modulus of material as implied in Equation 4.2. On the other hand, the real effect of temperature as well as strain rate on the flow stress of metals comes through the thermal stress component which is essentially governed by the thermally activated process of dislocation motion [67].

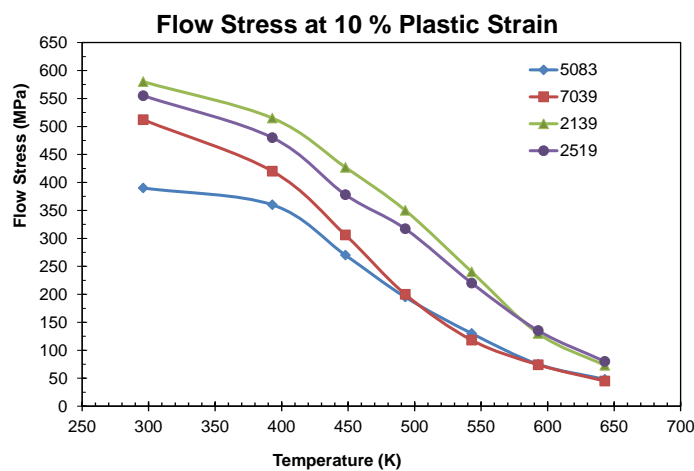


Figure 4.2 Flow stresses of 5083, 7039, 2519 and 2139 alloys as a function of temperature at 10% offset plastic strain at a strain rate of  $10^{-3} \text{ s}^{-1}$ .

At high enough temperatures, thermal stress component practically disappears as the thermal activation energy alone reaches the energy required to overcome short-range barriers, at which point the plastic deformation is essentially governed by (long-range) elastic interaction of gliding dislocations and driven by so-called athermal stress component. From this perspective, the experimental data shown in Figure 4.2 allow us to determine the athermal stress component for each alloy as the flow stress asymptotically approaches a plateau value at the high end of the temperature range investigated. The main concept of this process is also illustrated in Figure 4.3 [67].

Thermal softening rates, athermal flow stress components calculated from the Figure 4.2 are shown in Table 4.1. As it is seen in Table 4.1, thermal softening rate of 5083 is significantly lower than the other alloys up to 393 <sup>0</sup>K while 7039 has the highest one. Beyond this temperature, the thermal softening of 7039, 2519 and 2139 alloys almost have the same rate. Athermal component of flow stress for 5083 and 7039 is found to be  $\sigma_a \approx 40$  MPa while it is significantly higher for 2519 and 2139 at  $\sigma_a \approx 70$  MPa.

Table 4.1 Thermal softening rates, thermal and athermal flow stresses

Material	Thermal softening rate (MPa/K)		Athermal flow stress (MPa)
	298-393 K	448-643 K	
5083	-0.3	-1.4	40
7039	-0.94	-1.8	40
2519	-0.77	-1.7	70
2139	-0.67	-1.9	70

Results of Figure 4.2 also suggests that at low temperatures between 298-393 <sup>0</sup>K plastic deformation is driven by thermally activated dislocation glide, corresponding to a mild thermal softening rate. However, at higher temperatures beyond 448 <sup>0</sup>K we observe that thermal softening rate is almost doubled. This indicates that dynamic recovery (DRV) and even dynamic crystallization (DRX) mechanisms increasingly contribute to thermal softening at higher temperatures by decreasing the dislocation

density. Recalling that the dislocation forests are the main obstacles to the motion of dislocations in FCC metals and the temperatures involved in this range is about half the melting temperature of these aluminum alloys, DRV and DRX seem to be the most likely mechanisms responsible for increased thermal softening rate at higher temperatures.

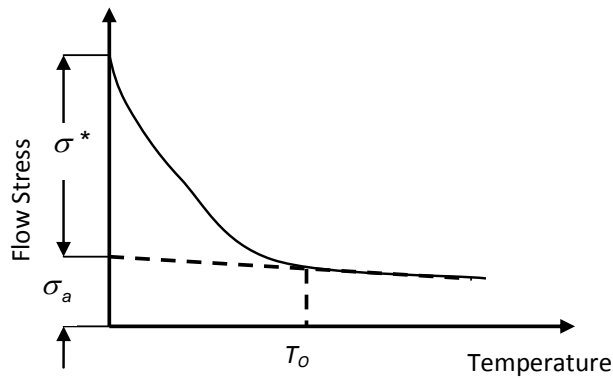


Figure 4.3 Flow stress of an idealized material as a function of temperature; thermal and athermal components of stress indicated [67].

#### 4.1.1.2. Strain Rate and Temperature Effect in Quasi-Static Regime

##### 4.1.1.2.1. Various Strain Rates of Quasi-static Regime at Room Temperature

Compressive stress-strain curves of aluminum alloys deformed at various quasi-static strain rates ( $10^{-3} \text{ s}^{-1}$ - $10^0 \text{ s}^{-1}$ ) at room temperature (RT) are shown in Figure 4.4.

Test results reveal that 5083 alloy has slight negative strain rate sensitivity (nSRS) while the other alloys have strain rate insensitivity in quasi-static regime. In closer inspection of all curves in Figure 4.4, mechanical response of 5083 also shows evidence of serrated flow. Serrated flow is one of the common results of Dynamic Strain Aging (DSA) in 5xxx series of aluminum alloys [68-72]. The DSA is a general term for the phenomenon where solute atoms diffuse around dislocations further strengthening the obstacles held on the dislocation and retard dislocation motion. Eventually these dislocations will overcome these obstacles with sufficient stress and will quickly move to the next obstacle where they are stopped and the process can repeat again.

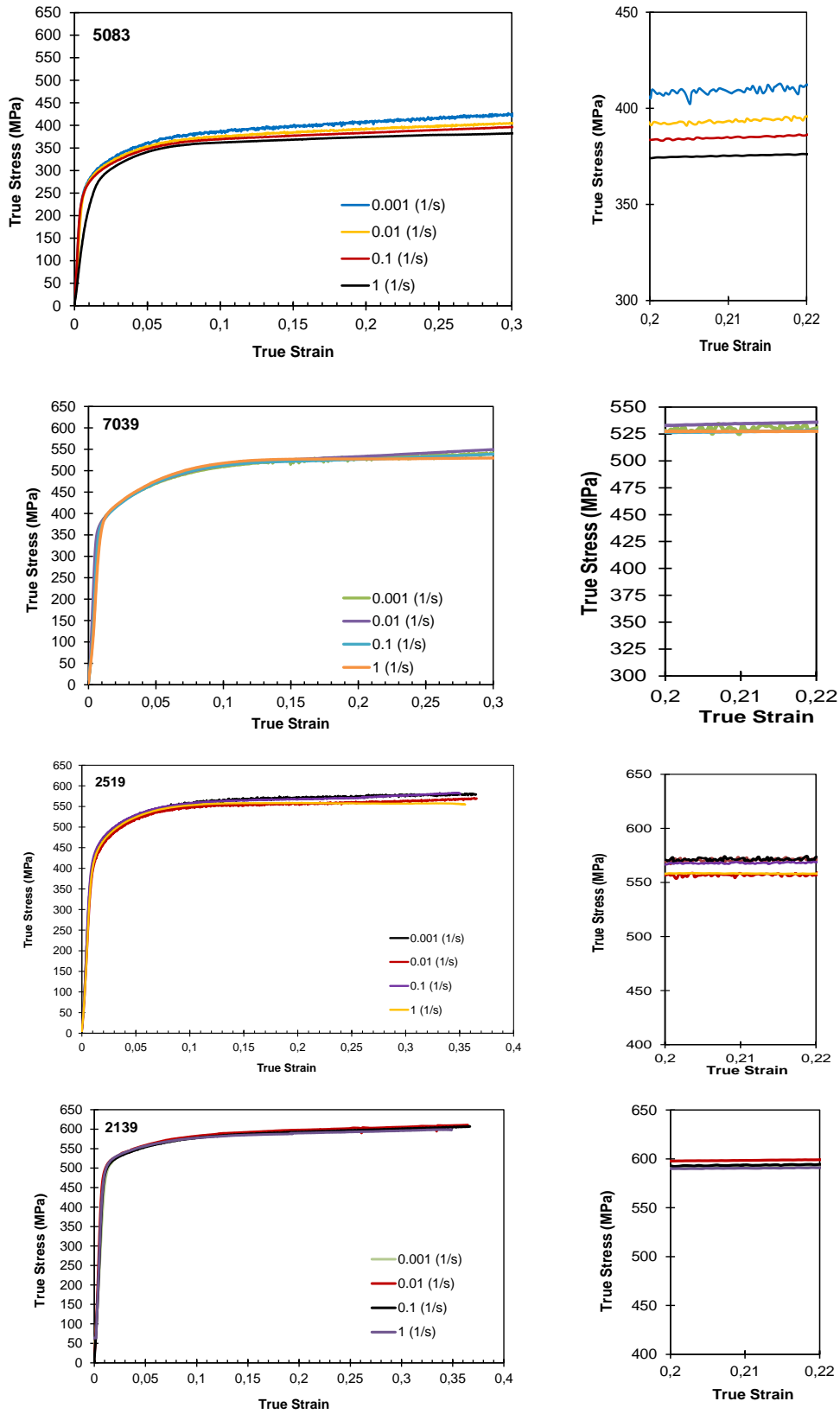


Figure 4.4 True stress-true strain curves of aluminum alloys at low strain rates ( $10^{-3}$ - $10^0$  s $^{-1}$ ) at RT (room temperature) for 5083, 7039, 2519 and 2139

This dynamic phenomenon is also referred to as the Portevin–Le Chatelier (PLC) effect with the appearance of serrated flow in stress-strain curves. The solute atoms causing serrated flow in 5083 alloy are Mg atoms. These are substitute atoms since they are larger than the aluminum atoms. Diffusion controlled nature of DSA also introduces a characteristic time scale to the process. At low strain rates, waiting time of dislocations at obstacles is long enough to allow this diffusive strengthening mechanism to operate. However, as the strain rate is increased solute atoms cannot diffuse fast enough to compete with the waiting time of dislocations at obstacles and, therefore, cannot provide the strengthening as much as they do at lower strain rates. In conclusion, DSA effectively leads to negative strain rate sensitivity (nSRS) in the material as observed in the case of 5083 from Figure 4.4.

Figures 4.4(b-d) clearly show that both yield and flow stresses of 7039, 2519 and 2139 alloys at room temperature are almost the same in entire range of quasi-static strain rates ( $10^{-3}$ - $10^0$  s<sup>-1</sup>) as expected for most of the aluminum alloys that are insensitive to strain rate. Additionally, in closer inspection of these figures, 7039, 2519 and 2139 alloys show no evidence of serrated flow at RT.

On the other hand, 2139 exhibits the highest strength. Strain hardening rate corresponding to each alloy is not affected by strain rate and is almost kept constant at quasi-static regime and at RT.

#### **4.1.1.2.2. Various Strain Rates of Quasi-static Regime at Elevated Temperatures**

How the temperature affects the strain rate sensitivity of aluminum alloys is investigated via controlled experiments as explained in Chapter 3. A specific temperature of 220 °C was selected to evaluate temperature effects above  $0.5T_m$  since it is observed that the thermal softening mostly occurs above  $0.5T_m$  as it can be seen in Figure 4.2.

The strain rate effects at elevated temperatures in the quasi-static regime (low strain rate regime) are shown in Figure 4.5. Although none of the aluminum alloys showed any strain rate hardening at room temperature, the flow stress increases with

increasing strain rate at the elevated temperature of 220 °C, showing a positive strain rate sensitivity (SRS).

As the temperature is increased, flow stress required to overcome short-range barriers gradually decreases because of the increase in thermal activation energy. What this means is that the plastic flow process is increasingly governed by thermal activated mechanisms in which both the temperature and the strain rate are two important players.

Therefore, strain rate hardening is observed at this elevated temperature even though it does not exist at room temperature.

As a result, elevated temperature causes SRS to increase rapidly. On the other hand, elevated temperature also affects strain hardening of the alloys such that 2519 and 2139 show strain softening at lower strain rate of quasi-static regime while 5083 and 7039 have no strain softening at quasi-static regime at elevated temperatures. Additionally, it is concluded that strain hardening increases with strain rate.

In closer inspection of Figure 4.5, 7039, 2519 and 2139 alloys show some evidence of serrated flow at elevated temperatures and at lower strain rates ( $10^{-3} \text{ s}^{-1} - 10^{-2} \text{ s}^{-1}$ ) of quasi-static regime. But the amplitudes of these discontinuities that are the manifestations of serrated flow are smaller and not as significant as in 5083 alloy. Naka et al. and Picu et al. [69-70] stated that this phenomena appears only in particular range of temperature and strain rate and the dislocation motion occurs so rapidly at higher strain rates that they cannot be delayed by solute atoms. That is why the serrated flow phenomenon cannot does not take place at higher strain rates ( $10^{-1} \text{ s}^{-1} - 10^0 \text{ s}^{-1}$ ) of quasi-static regime neither at RT nor at 220 °C as can be seen in Figures 4.4 and 4.5, respectively.

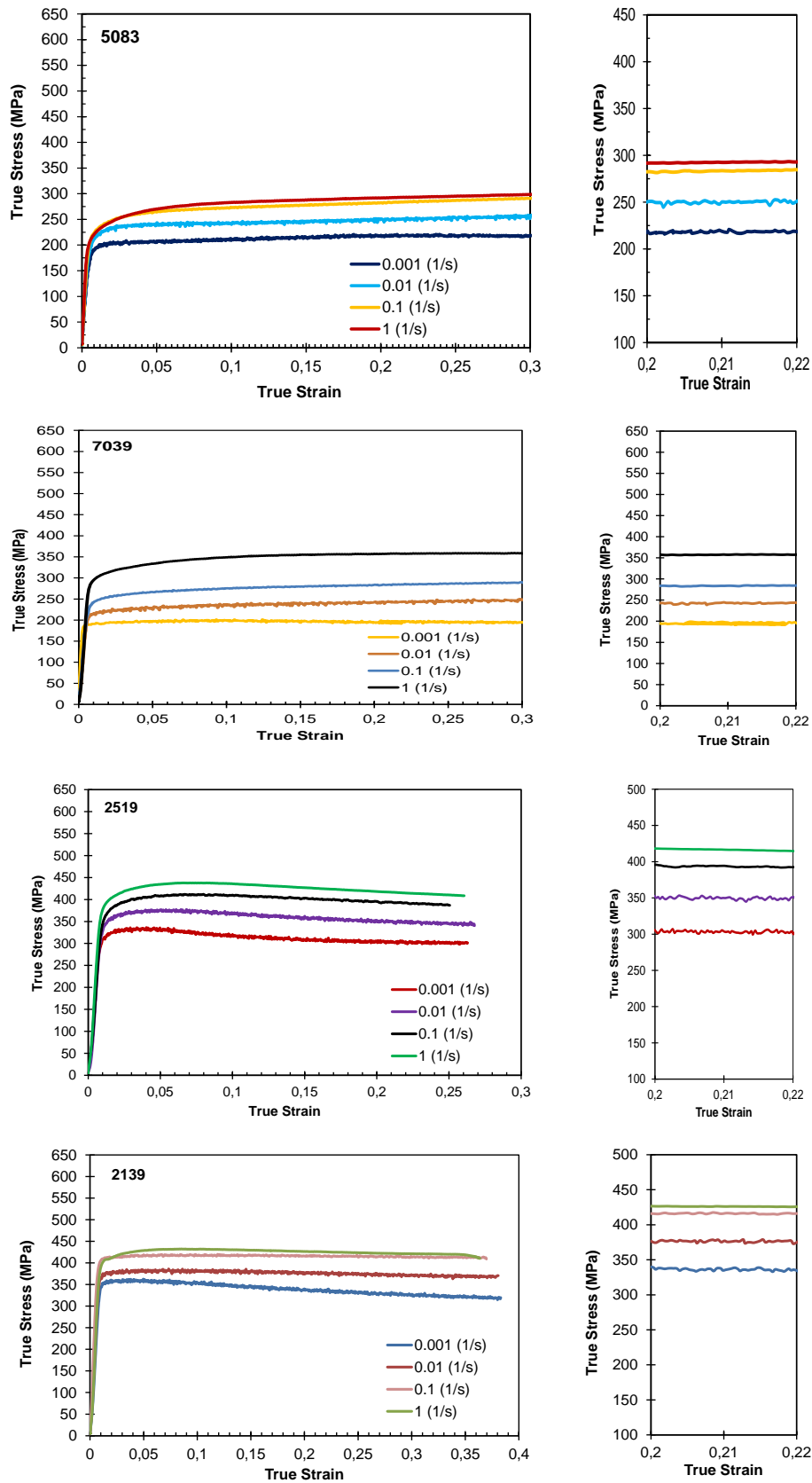


Figure 4.5 True stress-strain curves for aluminum alloys at low strain rates ( $10^{-3}$ - $10^0$  s $^{-1}$ ) and at elevated temperature (220 °C)



### 4.1.2. Dynamic (High Strain Rate) Experiments

For most materials, increasing the strain rate causes an increase in flow stress. The amount of strain rate sensitivity (SRS) depends on the temperature and material. In most metallic materials, the SRS at room temperature (RT) is small while at elevated temperatures the effect of strain rate on flow stress is much greater [73]. On the other hand, an increase in strain rate shifts the onset of strain hardening to lower strains.

To generalize the strain hardening behavior of materials, Figure 4.6 shows a schematic representation of the characteristic strain hardening behavior of FCC materials. High-purity FCC metals in an annealed condition, such as Cu, Ni, Al and Ag exhibit nearly strain-rate-independent yielding behavior, whereas strain hardening is strongly rate dependent after yielding, as shown in Figure 4.6. The strong dependency of strain hardening in FCC metals on temperature and strain rate is due to the suppression of dynamic recovery (DRV) processes [74].

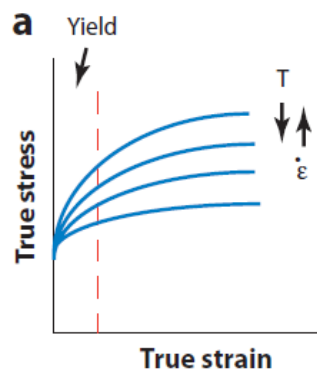


Figure 4.6 The influence of temperature and strain rate on the yield and strain hardening of pure FCC materials such as Ni, Al, and Cu [74].

#### 4.1.2.1 Strain Rate and Temperature Effect at Dynamic Regime

##### 4.1.2.1.1 High Strain Rate Behavior at RT

A number of high strain rate experiments were performed by using SHPB setup at room temperature. Resulting stress-strain curves for aluminum armor alloys are shown in Figure 4.7. One of stress-strain curves obtained in quasi-static regime (at

$10^{-3} \text{ s}^{-1}$  strain rate) is also added to these plots to make a direct comparison between the two regimes. All of the materials exhibited almost the same trend in their strain rate sensitivity such that there was very mild strain rate sensitivity in the range of strain rates from  $10^{-3}$  to  $10^4 \text{ s}^{-1}$  while the strain rate hardening significantly increased above  $10^4 \text{ s}^{-1}$ . For instance, as can be seen in Table 4.2, when the strain rate is increased 7 orders of magnitude from  $10^{-3}$  to  $10^4 \text{ s}^{-1}$ , the increase in flow stress is observed to be only about 10-40 MPa. On the other hand, less than an order of magnitude increase in strain rate beyond  $10^4 \text{ s}^{-1}$  results in a rapid increase in flow stress as much as 90-120 MPa. In other words, while all alloys exhibit mild strain rate sensitivity up to  $10^4 \text{ s}^{-1}$ , they display a dramatic increase in SRS above  $10^4 \text{ s}^{-1}$ . This behavior arises from the fact that the deformation mechanism at lower strain rates is dominated by thermally activated dislocation motion while it is governed by dislocation drag mechanism at higher strain rates. Such sudden increases in strain rate sensitivity of flow stress have been observed in a number of materials [75].

Table 4.2 The flow stress at various strain rate and 10% offset strain

Alloys	The flow stress (MPa) at $10^{-3} \text{ s}^{-1}$	The flow stress (MPa) at $9 \times 10^3 \text{ s}^{-1}$	The flow stress (MPa) at $3 \times 10^4 \text{ s}^{-1}$
5083	390	430	550
7039	512	555	660
2519	560	590	685
2139	580	590	680

At higher strain rates above the transition rate of  $10^4 \text{ s}^{-1}$ , the strain hardening is observed until the strain reaches a critical value which is called instability strain, beyond which deformation ceases to be uniform and macroscopic stress-strain behavior is governed by the formation and propagation of highly localized deformation bands called adiabatic shear bands (ASBs). Once the deformation instability starts, the flow stress starts to decrease dramatically due to the thermal softening that takes place as a result of local temperature increase within ASBs. These ASBs rapidly transform to shear cracks with further loading, leading to catastrophic failure.

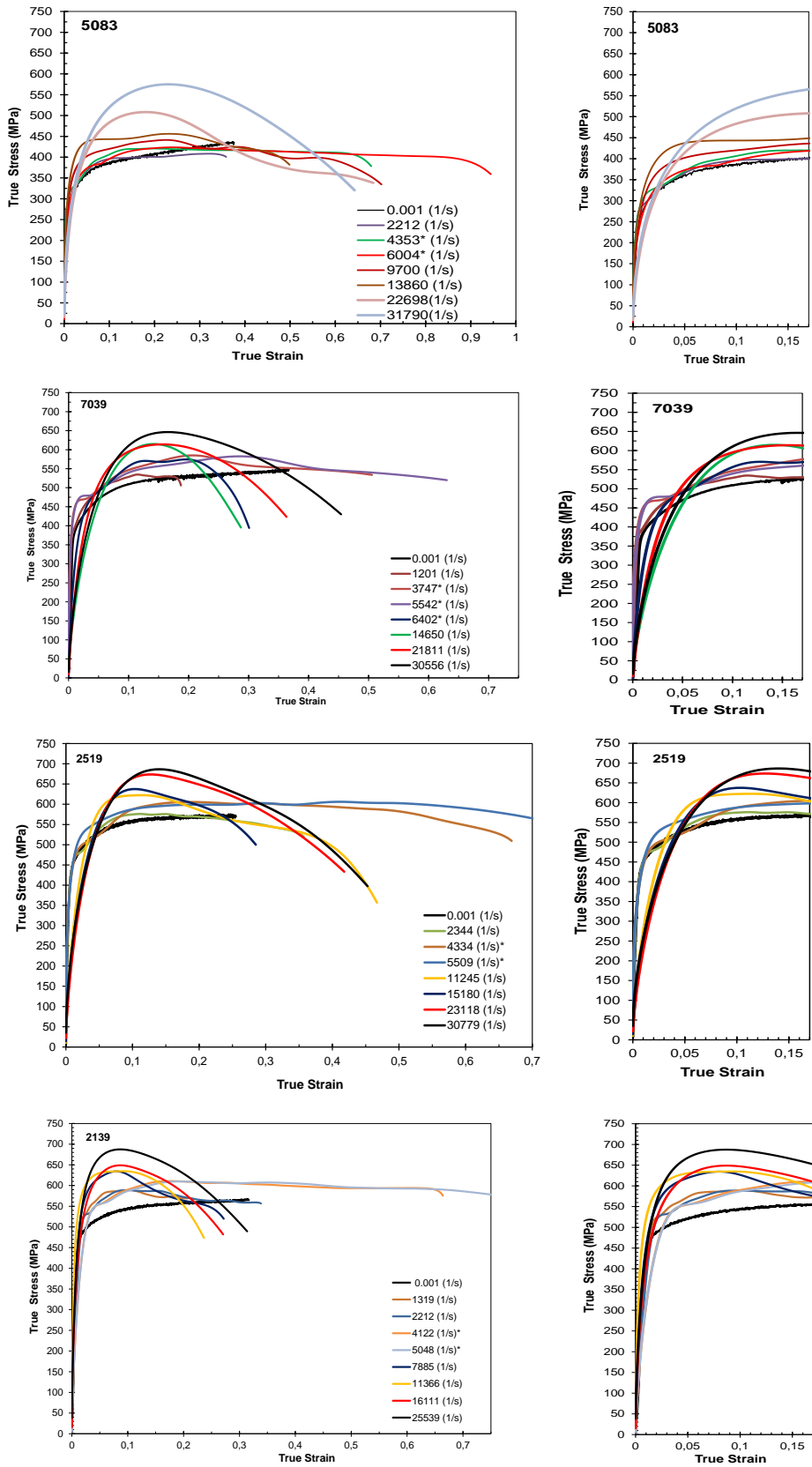


Figure 4.7 Dynamic compression true stress-true strain curves of 5083, 7039, 2519 and 2139 at strain rates of ( $10^2$ - $10^4$  s<sup>-1</sup>) at RT, full scale (left) and low strain (right)

#### 4.1.2.1.2 High Strain Rate Behavior at Elevated Temperature

Dynamic behavior of aluminum alloys; 5083, 7039, 2519 and 2139 at 220 °C is illustrated in Figure 4.8 over a range of strain rates from  $10^2$  to  $10^4$  s<sup>-1</sup>. As before, one of the stress-strain curves obtained at 220 °C in quasi-static regime at the strain rate of  $10^{-3}$  s<sup>-1</sup> is also added to the plots in Figure 4.8 to facilitate direct comparison between the two regimes.

Test results establish a strong coupling of temperature and strain rate effects on the flow stress. The magnitude of the flow stress in stress-strain curves drops when the temperature increases. All alloys exhibit the same dramatic decrease in flow stress at elevated temperatures as expected from the thermal softening behavior. Similar to the room temperature results, two different SRS is observed in quasi-static and dynamic regimes. However this time, at elevated temperature (220 °C), SRS observed in the range of strain rates from  $10^{-3}$  to  $10^4$  s<sup>-1</sup> was not only much higher than the one observed at room temperature but also comparable to the SRS at strain rates beyond  $10^4$  s<sup>-1</sup>.

Strain hardening behaviors of the alloys are also different at elevated temperature. The strain hardening is clearly lower at low strain rates than at higher strain rates especially above  $10^4$  s<sup>-1</sup>. The strain rate sensitivity (SRS) of the alloys is also relatively higher at elevated temperatures. At higher strain rates above  $10^4$  s<sup>-1</sup>, the strain hardening is observed until the strain reaches a critical value which is called instability strain. Beyond this point, further loading leads to the onset of ASBs and associated thermal softening behavior in macroscopic behavior similar to the process discussed in room temperature results.

Dynamic behavior of aluminum alloys at elevated temperatures reveal that all alloys exhibit almost the same behavior with different SRS and strain hardening due to the different strain rate hardening mechanisms. For instance, as can be seen in Table 4.3, the increase in flow stress is about 100 and 195 MPa between  $10^{-3}$  s<sup>-1</sup> and  $8 \times 10^3$  s<sup>-1</sup> strain rates, while the increase in flow stress is about 70 and 90 MPa above  $8 \times 10^3$  s<sup>-1</sup> strain rates.

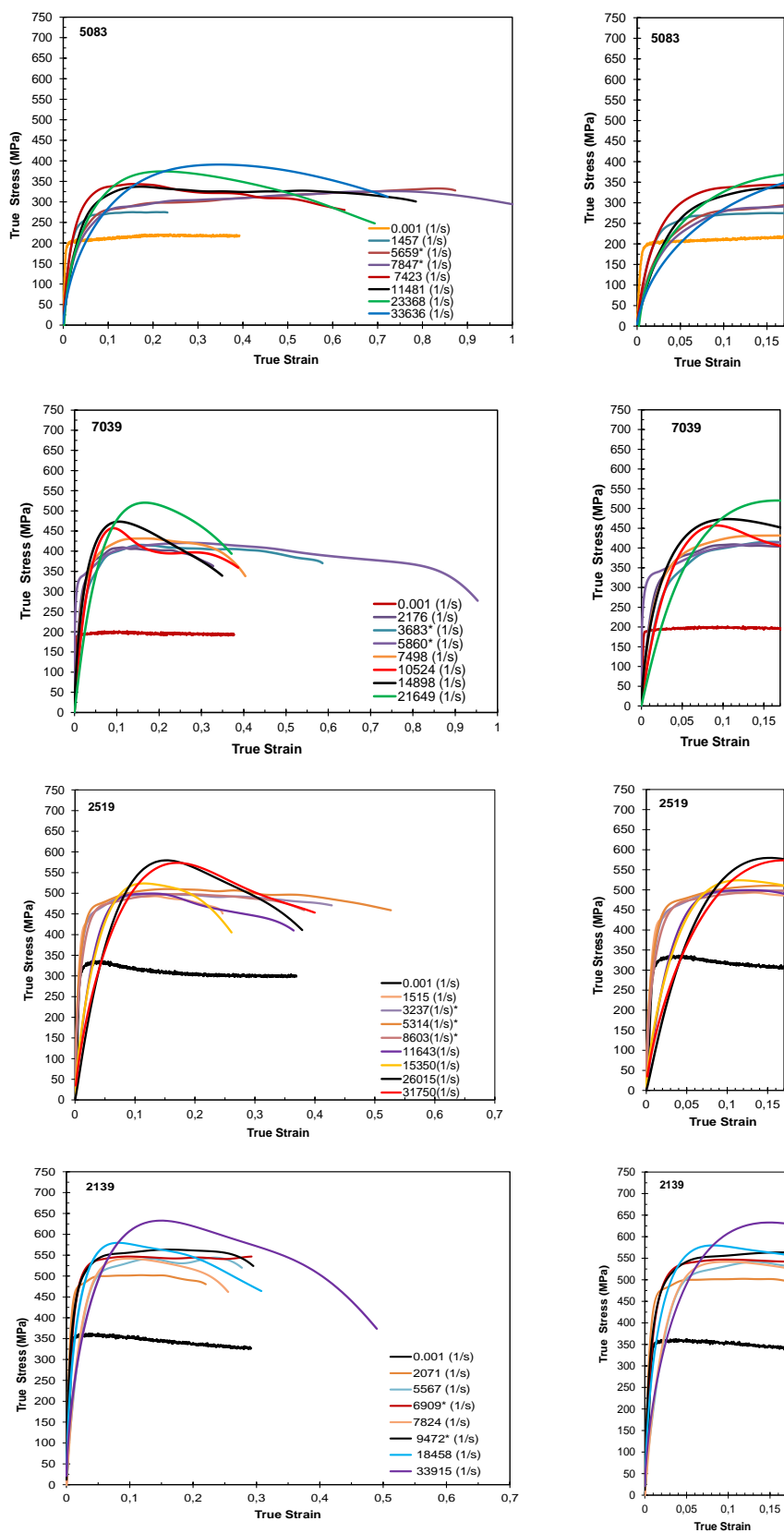


Figure 4.8 Dynamic stress-strain curves for 5083, 7039, 2519 and 2139 for strain rates ( $10^2$ - $10^4$   $s^{-1}$ ) at a temperature of 220  $^{\circ}C$ , full scale (left) and low strain (right)

At elevated temperatures, the flow stress increase at strain rates above  $10^4 \text{ s}^{-1}$  is not as high as that of below  $10^4 \text{ s}^{-1}$ . This is attributed to increasing role of thermally activated mechanisms in plastic deformation at high temperatures as discussed in detail in Section 4.1.2.

Table 4.3 Compression dynamic flow stress at  $220^\circ\text{C}$  and 10% offset strain

Alloys	The flow stress (MPa) at $10^{-3} \text{ s}^{-1}$	The flow stress (MPa) around $8 \times 10^3 \text{ s}^{-1}$	The flow stress (MPa) at $3 \times 10^4 \text{ s}^{-1}$
5083	212	314	380
7039	200	432	520
2519	317	495	575
2139	350	545	625

Generally the rate of strain hardening also decreases at elevated temperature as shown in Figure 4.8 when compared to Figure 4.7.

#### 4.1.2.2 Rate Dependence of Flow Stress in Quasi-static and Dynamic Strain Regimes

In order to observe the strain rate sensitivity (SRS) of aluminum alloys, in a wide range of strain rates, the flow stresses at 10% offset strain have been plotted as a function of strain rate on logarithmic scale at RT and  $220^\circ\text{C}$  as shown in Figure 4.9.

It is obvious from Figure 4.9 that the strain rate sensitivity becomes more pronounced at elevated temperature as compared to RT. Moreover, rate dependence of flow stress is significantly higher in dynamic loading regime than in quasi-static regime.

At room temperature and quasi-static regime, the alloys, 7039, 2519 and 2139 exhibit almost no SRS while 5083 shows negative SRS because of the Dynamic Strain Aging (DSA) as discussed in Section 4.1.1.2.1. The flow stress of 5083 alloy decreases with increasing strain rate at quasi-static regime ( $10^{-4}$ – $10^0 \text{ s}^{-1}$ ) while it steadily increases with strain rate in dynamic regime. Thus, the strain rate sensitivity of 5083 is negative in quasi-static regime while it is positive in dynamic regime. The

negative strain rate sensitivity appears to be similar to that presented by Huskins *et al.*[76] for the same material. Interestingly, however, the negative strain rate sensitivity observed in 5083 disappears at elevated temperatures suggesting that thermally activated dislocation kinetics dominates the mechanical response at higher temperatures. This reversal in SRS can be explained as follows. At room temperature, DSA is observed because the critical time scale for the diffusion of solute atoms to dislocation cores is on the same order of magnitude with the time scale of deformation in quasi-static loading regime. On the other hand, when the temperature is increased, diffusion rate significantly increases and results in a marked decrease in diffusion time scale as compared to the typical time scale of deformation at low strain rates. In other words, diffusion based strengthening of energy barriers at elevated temperatures occurs so fast that the thermally activated dislocation kinetics remains as the sole rate-controlling mechanism in quasi-static regime. In fact, when the strain rate approaches to the higher limit of quasi-static regime, deformation time scale becomes small enough to interfere with diffusion controlled hardening process (where dislocations start overcoming barriers at a faster rate before diffusion hardening fully occurs) such that the effective SRS relatively decreases as can be observed from Figure 4.9.

Another important observation from the experimental data presented in these graphs, is that the flow stress increases mildly with strain rate above  $10^3 \text{ s}^{-1}$ . This causes moderate SRS at low strain rate regime. But after the strain rate exceeds  $10^4 \text{ s}^{-1}$ , the SRS increases to a comparatively higher value due to the change in rate controlling mechanism from thermally activated dislocation mechanism to dislocation drag mechanism as discussed in Sections 4.1.2.1.1 and 4.1.2.1.2. Furthermore, it is interesting to note that strain rate sensitivity seems to be almost the same in dynamic loading regime irrespective of deformation temperature, although the flow stresses are significantly lower at elevated temperature. This behavior is in line with the underlying dislocation drag mechanism operating in this regime where the rate of hardening is proportional to the rate of deformation as discussed in Section 2.1.2.

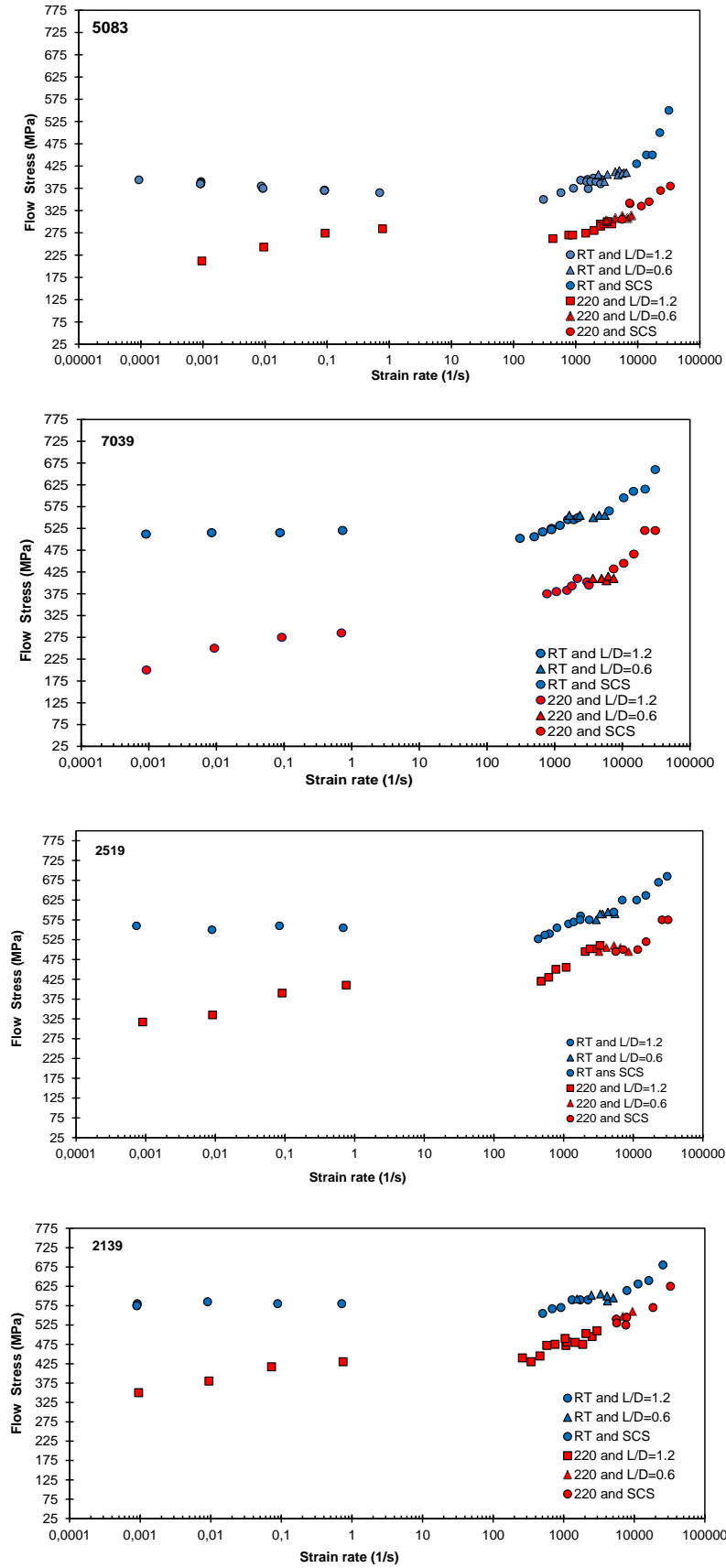


Figure 4.9 Variation of flow stress 10% offset strain with strain rate at both RT and 220 °C for 5083, 7039, 2519 and 2139



## **4.2 Propensity to Adiabatic Shear Localization**

### **4.2.1 Occurrence of adiabatic shear band (ASB)**

Adiabatic shear banding (ASB) is an important deformation instability that is commonly observed in dynamic deformation processes in which materials are subjected to large strains at high strain rates. Examples of these processes are armor penetration, blanking, cropping, impact erosion and frictional contact, dynamic forming and high speed cutting. Metals, such as armor materials, that are mostly subjected to impact by projectiles are potentially susceptible to the formation and propagation of adiabatic shear bands leading to catastrophic fracture.

Investigation of the conditions that lead to adiabatic shear banding requires well controlled experiments and special specimen geometries where uniform, yet large, strains are ensured in the gage section of specimen under a predominantly shear mode of deformation. A high, but steady, strain rate is also required to achieve adiabatic conditions by limiting conductive heat loss from deformation zone to negligible proportions. Strain rates typically achieved by SHPB experiments ( $10^3$ - $10^4$  s<sup>-1</sup>) meet these conditions when used in conjunction with well calibrated shear compression specimens (SCSs).

Therefore, Split Hopkinson Pressure Bar (SHPB) is the most commonly used technique in studying adiabatic shear bands. There are different types of SHPB experiments, with their advantages and disadvantages, which are used to determine the propensity of materials to failure by adiabatic shear localization.

The most widely used ones are (i) torsional SHPB technique with hollow torsion specimens, and (ii) compression SHPB technique with either hat-shaped specimen or shear compression specimen (SCS). However, torsion specimens may suffer from buckling and bending problems during deformation and also torsional SHPB is limited to relatively low strain rates while, on the other hand, hat-shaped specimen lacks a well-defined gage section with uniform deformation field. Due to these shortcomings, SCS was developed to obtain higher strain rates and almost uniform strain field in the gage section. But SCS needs additional experiments to determine

certain calibration parameters such as  $k_1$  and  $k_2$  since it is geometry depended (for a review, Bai and Dodd[29]).

#### 4.2.2 Parameter Fitting for SCS Dynamic Experiments

SCS has a unique geometry with a pair of slots machined on the opposite faces of a circular specimen as shown in Figure 3.1. In SHPB experiments, time resolved load and displacement rate is calculated by using incident, reflected and transmitted stress wave signals recorded by an oscilloscope. In order to convert these load and displacement data to scalar measures of equivalent stress and plastic strain, the following equation (Equation 4.3) was developed by Vural et al [47].

$$\begin{aligned}\varepsilon_{eq} &= \frac{1}{k_1} \frac{\delta}{h} \\ \sigma_{eq} &= k_1 \exp(-k_2 \varepsilon_{eq}) \frac{P}{Dt_o}\end{aligned}\tag{4.3}$$

where  $k_1$  and  $k_2$  are constants determined from either computational analysis or through calibration experiments conducted with classical cylindrical specimens.  $\sigma_{eq}$  is the equivalent (von Mises) stress and  $\varepsilon_{eq}$  is the equivalent strain,  $P$  is the compressive force,  $D$ ,  $t_o$ ,  $h$  and  $\delta$  are the SCS dimensions shown in Figure 3.1.

In order to determine calibration constants  $k_1$  and  $k_2$  in Equation 4.3, stress-strain curve of SCS should be matched with the stress-strain curve of cylindrical specimen with a suitable  $k_1$  and  $k_2$  parameters.

Therefore, both cylindrical and SCSs were tested at a reference strain rate of  $10^{-3} \text{ s}^{-1}$  at room temperature. True stress- plastic strain data of both tests were overlapped with appropriate fitting parameters  $k_1$  and  $k_2$  separately for each alloy; 5083, 7039, 2519 and 2139 as shown in Figures 4.10.

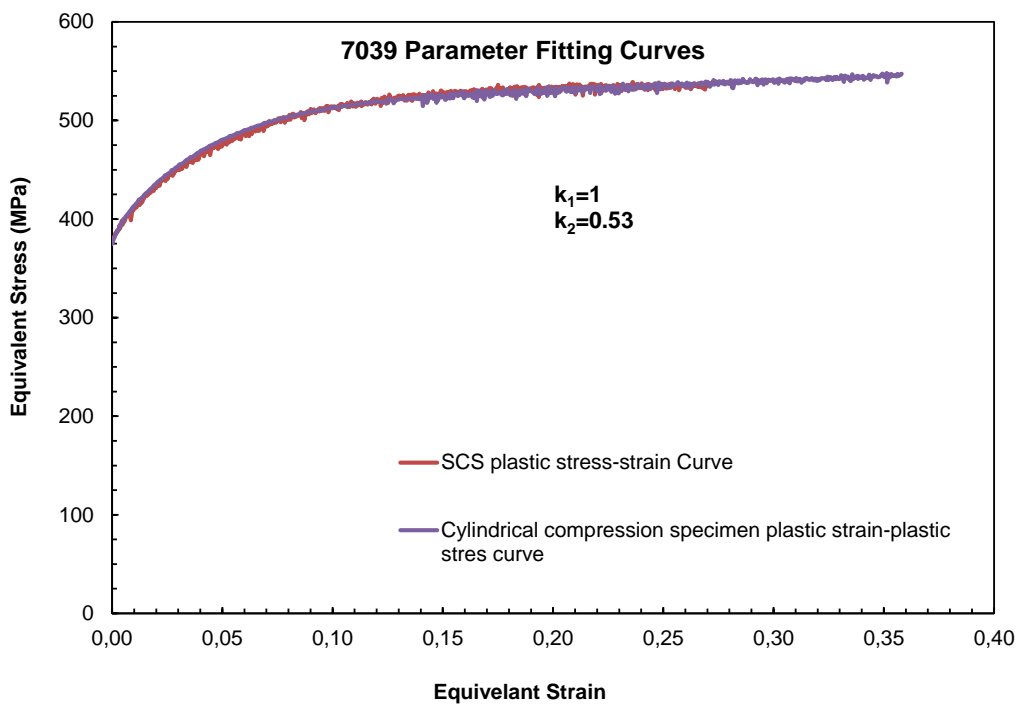
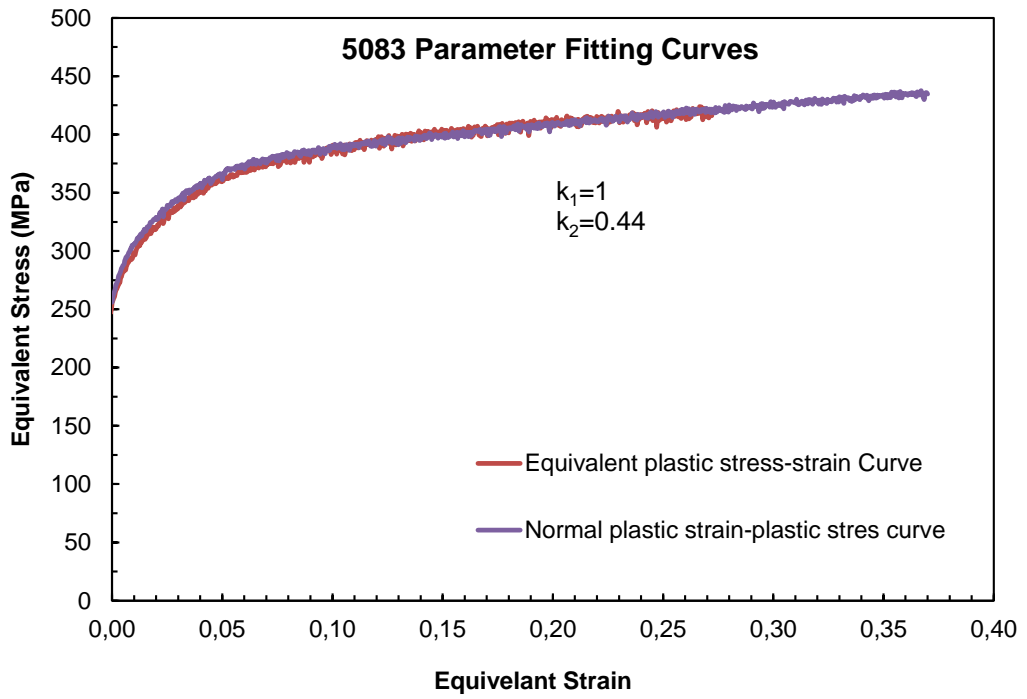


Figure 4.10 Calibration experiments to determine fitting parameters for 5083, 7039, 2519 and 2139

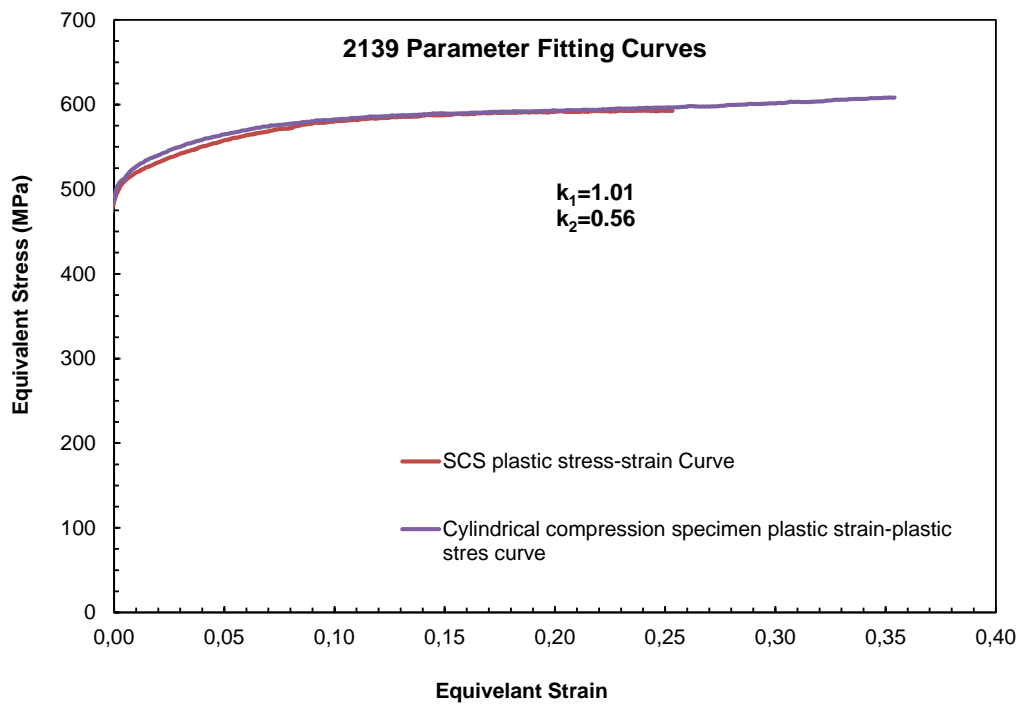
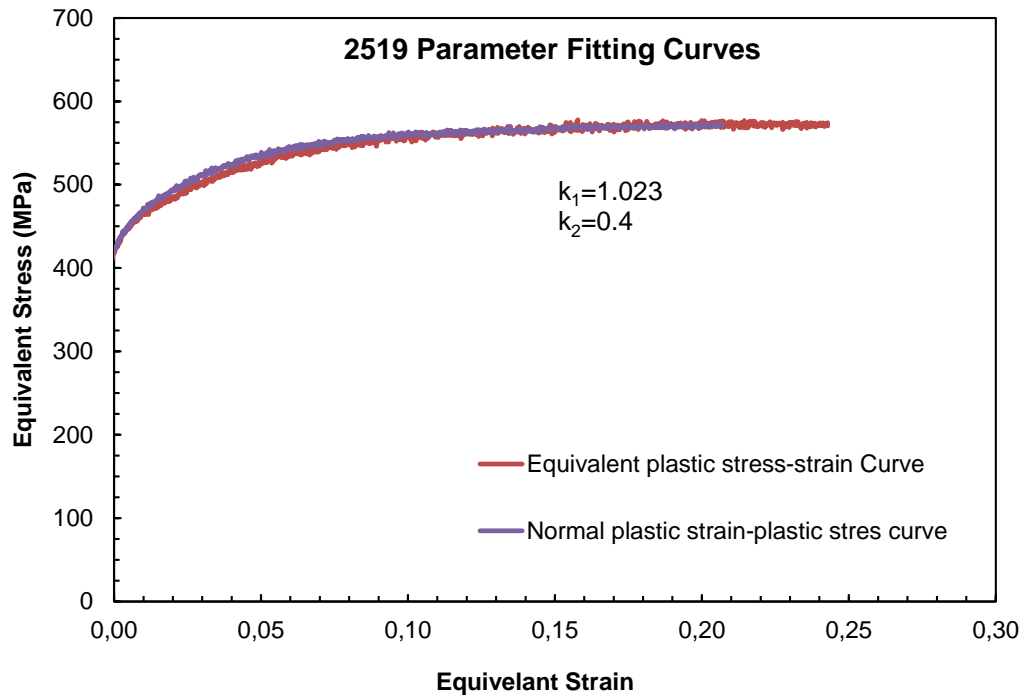


Figure 4.10 Continued

## 4.2.3 SCS Dynamic Experiments

### 4.2.3.1. Shear Localization Curves

Equivalent stress-strain curves obtained from dynamically loaded SCSs indicate the deformation in the gage section of specimens undergoes three distinct stages as can be seen in Figure 4.11. The stage 1 is characterized with work hardening and homogenous deformation. As the strain increases, stage 2 occurs with onset of adiabatic shear band (ASB) formation at  $\epsilon_1$ . Dynamic deformation is inhomogeneous in stage 2 and characterized with the formation and propagation of one or more localized shear bands. After ASB formation and development in stage 2, when the macroscopic strain reaches to  $\epsilon_2$  (also called as critical strain  $\epsilon_{cr}$ ), stage 3 starts, when the transition of ASBs to shear cracks and eventual failure [29].

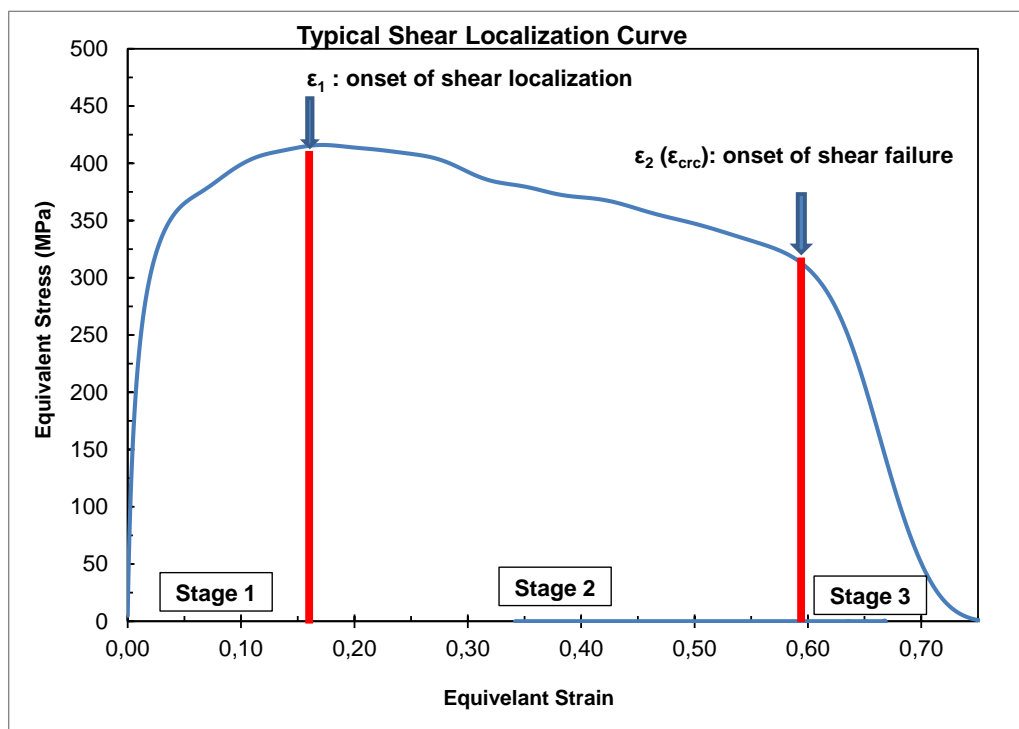


Figure 4.11 A Typical shear localization curve showing the three stages of shear deformation

Dynamic tests with SCSs have been performed for 5083, 7039, 2519 and 2139 to determine the onset of shear localization and shear failure points. Then, several controlled tests were carried out by using stop rings to obtain SCSs deformed to predefined strains in the 1<sup>st</sup>, 2<sup>nd</sup> and 3<sup>rd</sup> stages of their localization curve. Using the

stop rings to freeze the deformation at the predetermined points allowed us to investigate the evaluation of the deformation substructure and shear localization. To this end, a minimum of three localization curves were obtained for each alloy to determine critical strain points separating these three stages (as much as close to the  $\epsilon_1$  and  $\epsilon_2$  strains, respectively) as well as to ensure the repeatability of the experimental data. These repeatability curves and average range of the stages were shown in Figure 4.12 for each alloy.

According to these curves, SCSs undergoes three distinct stages (1<sup>st</sup>, 2<sup>nd</sup> and 3<sup>rd</sup> stage) of the dynamic deformation as shown in Figure 4.12. These curves are of critical importance not only to determine the macroscopic strain points separating these different deformation regimes but also to extract some useful quantitative data that helps and guide us in the assessment of the shear localization behavior. Thus, the quantitative data such as critical strains, maximum flow stresses and corresponding strains, thermal softening rate in 2<sup>nd</sup> and 3<sup>rd</sup> stages were tabulated for each alloy in Table 4.4.

Table 4.4 Comparison of critical strains, stresses and softening rates obtained from SCS experiments of 5083, 7039, 2519 and 2139. Note that all specimens had the same gage width ( $w=0.1$  in) and were tested at the same strain rate ( $5 \times 10^3 \text{ s}^{-1}$ ) and temperature (RT).

<b>Material</b>	<b><math>\sigma_{\max}</math> (MPa)</b>	<b><math>\sigma_{\text{cr}}</math> (MPa)</b>	<b><math>\epsilon_1</math></b>	<b><math>\epsilon_{\text{cr}} (\epsilon_2)</math></b>	<b><math>\Delta\sigma/\Delta\epsilon</math> in 2<sup>nd</sup> stage (MPa)</b>	<b><math>\Delta\sigma/\Delta\epsilon</math> in 3<sup>rd</sup> stage (MPa)</b>
5083	417	317	0.18	0.60	238	2641
7039	525	490	0.11	0.32	166	2000
2519	602	505	0.09	0.38	334	6312
2139	570	510	0.09	0.35	240	4080

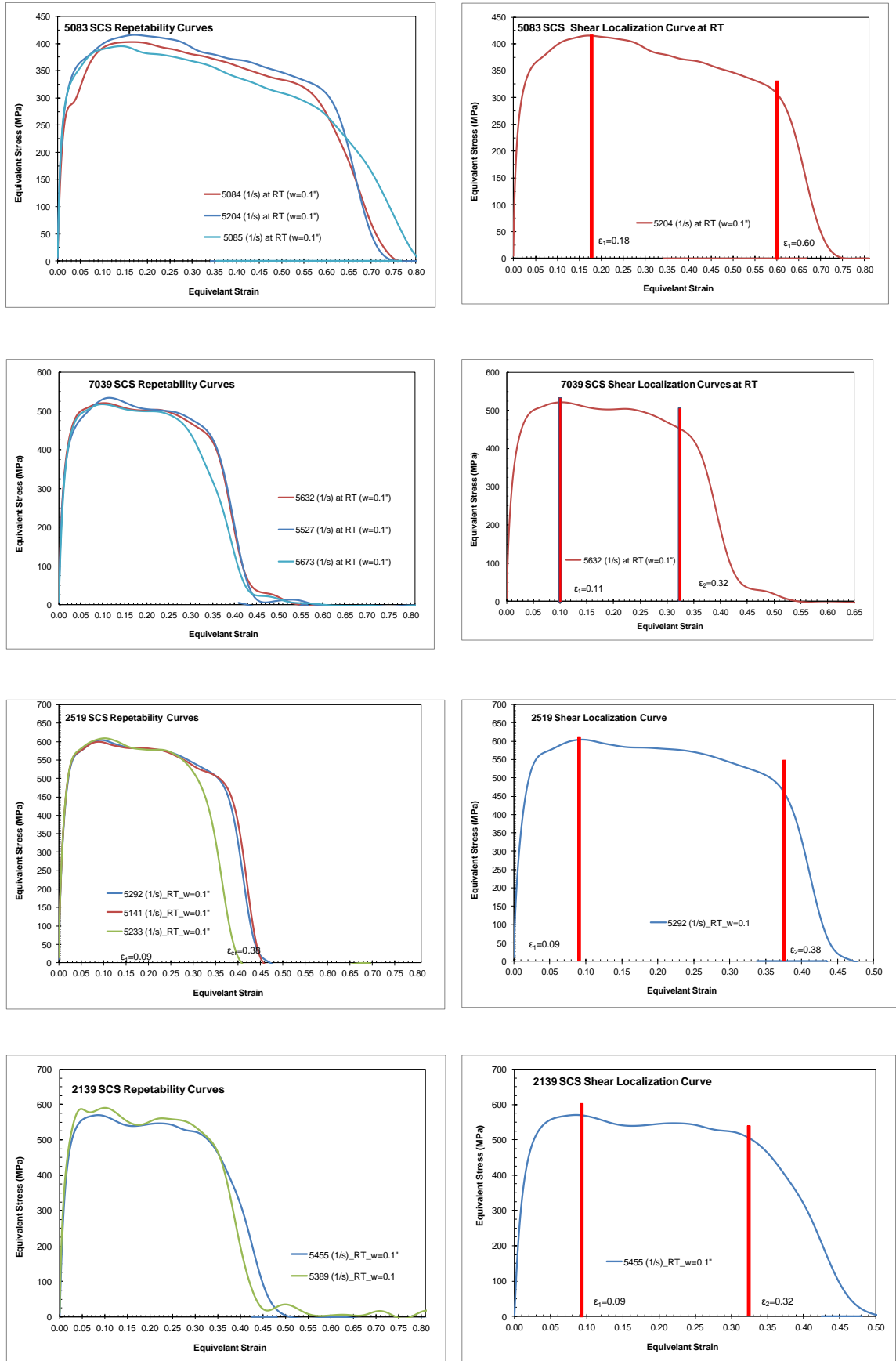


Figure 4.12 Shear localization curves of 5083, 7039, 2519 and 2139

### 4.2.3.2. Dynamic Experiments with Stop Rings

As also discussed in Section 4.2.3.1 a minimum of three stop rings were designed and manufactured for each alloy to dynamically deform SCSs to pre-determined strains that fall into 1<sup>st</sup>, 2<sup>nd</sup> and 3<sup>rd</sup> stages according to the shear localization curves given in Figure 4.12. Pre-determined strain values before and after the onset of shear localization strain ( $\epsilon_l$ ) and close to onset of shear failure ( $\epsilon_2$ ) are tabulated in Table 4.5 and shown in Figure 4.13 for each alloy.

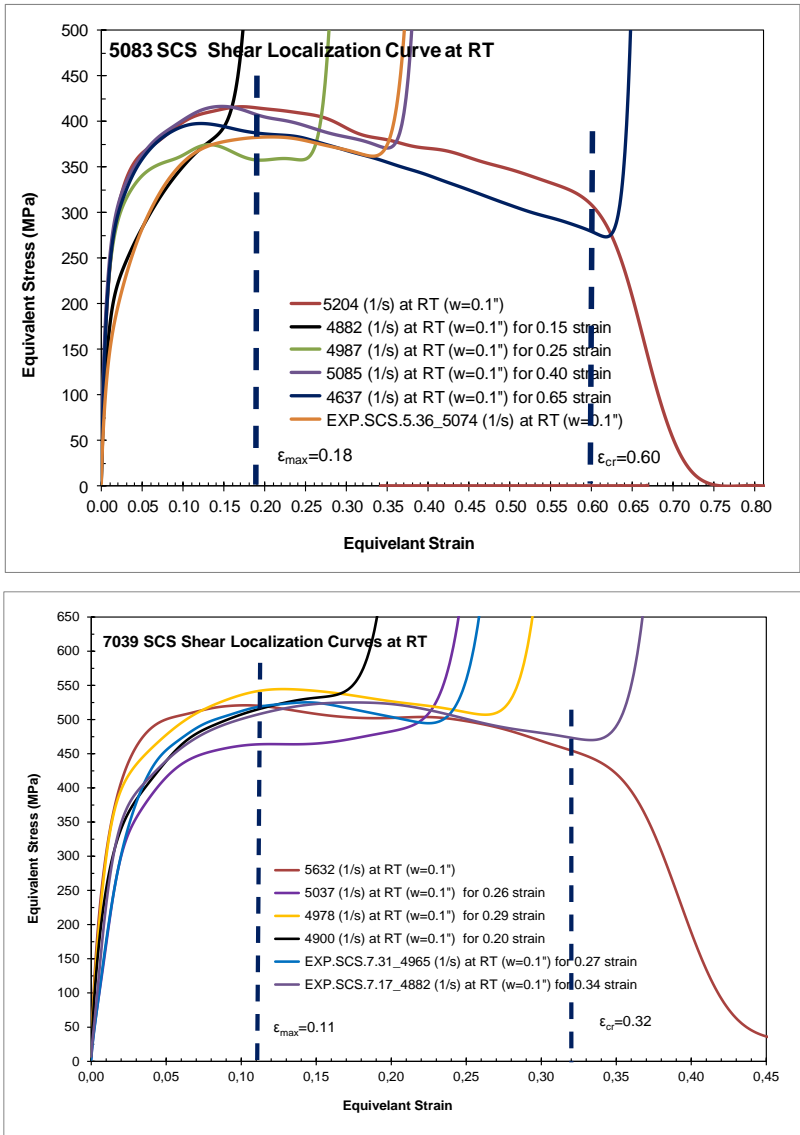


Figure 4.13 Dynamic experiment result with stop rings embedded on shear localization curves for 5083, 7039, 2519 and 2139



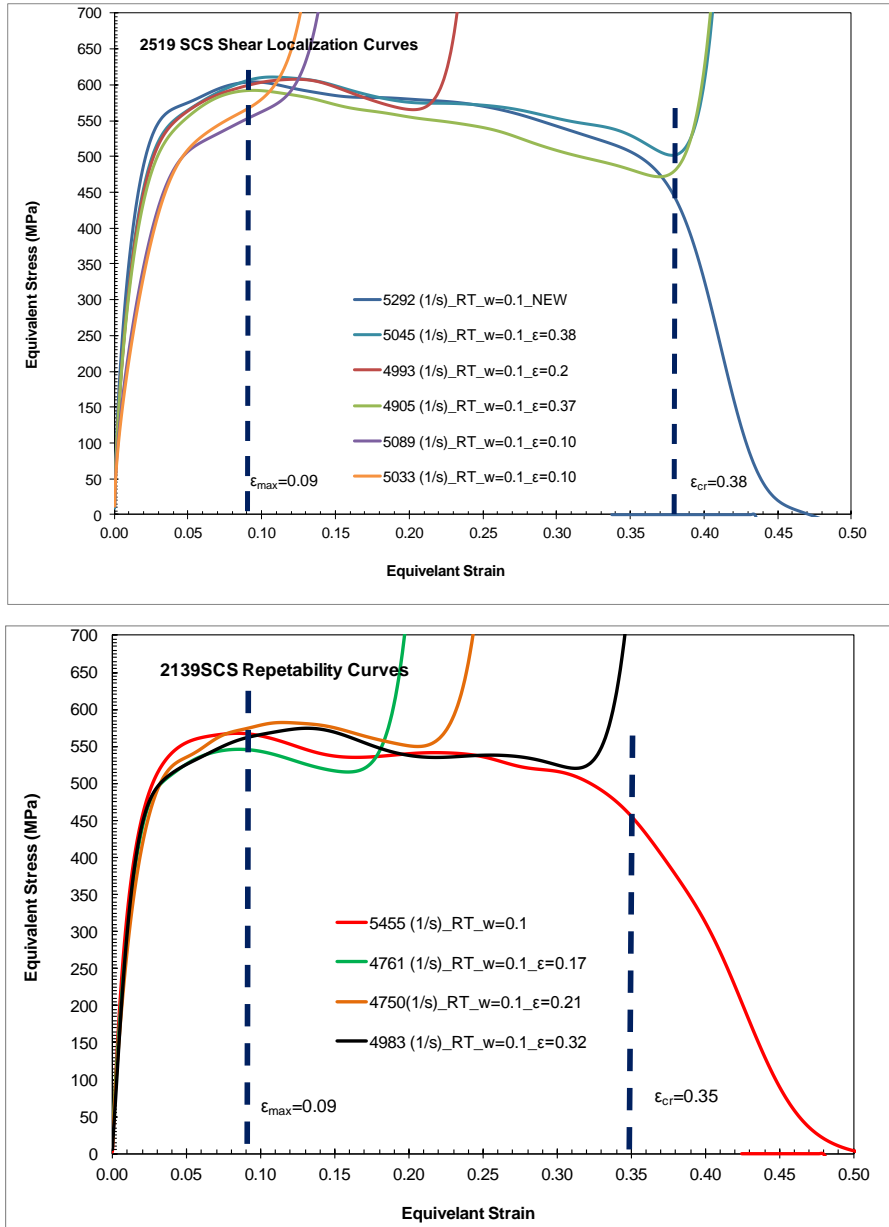


Figure 4.13 Continued

Table 4.5 Pre-determined strain values for SCSs for each alloy with respect to three distinct stages

Material	Before $\epsilon_1$	After $\epsilon_1$	Close to $\epsilon_2(\epsilon_{cr})$
5083	0.15	0.25 and 0.40	0.65
7039	0.18	0.22	0.29
2519	0.1	0.20	0.27
2139	0.17	0.21	0.32

### 4.3 Microstructural Observation

All SCSs dynamically deformed to pre-determined strains (given in Table 4.5 and graphically shown in Figure 4.13) were recovered, sectioned and prepared for microstructural examination by using Nikon Eclipse MA 200 inverted metallurgical microscope with NIS-Elements Imaging Software. After careful grinding, polishing and chemical etching, the gage sections of specimens were directly examined by optical microscope at a magnification of 5x to 50x depending on the resolution and clarity of the image. Firstly, a complete image of sectioned specimens was obtained by stitching the images together from multiple fields of view during shooting as shown in Figure 4.14(a). Then a detail section were taken from that complete image as seen in Figure 4.14(b) in order investigate the adiabatic shear localizations in the gage length for each pre-determined strain and alloy.

Two types of shear bands were observed by optical microscopy for all of aluminum alloys; 5083, 7039, 2519 and 2139. One is the deformed shear band spread out along almost entire gage section, and the other is severely localized shear band of much smaller length scale typically located at the borders of gage section and sometimes characterized with a white color, as shown in Figure 4.15. The white shear band is also called as “transformed shear band” [77].

The Figures 4.15-4.18 illustrate the deformation substructure in each one of alloys before and after the onset of shear localization. It is obvious from microstructural investigation that the deformation in stage 1 is homogeneous with no sign of shear localization. Beyond the maximum stress in stage 2, the signs of non-uniform shear are observed first in the form of large scale bends in otherwise uniform shear field represented by straight texture lines in microstructure. As the deformation continues further, towards the end of stage 2, localized shear bands of very small thickness starts developing at the sites of stress concentration (typically at the edges of gage section). Finally in stage 3, these highly localized shear bands show signs of dynamic recrystallization (DRX), which is also taken as an indication of significant local temperature rise, and appear as white lines after chemical etching, which indicates severely localized shear. Adiabatic shear band(s) rapidly propagates and evolves to shear cracks by the end of stage 3. For example, as the strain goes from

0.15-0.25 range to 0.45-0.65 range for 5083 alloy and from 0.20 to 0.38 for 2519 alloy, transformed shear bands (white shear bands) appears. As it can be seen in Figure 4.16, the phenomena are the same for 7039 alloy. However, for 2139 alloy there is no sign of highly localized shear bands although some degree of localization is observed at the end of stage 2 (see Figure 4.18). Thus it can be concluded that 2139 has the lowest propensity to adiabatic shear localization since the homogenous deformation continues throughout the 2<sup>nd</sup> stage and there is no apparent shear localization and no decrease in width of the deformed band. This lower propensity of 2139 to adiabatic shear localization is also considered to be one of the reasons for its higher ballistic performance shown in Figure 1.4. Dannemann et al. [15] also concluded in their small size research that 2xxx series alloys have superior ballistic performance than 5000 series alloys.

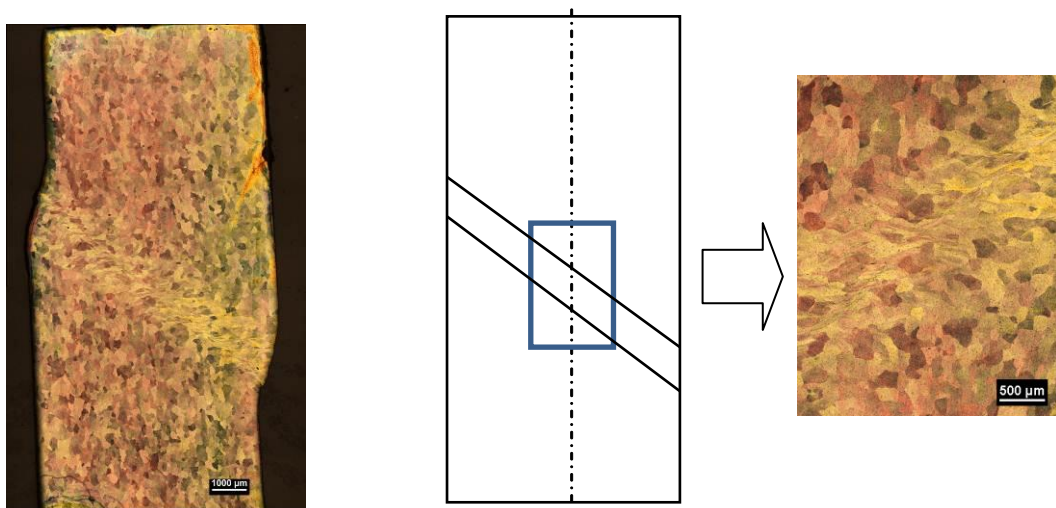


Figure 4.14 Microstructural image (a) a complete view (b) a detail section

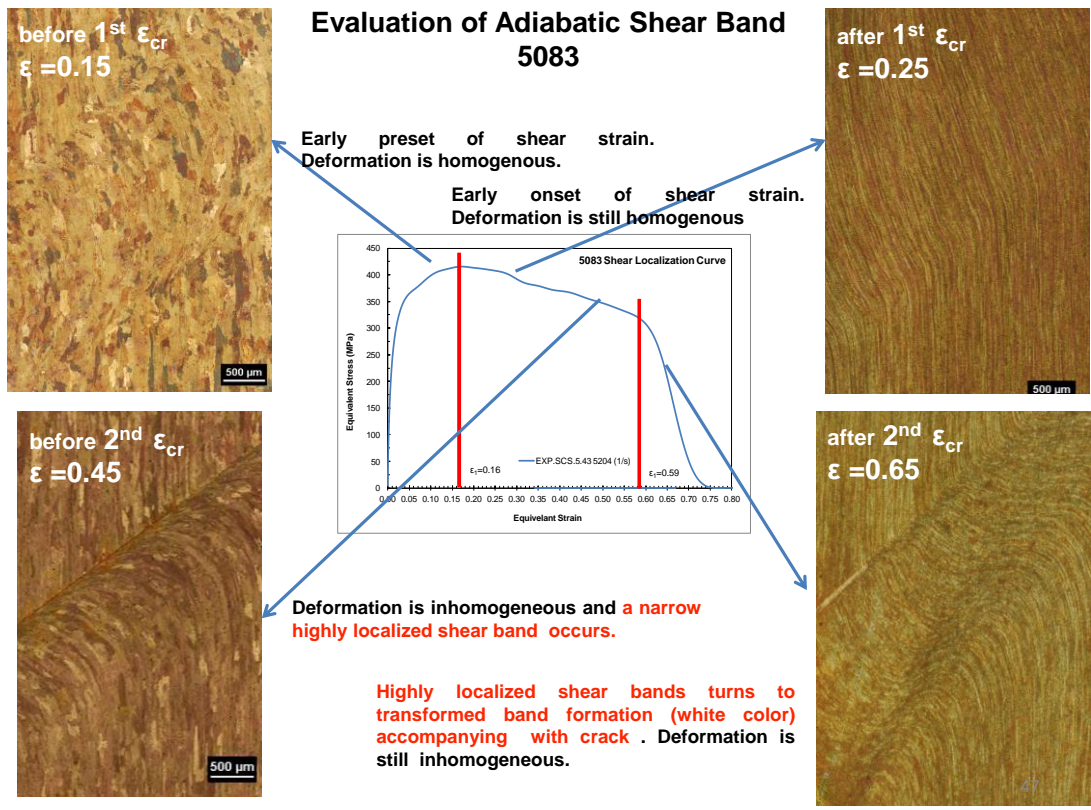


Figure 4.15 Evolution of localized shear band for 5083

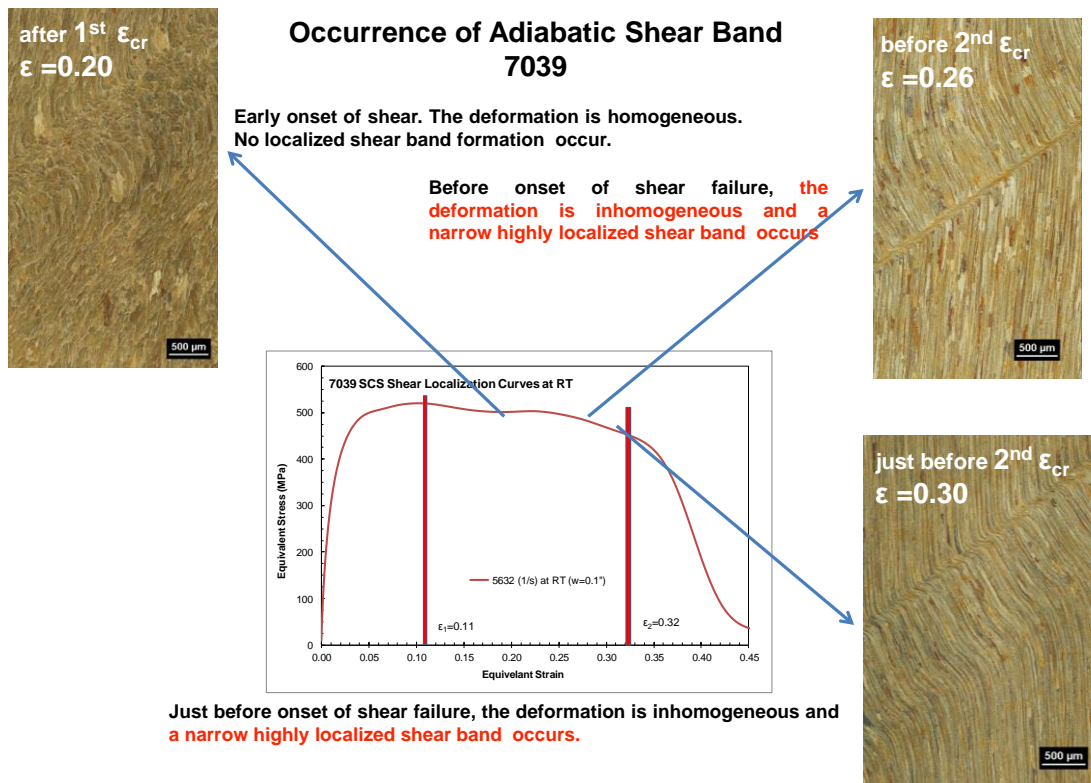


Figure 4.16 Evolution of localized shear band for 7039

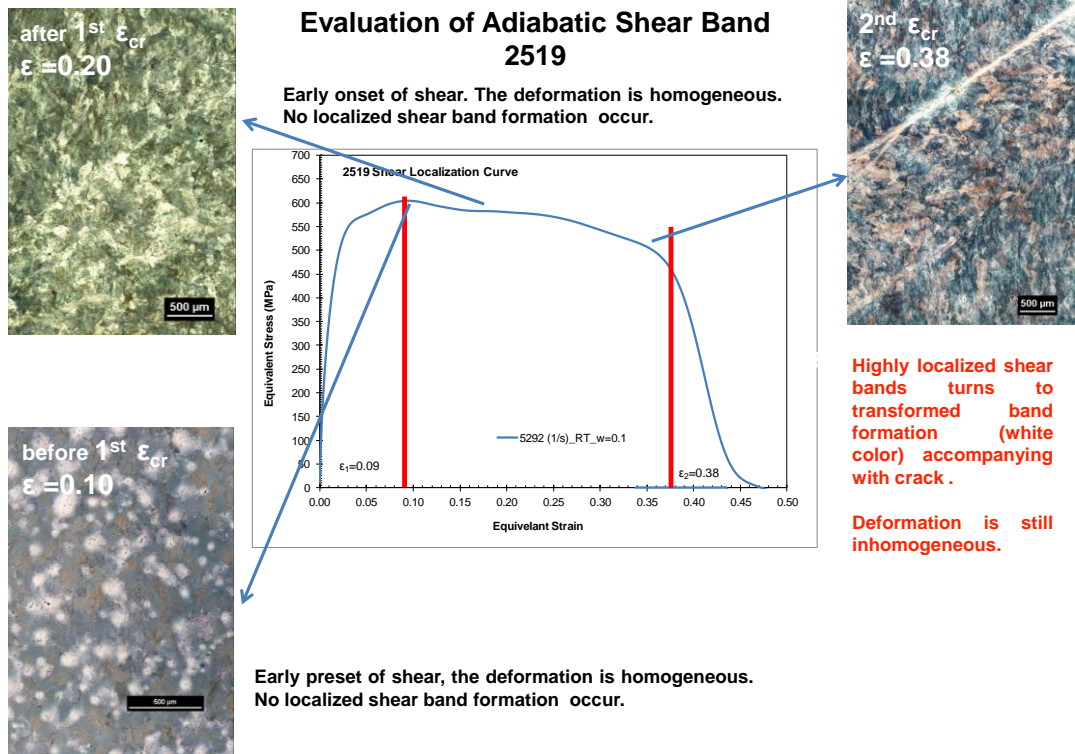


Figure 4.17 Evolution of localized shear band for 2519

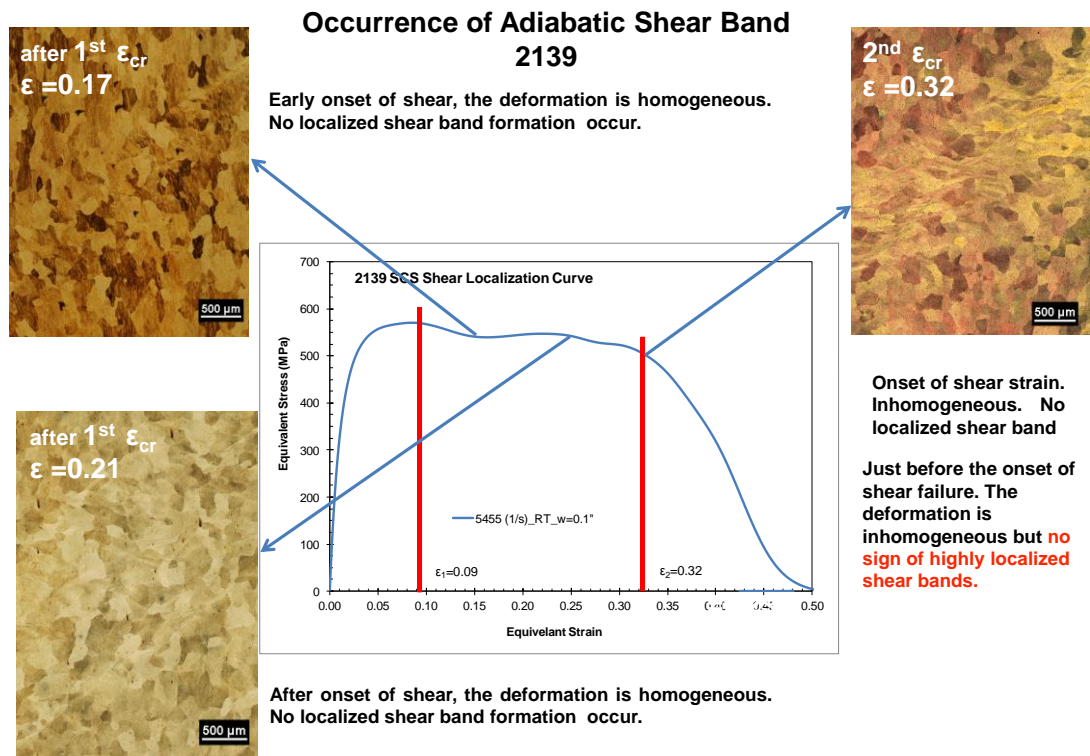


Figure 4.18 Evolution of localized shear band for 2139



## CHAPTER 5

### CALIBRATION OF MATERIAL MODELS

Aluminum armor alloys; 5083, 7039 and 2519 have been used in lightweight armored vehicles to provide protection against projectile/fragmentation impact as well as blast loading targeted to it. These dynamic loading events result in high strain rate loading that causes large strains and high temperatures due to the thermoplastic heating. Therefore, it is of utmost importance to investigate the deformation behavior of such aluminum alloys in a wide range of strain rates (from quasi-static to dynamic up to  $10^5 \text{ s}^{-1}$ ) and temperatures (from room temperature to elevated temperatures) and develop predictive constitutive models to facilitate the analysis and optimization of structures against ballistic threats.

To this end, an extensive experimental database has been established to investigate and document the rate and temperature dependent flow behavior of four different aluminum armor alloys under a wide range of strain rates spanning quasi-static and dynamic loading regimes. The procedure and results of these experiments have been discussed in preceding chapters. This chapter will discuss the applicability of various existing phenomenological and physics-based models to the mechanical response of aluminum armor alloys, and also present an effort to further modify some of these constitutive models for improving their predictive capability.

In order to evaluate the performance of currently available constitutive models initially, Johnson-Cook (JC) and Zerilli-Armstrong (ZA) were chosen since they are widely used and easily implemented in non-linear finite element codes such as codes such as AUTODYN, LS-DYNA, ABAQUS and ANSYS Explicit. Unfortunately, none of these models provided satisfactory correlation with

experimental data due to the rather complex behavior of aluminum alloys investigated. Then, relatively more recent modified versions of these models; Modified JC (MJC) and Modified ZA (MZA), are considered for the prediction of material behavior in a wide range of strain rates and temperatures. A most recently developed model [58] obtained by further modifying MZA was also included in this comparative analysis. So, in total five material models which are Johnson-Cook (JC), Modified JC (MJC) as phenomenological models and Zerilli-Armstrong model (ZA), Modified ZA (MZA) and Turkkan-Vural MZA(TVMZA) as physics-based models were used within the scope of this study. These five material models have been discussed in detail in Chapter 2.

The material model evaluation has been done at both room and elevated temperature (220 °C) for all five material models over a wide range of strain rates. The reason for choosing 220 °C (493 K) is that the flow stress starts decreasing at a higher rate beyond this point (see Figure 4.2), and it corresponds to about half the melting temperature in Kelvin scale. At higher temperatures, the recrystallization of microstructure becomes a serious concern and none of the existing models can account for microstructure evolution.

## **5.1 Phenomenological (Engineering or empirical) Constitutive Models**

Calibration of phenomenological or empirical models is carried out by means of fitting model equations to the experimental data and finding model parameters without considering the physical processes causing the observed behaviour. These empirical models are also named engineering models as they are more commonly used in engineering applications than the physically based material models.

### **5.1.1 Johnson-Cook (JC) Model**

Johnson-Cook (JC) [48] model is the most widely used phenomenological model, mainly because of its simplicity, that describes the rate and temperature dependent flow stress of metals. JC model uses equivalent (von Mises) flow stress as a function of equivalent plastic strain, strain rate and temperature. This model is generally used in many explicit FE solvers to analyze terminal ballistics and impact problems.



In this model, flow stress is based on multiplicative decomposition of strain hardening, strain rate hardening and thermal softening terms as in the following:

$$\sigma = (\sigma_0 + B\varepsilon^n) \left( 1 + C \ln \frac{\dot{\varepsilon}}{\dot{\varepsilon}_0} \right) [1 - (T^*)^m] \quad (5.1)$$

$$T^* = \left( \frac{T - T_r}{T_m - T_r} \right)$$

where  $T^*$  is homologous temperature,  $T_r$  is the reference temperature at which the calibration is done (typically room temperature), and  $T_m$  is a representative melting temperature, not necessarily the absolute melting temperature, measured in Kelvin.

Dimensionless strain rate is given by;

$$\left( \frac{\dot{\varepsilon}}{\dot{\varepsilon}_0} \right)$$

where  $\dot{\varepsilon}$  is equivalent plastic strain rate and  $\dot{\varepsilon}_0$  is a reference strain rate defined by the user, which is usually chosen in quasi-static regime for the calibration of strain hardening parameters. Remaining constants are the model parameters that need to be determined by a best fit process (least squares, multiple regression analysis, etc.) to experimental data.

To establish the JC constitutive model for each alloy, the parameters  $A$ ,  $B$ ,  $n$ ,  $C$  and  $m$  should be determined, based on quasi-static and dynamic experiments in a wide range of strain, strain rates and temperatures. These parameters were determined in two steps.

Step 1: Calibration of only first and third brackets in Equation 5.1. The strain hardening and the thermal softening terms are calibrated first by using the experimental data at various temperatures at the reference strain rate. These two terms are calibrated together to obtain the best fitting results because thermal softening also affects the hardening characteristics of material.

Step 2: Calibration of second bracket in Equation 5.1. The strain rate sensitivity is, then, calibrated by fitting the model to the variation of flow stress with strain rate, which is extracted from experimental data at varying strain rates in both quasi-static and dynamic regimes.

The model parameters determined by using the aforementioned calibration procedure are tabulated in Table 5.1 for two of the aluminum alloys. The resulting model predictions for flow stress as a function of strain, strain rate and temperature can be found in Figure 5.1-5.4 for a wide range of strain rates and temperatures.

Table 5.1 JC Material Model Parameters for 5083 and 2139 Alloys

Model Parameters	5083	2139
A (MPa)	300	418
B (MPa)	230	250
T <sub>0</sub> (K)	0	30
T <sub>m</sub> (K)	620	640
n	0.24	0.1
m	3.5	3.5
C	0.003	0.003

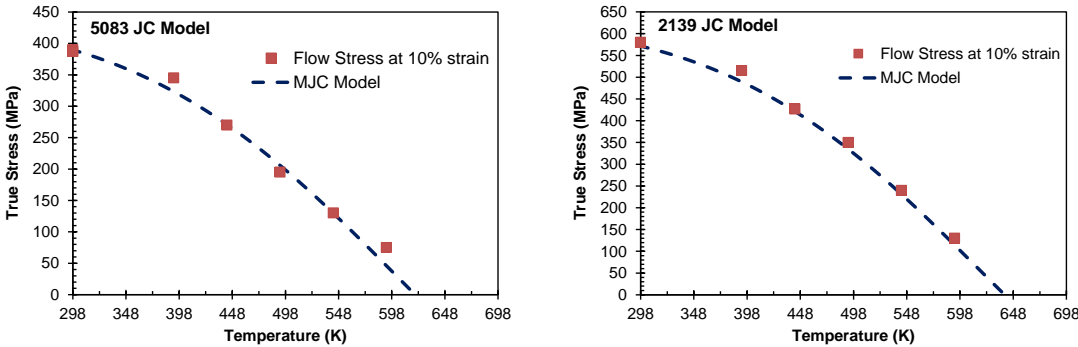


Figure 5.1 Flow stress as a function of temperature for 5083 and 2139 at 10% offset strain and at a strain rate of 10<sup>-3</sup> s<sup>-1</sup>: experimental data versus the prediction of JC model

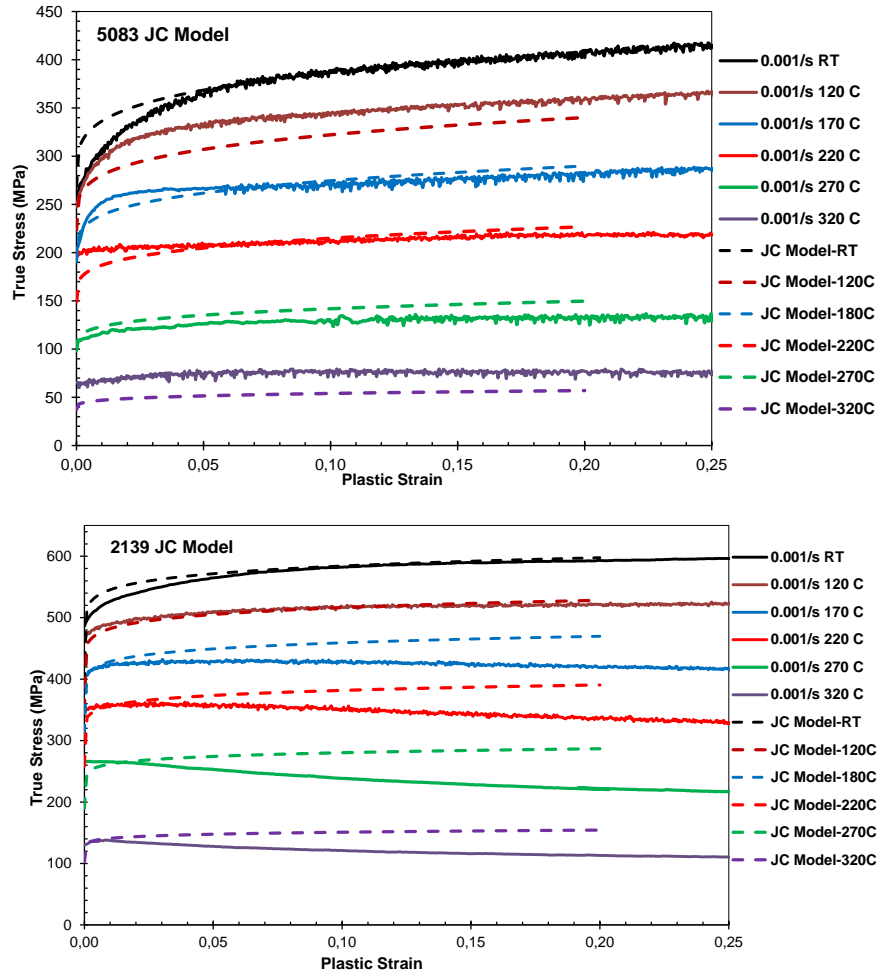


Figure 5.2 Flow stress versus plastic strain for 5083 and 2139 at different temperatures and at a strain rate of  $10^{-3} \text{ s}^{-1}$ : experimental data (solid lines) versus the predictions of JC model (dashed lines)

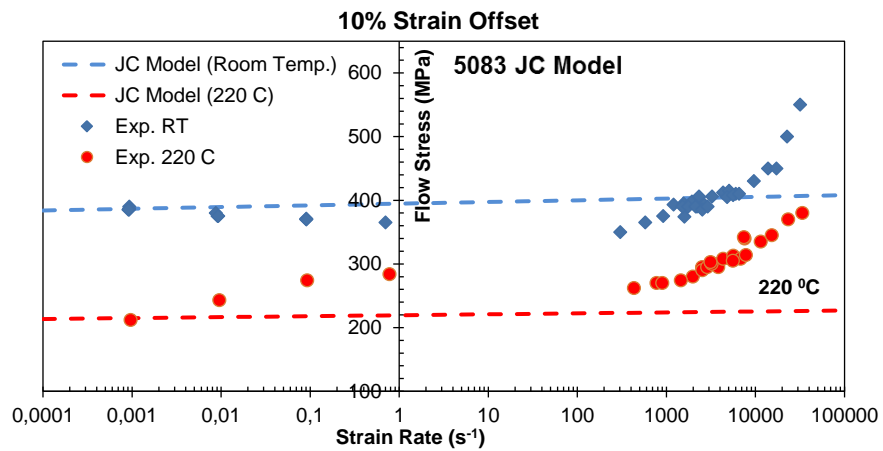


Figure 5.3 Flow stress at 10% offset strain versus strain rate for 5083 and 2139 alloys at both RT and elevated temperature: experimental data versus the prediction of JC model.

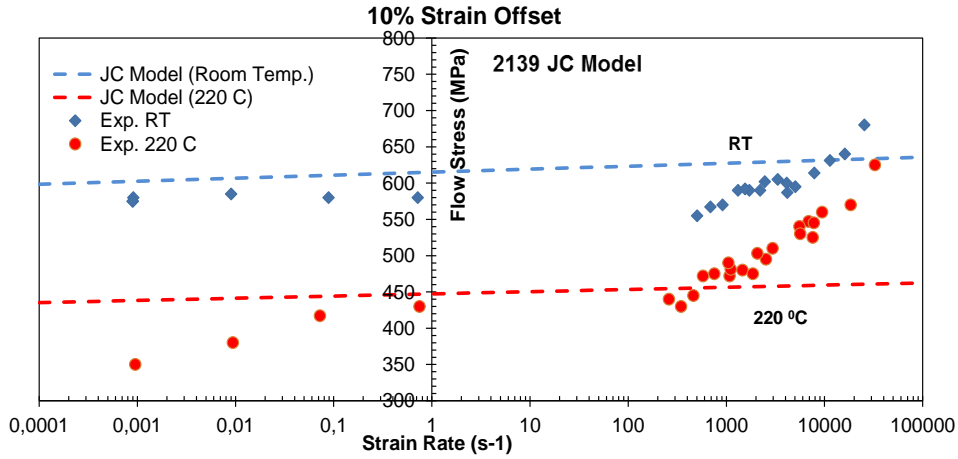


Figure 5.3 Continued.

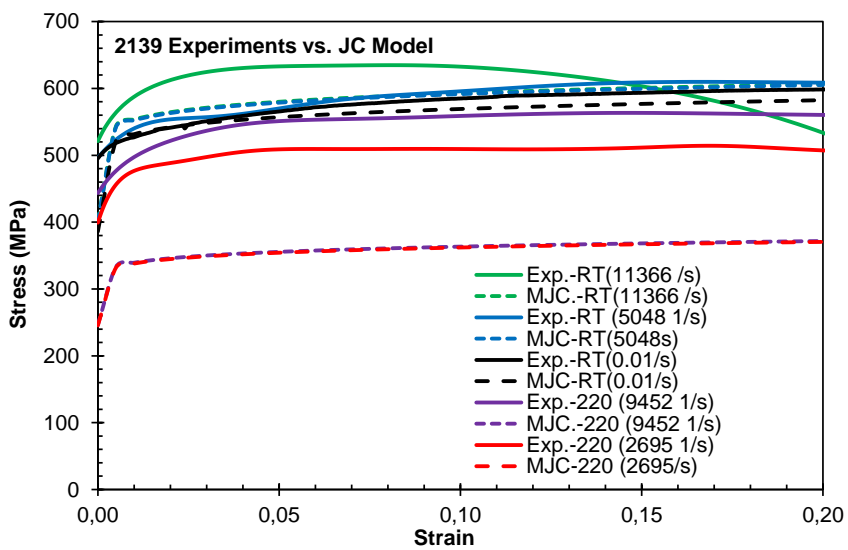
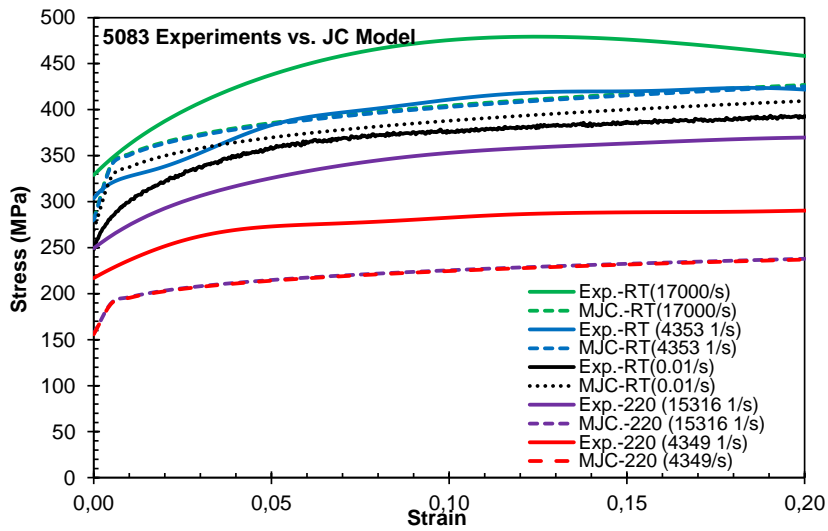


Figure 5.4 Flow stress versus plastic strain for 5083 and 2139 at different strain rates and temperatures: experimental data versus the prediction of JC model

A close inspection of Figures 5.1 through 5.4 shows that JC model poorly fits to experimental data. One of the shortcomings with this constitutive equation is that strain rate and temperature effects on the flow stress are uncoupled. This implies that the strain rate sensitivity (SRS) is independent of temperature, which is not the real case generally observed for most metals [78]. Additionally a different problem with JC model is observed as far as the SRS, especially in dynamic regime, is concerned. The JC model proposes a single SRS constant while the experimental data clearly indicates the existence of different strain rate dependencies in quasi-static and dynamic loading regimes.

Vural et al [10] also pointed out about these shortcomings of JC model and proposed a modified JC model, which will be discussed next.

### 5.1.2 Modified Johnson-Cook (MJC) Model

The details of original JC and modified JC (MJC) models are presented in Section 2.3.1.2. The modified model [10] is defined by Equation 2.48 and briefly reviewed here:

$$\begin{aligned} \sigma &= (A + B\varepsilon^n) \left( 1 + C \ln \frac{\dot{\varepsilon}}{\dot{\varepsilon}_0} \right) [1 - (T^*)^m] & T^* &= \left( \frac{T - T_r}{T_m - T_r} \right) \\ B &= B_0 (1 - (T^*)^m) & C &= C_1 (T_r^*)^p + C_2 H(\dot{\varepsilon}, \dot{\varepsilon}_t, k) \quad (2.48) \\ H(\dot{\varepsilon}, \dot{\varepsilon}_t, k) &= \frac{1}{2} + \frac{1}{2} \tanh \left( k \ln \frac{\dot{\varepsilon}}{\dot{\varepsilon}_t} \right) = \frac{1}{1 + e^{-2k \ln(\dot{\varepsilon}/\dot{\varepsilon}_t)}} & T_r^* &= \left( \frac{T - T_0}{T_r - T_0} \right) \\ \dot{\varepsilon}_0 &= \dot{\varepsilon}_{01} \left\{ 1 + \left[ \left( \frac{\dot{\varepsilon}_t}{\dot{\varepsilon}_{01}} \right)^{(c_2)(C_1(T_r^*)^p + C_2)} - 1 \right] H(\dot{\varepsilon}, \dot{\varepsilon}_t, k) \right\} \end{aligned}$$

The main modifications over original JC model are (i) introduction of a stronger coupling between temperature and strain hardening through modified  $B$  parameter, (ii) recognition of dual rate sensitivity in quasi-static and dynamic regimes via  $C_1$  and  $C_2$ , respectively, with a smoothly transitioning Heaviside step function and (iii) inclusion of the temperature dependence of rate sensitivity in quasi-static regime as observed in experiments. The parameters of MJC constitutive model discussed in Section 2.3.1.2 were determined by using least square fitting. The procedures to find

the parameters were described by Vural [10]. According to this procedure, the parameters determined for each material are tabulated in Table 5.2;

Table 5.2 MJC Material Model Parameters for 5083 and 2139 Alloys

Model Parameters	5083	2139
A (MPa)	260	484
B (MPa)	210	130
T <sub>0</sub> (K)	280	280
T <sub>m</sub> (K)	650	640
n	0.2	0.15
m	3	3.19
p	1.75	1.75
C <sub>1</sub>	0.00001	0.00001
C <sub>2</sub>	0.16	0.08
$\dot{\epsilon}_{01}$	0.001	0.001
$\dot{\epsilon}_t$	4300	3000
k	400	100

Using these parameters, MJC model predictions are compared with experimental data for the alloys. Comparison results are shown in Figures 5.5 through 5.8.

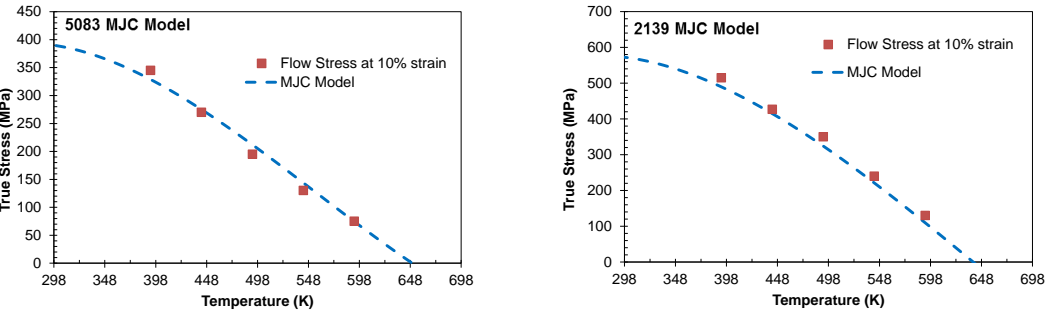


Figure 5.5 Flow stress as a function of temperature for 5083 and 2139 at 10% offset strain and at a strain rate of  $10^{-3} \text{ s}^{-1}$ : experimental data versus the prediction of MJC model.

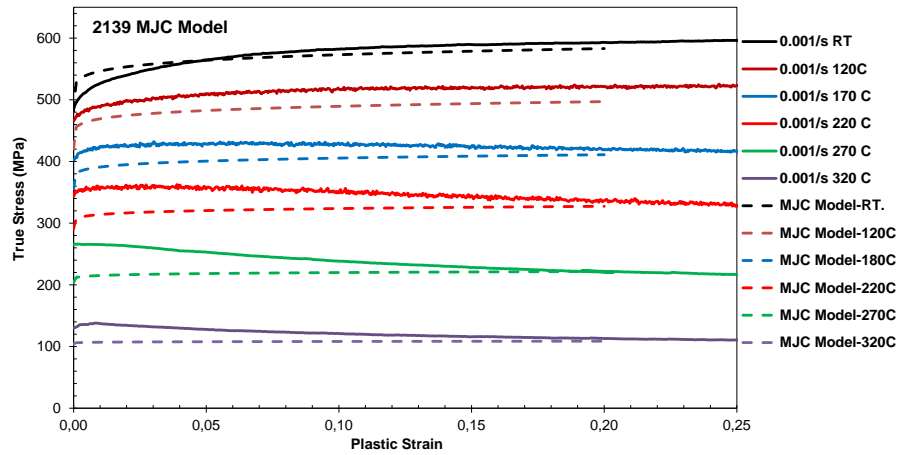
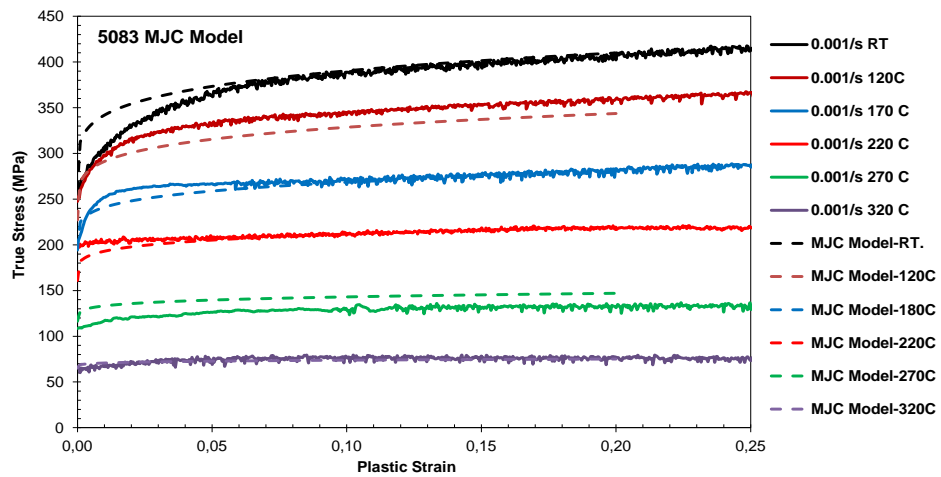


Figure 5.6 Flow stress versus plastic strain for 5083 and 2139 at different temperatures and at a strain rate of  $10^{-3} \text{ s}^{-1}$ : experimental data (solid lines) versus the prediction of MJC model (dashed lines)

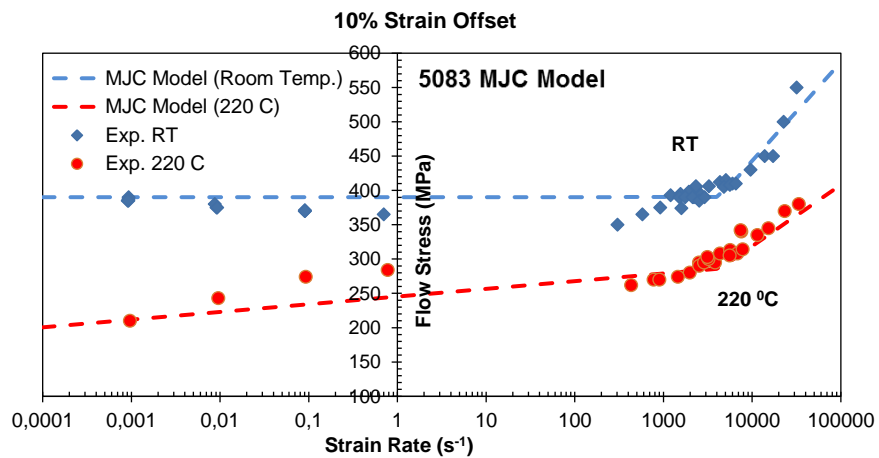


Figure 5.7 Flow stress at 10% offset strain versus strain rate for 5083 and 2139 alloys at RT and elevated temperature: experimental data versus the prediction of MJC model.

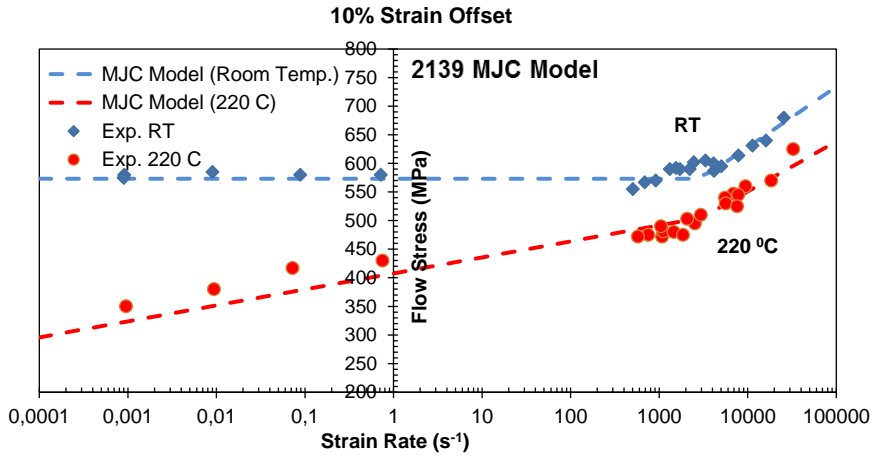


Figure 5.7 Continued

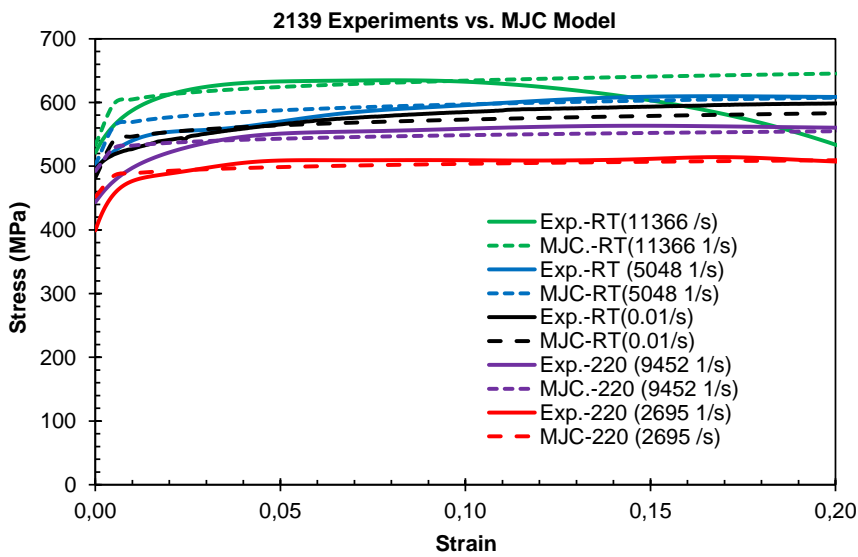
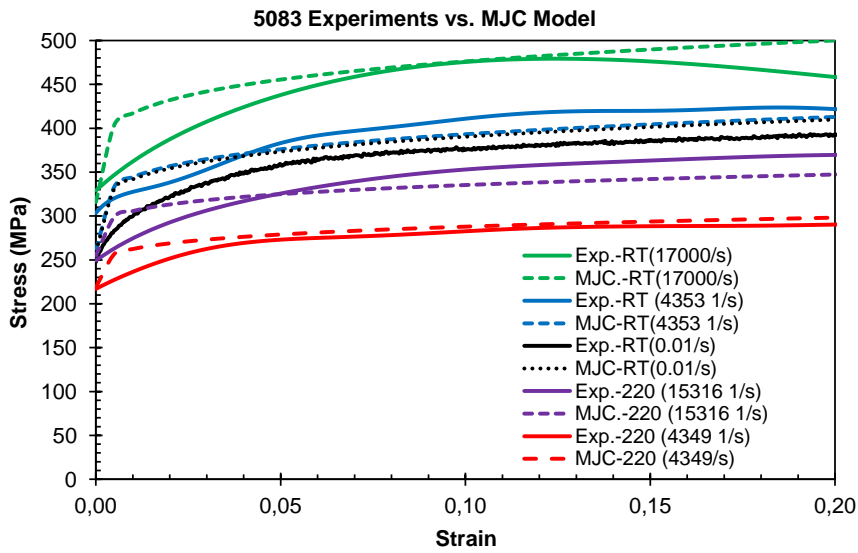


Figure 5.8 Flow stress versus strain for 5083 and 2139 at different strain rates and RT and elevated temperature: experimental data versus the prediction of MJC model.



It can be seen from the Figures 5.5-5.8, MJC model fits to the experimental data significantly better than the original JC model except for the quasi-static regime at elevated temperatures. This is consistent with the fact that this model assumes a constant SRS until moderate strain rates ( $10\text{-}10^2\text{ s}^{-1}$ ) where thermal softening effects may become apparent due to insufficient heat conduction time from plastically deforming specimen to the loading platens [79].

## 5.2 Physical based Constitutive Models

Unlike phenomenological models where a combination of mechanistic and empirical approach is dominant, physically based constitutive models rely on the mathematical description of underlying deformation mechanisms, mostly emanating from dislocation dynamics, and their coupling with macroscopic field variables [80].

Zerilli-Armstrong (ZA) model emerges as the most widely used physically based material model in literature and, therefore, will be discussed next.

### 5.2.1 Zerilli-Armstrong (ZA) Model

The Zerilli-Armstrong (ZA) model [51-53] is based on simplified dislocation mechanics, whose details are presented in Section 2.3.2.1. The model, which is defined by Equations 2.62 and 2.63, and its performance is briefly reviewed here;

$$\sigma = \sigma_a + B e^{-\beta T} + B_0 \varepsilon^{\frac{1}{2}} e^{-\alpha T} \quad (2.62)$$

where

$$\begin{aligned} \alpha &= \alpha_0 - \alpha_1 \ln(\dot{\varepsilon}) \\ \beta &= \beta_0 - \beta_1 \ln(\dot{\varepsilon}) \end{aligned} \quad (2.63)$$

$$\sigma_a = \frac{k}{\sqrt{l}} + \sigma_s$$

The calibration is done in one step:

Step 1: Calibration of flow stress,  $\sigma = \sigma_a + B e^{-\beta T} + B_0 \varepsilon^{\frac{1}{2}} e^{-\alpha T}$ , according to the results of all experiments.

The parameters determined in accordance with ZA model are tabulated in Table 5.3 and the resulting flow stress plots as a function of strain, strain rate and temperature

in a wide range of strain rates at room and elevated temperatures are presented in Figures 5.9 through 5.11 together with experimental data for comparison.

Table 5.3 ZA Material Model Parameters for 5083 and 2139 Alloys

Model Parameters	5083	2139
$\sigma_a$ (MPa)	20	40
$B$ (MPa)	390	600
$B_0$ (MPa)	390	600
$\beta_0$ (K <sup>-1</sup> )	0.001	0.001
$\beta_1$ (K <sup>-1</sup> )	0.00002	0.00003
$\alpha_0$ (K <sup>-1</sup> )	0.02	0.002
$\alpha_1$ (K <sup>-1</sup> )	0.00001	0.00002

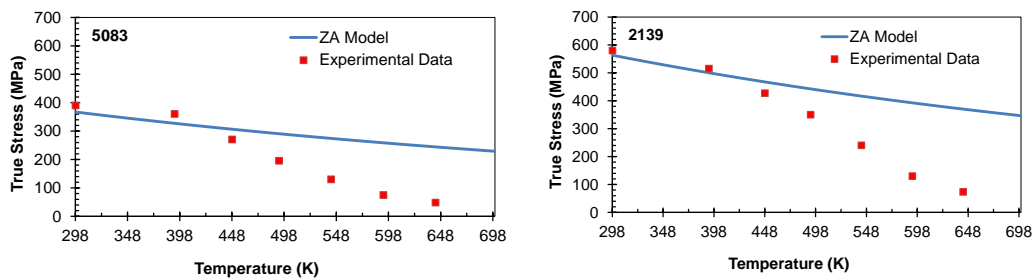


Figure 5.9 Flow stress as a function of temperature for 5083 and 2139 at 10% offset strain and at a strain rate of  $10^{-3} \text{ s}^{-1}$ : experimental data versus the prediction of ZA model

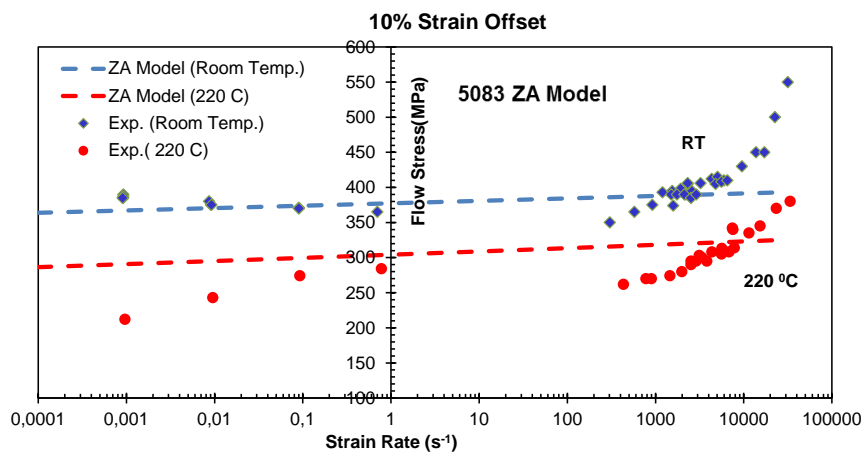


Figure 5.10 Flow stress at 10% offset strain versus strain rate for 5083 and 2139 alloys at RT and elevated temperature: experimental data versus the prediction of ZA model.

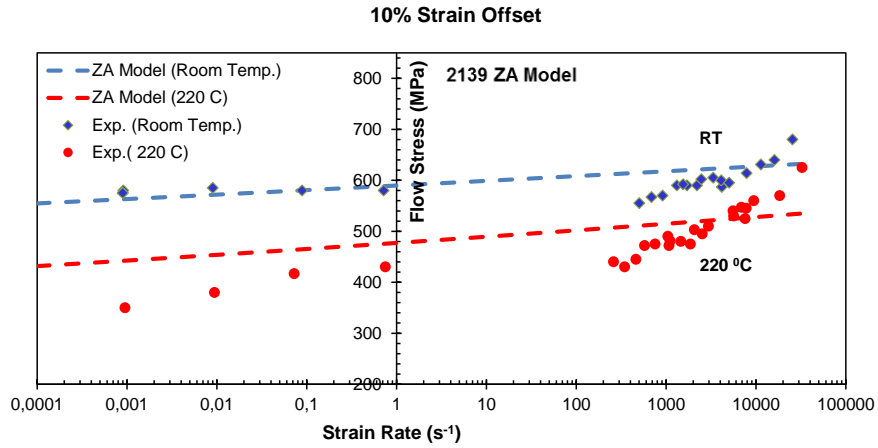


Figure 5.10 Continued

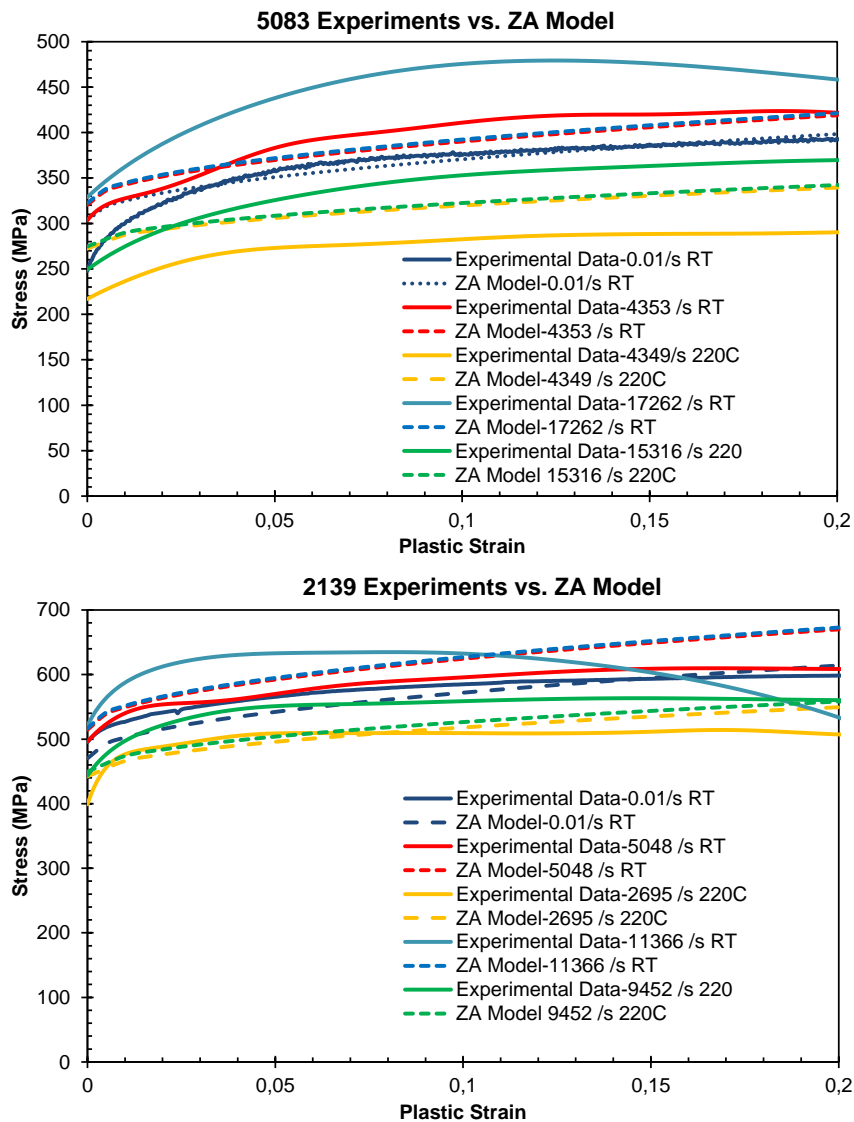


Figure 5.11 Flow stress versus strain for 5083 and 2139 at different strain rates and temperatures: experimental data versus the prediction of ZA model.

The comparisons between experimental data and predicted results by ZA model as shown in Figure 5.9, 5.10 and 5.11 clearly reveal that no good fit was available with this model as it was in JC model. Shortcomings such as uncoupled strain rate and temperature, constant SRS in all three regimes of quasi-static, intermediate and high strain rates are the same as those with JC model. Another common shortcoming of ZA and JC models is that they don't predict dynamic behavior accurately above  $10^4 \text{ s}^{-1}$  strain rates. In other words, this model lacks catching the drastic increase in flow stress above  $10^4 \text{ s}^{-1}$ . As a result, at strain rates higher than  $10^4 \text{ s}^{-1}$  and at elevated temperatures in both quasi-static and dynamic regimes, the ZA model cannot predict the material behavior accurately.

Therefore Zerilli and Armstrong modified [54] the thermal component of their model (ZA model) to include dynamic recovery process and dislocation drag mechanisms in the dynamic loading regime as it was done in MJC by Vural et al [10].

### 5.2.2 Modified Zerilli-Armstrong (MZA) Model

The details of Modified Zerilli-Armstrong (MZA) model [53-54] is discussed in Section 2.3.2.2. The model is defined by Equation 2.71 and its predictive capability is briefly reviewed here;

$$\sigma = \sigma_a + \sigma^*$$

$$\sigma_{th} = B e^{-\beta T} + \left[ A \sqrt{\left( \frac{1}{w} (1 - e^{-w\varepsilon}) \right)} \right] e^{-\alpha T} \quad (2.71)$$

$$\sigma^* = 0.5 \sigma_{th} \left[ 1 + \left( 1 + \frac{4C_0 \dot{\varepsilon} T}{\sigma_{th}} \right)^{\frac{1}{2}} \right]$$

where;

$$\alpha = \alpha_0 - \alpha_1 \ln(\dot{\varepsilon})$$

$$\beta = \beta_0 - \beta_1 \ln(\dot{\varepsilon})$$

The calibration is done in one step.

Step 1: Calibration of flow stress,  $\sigma = \sigma_a + \sigma^*$  according to the results of all experiments.

The model parameters determined are tabulated in Table 5.4 and the resulting flow stress plots as a function of strain, strain rate and temperature in a wide range of strain rates at room and elevated temperatures are presented in Figures 5.12 through 5.14.

Table 5.4 MZA Material Model Parameters for 5083, and 2139 Alloys

Model Parameters	5083	2139
$\sigma_a$ (MPa)	25	100
$A$ (MPa)	750	450
$B$ (MPa)	550	800
$C_0$ ( $10^{-5}$ MPa/K)	2.3	2
$w$	45	45
$\beta_0$ ( $K^{-1}$ )	0.002	0.002
$\beta_1$ ( $K^{-1}$ )	0	0
$\alpha_0$ ( $K^{-1}$ )	0.003	0.003
$\alpha_1$ ( $K^{-1}$ )	0.00001	0.00003

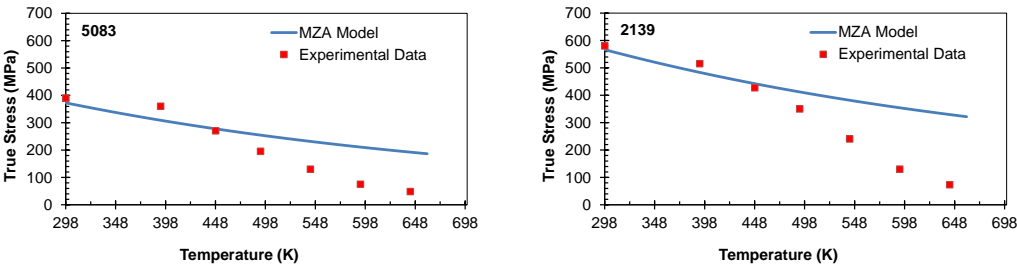


Figure 5.12 Flow stress as a function of temperature for 5083 and 2139 at 10% offset strain and a strain rate of  $10^{-3} s^{-1}$ : experimental data versus the prediction of MZA model

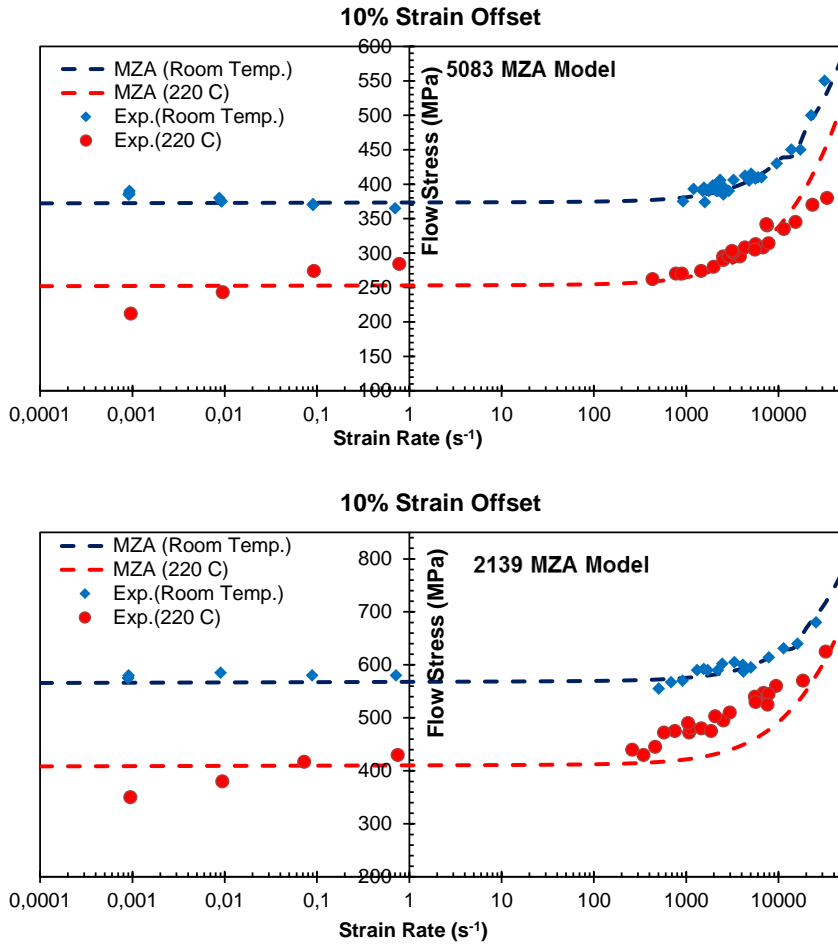


Figure 5.13 Flow stress versus strain rate for 5083 and 2139 alloys at RT and elevated temperature: experimental data versus the prediction of MZA model

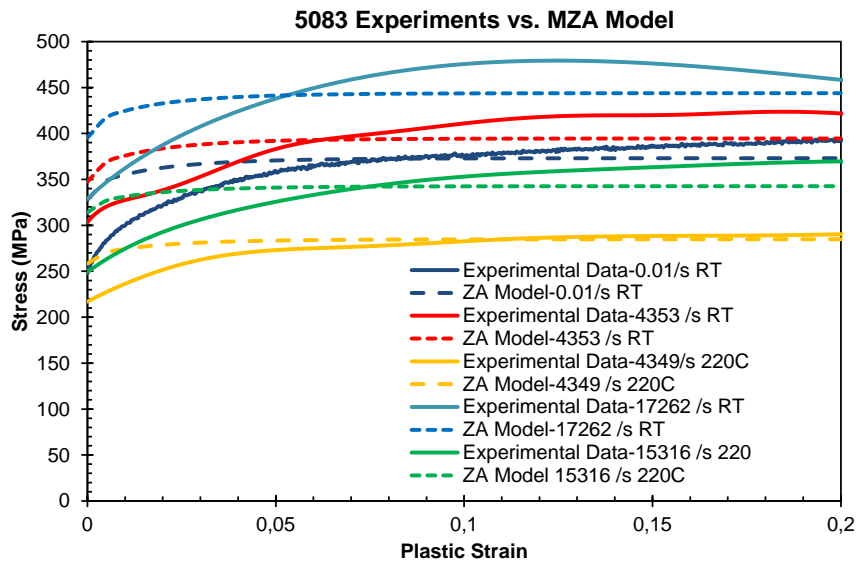


Figure 5.14 Flow stress versus strain for 5083 and 2139 at different strain rates and temperatures: experimental data versus the prediction of MZA model.

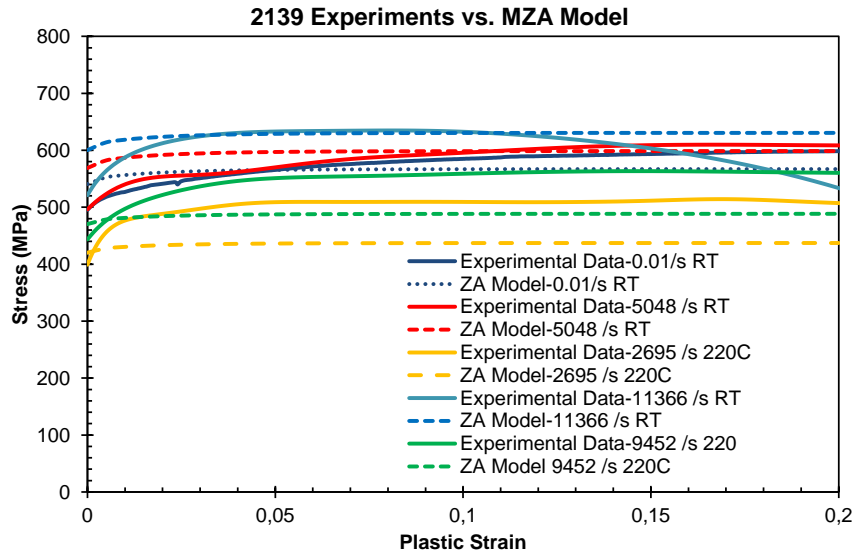


Figure 5.14 Continued

It can be seen from the Figures 5.12 through 5.14, MZA model well fits to the experimental data at room temperature while it poorly fits to the experimental data at elevated temperature. This is because this model generates a common SRS at both room temperature and elevated temperatures by failing to recognize stronger coupling of thermal activation process with strain rate at higher temperatures. On the other hand, MZA model captures increased SRS at high strain rates due to the addition of dislocation drag mechanism which becomes effective at strain rates above  $10^4 \text{ s}^{-1}$  as discussed in Section 2.1.2.

Thus, unlike ZA model, MZA model gives high SRS in dynamic regime at both room and elevated temperatures. But, the experimental data shown in Figure 5.13 exhibits different SRS at elevated temperature.

It is important to note that, in both MZA and ZA models, flow stress is coupled to the temperature in an exponential manner, which gives unrealistic results after some point. Turkkan-Vural [58] modified the MZA model in order to accurately capture the experimental data in a greater temperature range, the exponential relation between the flow stress and the temperature should be coupled. Only way to modify this relation is to make one of the parameters temperature dependent [58].

### 5.2.3 Turkkan -Vural Modifications to MZA (TVMZA) Model

The details of Turkkan-Vural MZA (TVMZA) model [58] is presented in Section 2.3.2.3 The model is defined by Equation 2.76 and Equation 2.77 and its predictive performance will be briefly reviewed here;

$$\sigma = \sigma_a + \sigma^*$$

$$\sigma_{th} = \left[ A(T) \sqrt{1 + \frac{1}{w} (1 - e^{-w\varepsilon})} \right] e^{-\alpha T} \quad (2.76)$$

$$\sigma^* = 0.5\sigma_{th} \left[ 1 + \left( 1 + \frac{4C_0\dot{\varepsilon}T}{\sigma_{th}} \right)^{\frac{1}{2}} \right] e^{-\alpha T}$$

where

$$\alpha = \alpha_0 - \alpha_1 \ln(\dot{\varepsilon})$$

$$A(T) = A \left( 1 - \left( \frac{T - T_0}{T_m - T_0} \right)^p \right) \quad (2.77)$$

The calibration is done in one step.

Step 1: Calibration of flow stress,  $\sigma = \sigma_a + \sigma^*$  according to the results of all experiments.

The model parameters are tabulated in Table 5.5 and resulting flow stress predictions as a function of strain, strain rate and temperature in a wide range of strain rates at room and elevated temperatures are presented in Figures 5.15 through 5.17 in comparison with experimental data.



Table 5.5 TVMZA Material Model Parameters for 5083 and 2139 Alloys

Model Parameters	5083	2139
$\sigma_a$ (MPa)	0	0
A (MPa)	310	470
$T_m$ (K)	650	630
$T_0$ (K)	120	140
$C_0$ ( $10^{-5}$ MPa/K)	2	1.4
$w$	9	11
$p$	3	4
$\alpha_0$ ( $K^{-1}$ )	0	0.000025
$\alpha_1$ ( $K^{-1}$ )	0.00001	0.00001

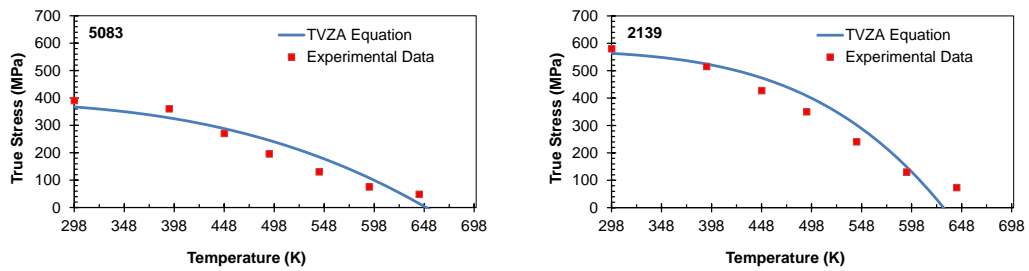


Figure 5.15 Flow stress as a function of temperature for 5083 and 2139 at 10% offset strain and at  $10^{-3} s^{-1}$ : experimental data versus the prediction of TVMZA model

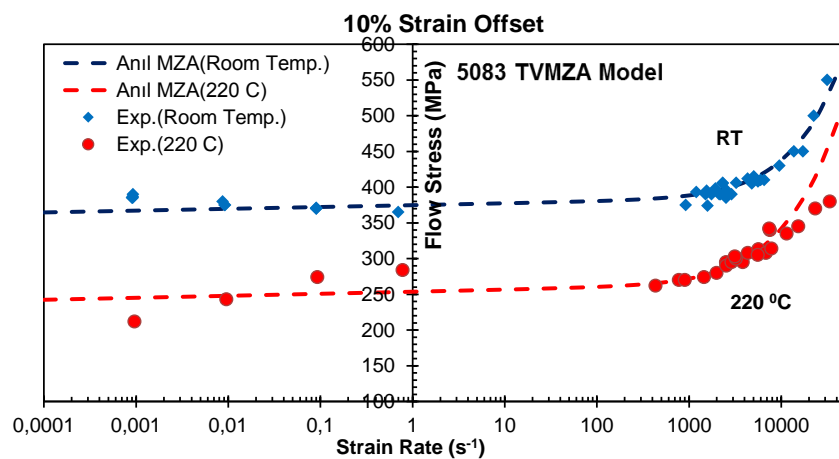


Figure 5.16 Flow stress at 10% offset strain versus strain rate for 5083 and 2139 alloys at RT and elevated temperature: experimental data versus the prediction of TVMZA model.

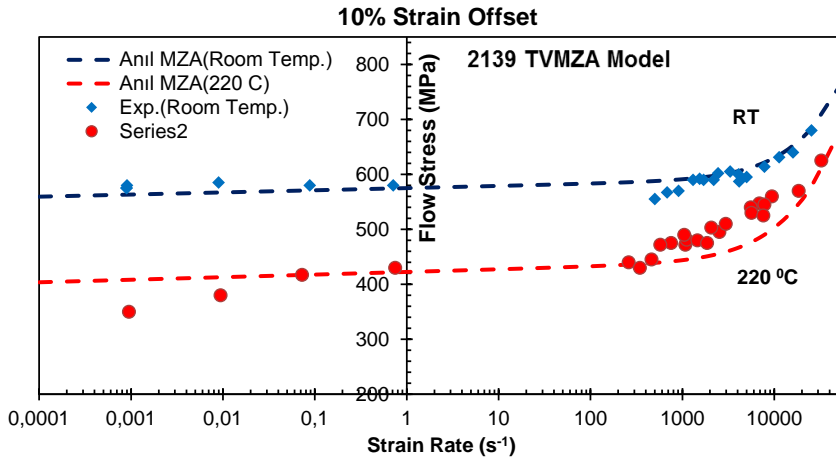


Figure 5.16 Continued

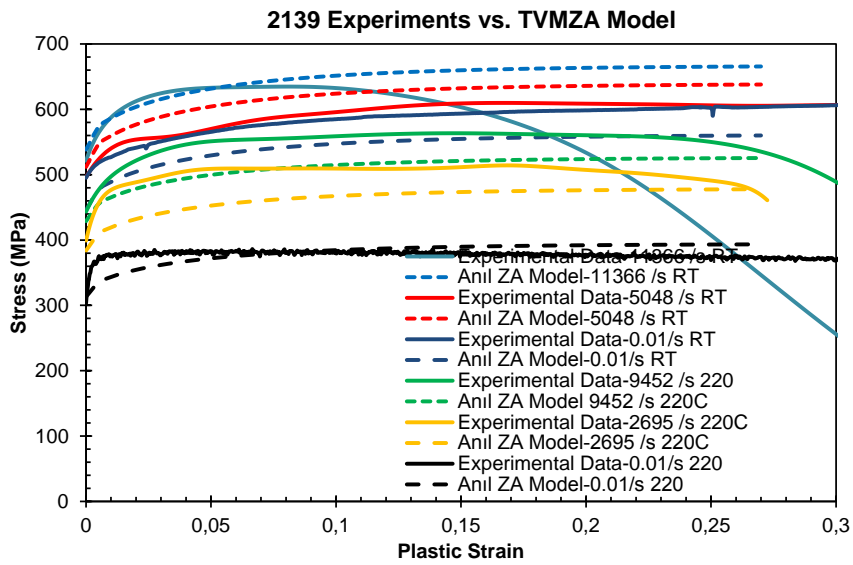
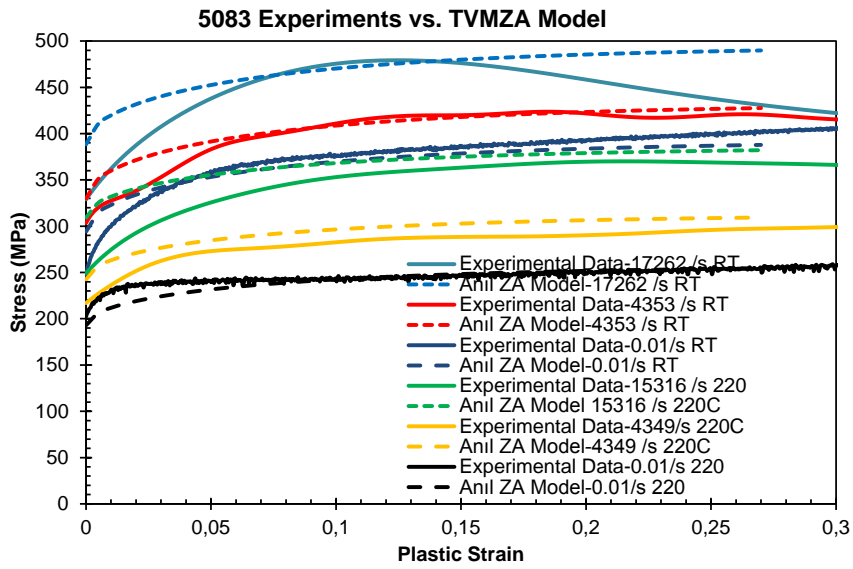


Figure 5.17 Flow stress versus strain for 5083 and 2139 at different strain rates and temperatures: experimental data versus the prediction of TVMZA model.

It is clearly seen from Figure 5.15 that modifications implemented in TVMZA model makes the thermal softening predictions more realistic for the aluminum alloys investigated in this study. However, prediction of the rate dependence of flow stress presented in Figure 5.16 remains practically the same as the MZA model. In other words, TVMZA model still has shortcomings in predicting SRS at elevated temperatures of quasi-static regime as in the case of ZA and MZA.

Although TVMZA model has a capability to accurately capture the experimental data in a greater temperature range and the exponential relation between the flow stress and temperature in MZA model which is now significantly altered in an attempt to include diffusion effects at elevated temperatures, TVMZA model does not take into consideration the interaction between temperature and strain rate hardening in quasi-static regime.

In an effort to overcome the shortcomings of JC, MJC, ZA, MZA and TVMZA models and to establish a modified model whose predictions at room and elevated temperatures in both quasi-static and dynamic regimes well fit to experimental data, we remarked the following findings:

- i. When original JC and ZA models are compared with modified versions (MJC, MZA and TVMZA), better predictions were obtained by modified versions of these phenomenological and physically based models.

- ii. While MJC has strain rate sensitivity (SRS) coupled with temperature for quasi-static and dynamic regimes differently, it assumes a constant SRS in quasi-static regime until transition strain rate ( $\dot{\epsilon}_t$ ) and a constant SRS for dynamic regime at both RT and elevated temperatures.

- iii. Furthermore, MJC model does not predict the dramatic increase in flow stress beyond strain rate of  $10^4 \text{ s}^{-1}$  which is considered to be the transition strain rate from thermally activated dislocation mechanism to viscous drag mechanism.

- iv. MZA and TVMZA almost have the same shortcomings in predicting the material behavior in quasi-static regime at elevated temperatures. While they predict

the material behavior correctly at RT for two distinct regimes and the dramatic increase in flow stress above the strain rate of  $10^4 \text{ s}^{-1}$ , these models do not predict the flow stress of quasi-static regime at elevated temperature accurately because of the assumption of the same SRS for RT and elevated temperature.

v. As a result, while the MJC, TVMZA and MZA models realistically predict the dynamic behavior of the aluminum alloys at room temperature in both quasi-static and dynamic regimes, they do not have a good capability to capture the experimental data at elevated temperatures.

#### **5.2.4 Proposed Model by combining MJC and TVMZA Model**

The basic ZA model assumed an exponential stress-temperature relationship in modeling the thermal stress component based on simplified dislocation mechanics. This exponential form is not applicable the metals particularly at elevated temperatures [81]. Abed and Vojjadjis [81] noticed that the explicit definition of  $\beta$  and  $\alpha$  given in Equation 2.63 clearly indicates that these parameters is not a constant, but rather a temperature dependent parameter. Furthermore, they state that while ZA model is known as a physically based model, actually ZA model is a combination of physical and phenomenological model since they formulated  $\beta$  and  $\alpha$  expressions according to experimental results.

Therefore, in order to overcome all these shortcomings of the commonly used models discussed above, we propose a new model by modifying TVMZA model by taking the following points into consideration:

i. MJC, TVMZA and MZA models provide good results at room temperature at both quasi-static and dynamic regimes.

ii. Since there is a significantly high SRS at elevated temperatures in quasi-static regime, the SRS should be temperature coupled. On the other hand, the SRSs in quasi-static and dynamic deformation regimes should be defined differently due to the difference in dominant mechanisms of resistance to dislocation motion.

iii. Since the deformation in dynamic regime is adiabatic, there is not enough time for heat diffusion via conduction while it has enough time for heat diffusion in quasi-static regime where the deformation is isothermal. Therefore, the temperature effects of elevated temperature which simulates the temperature raise within adiabatic shear bands (ASB's) cause a drop in flow stress in dynamic regime. Since this drop in flow stress is related with the thermal component of flow stress ( $\sigma_{th}$ ), it is expressed by a coefficient,  $D$  as  $D\sigma_{th}$ . The drop in flow stress occurs due to the transition from isothermal to adiabatic deformation (that corresponds to the transition from quasi-static to dynamic regime). As the strain rate increases in dynamic regime, the flow stress increases with the effect of SRS of dynamic regime at elevated temperature. The drop in flow stress is schematically shown in Figure 5.18. If there is no drop in flow stress (means  $D=0$ ), the flow stress will be the same as the flow stress at room temperature in dynamic regime. In this case, it can be assumed that there is no adiabatic deformation in the material.

iv. Therefore the parameter,  $D$  in proposed model can also be considered as the recognition of increasing thermal softening rate at elevated temperatures.

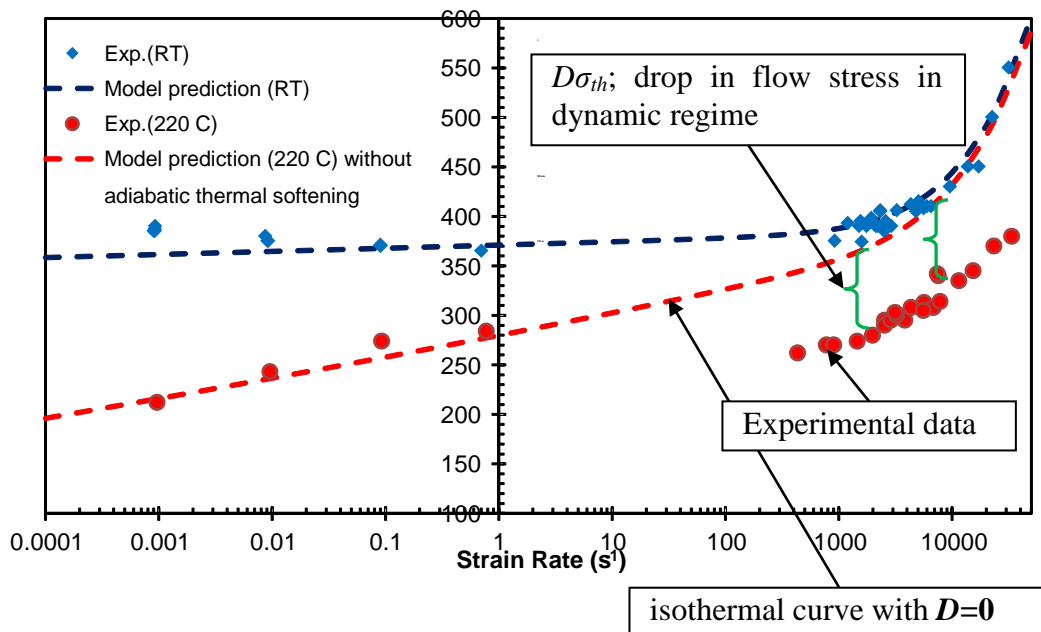


Figure 5.18 Flow stress versus strain rate without considering thermal softening in dynamic regime

Based on experimental data of each alloy in this study, a modification to TVMZA model is presented here by coupling thermal softening with strain rate through the smooth Heaviside step function of MJC and introducing a new parameter  $D$ ;

$$\sigma = \sigma_a + \sigma^*$$

$$\sigma_{th} = \left[ A(T) \sqrt{1 + \frac{1}{w} (1 - e^{-w\varepsilon})} \right] e^{-\alpha T} \quad (5.1)$$

$$\sigma^* = 0.5\sigma_{th} \left[ 1 + \left( 1 + \frac{4C_0\dot{\varepsilon}T}{\sigma_{th}} \right)^{\frac{1}{2}} \right] e^{-\alpha T} - \sigma_{th} (1 - T_r^*) \ln \left( \frac{\dot{\varepsilon}}{\varepsilon_0} \right) \left( C + D \left( \frac{1}{2} + \frac{1}{2} \tanh \left( \ln \frac{\dot{\varepsilon}}{\dot{\varepsilon}_0} \right) \right) \right)$$

where;

$$\alpha = \alpha_0 - \alpha_1 \ln(\dot{\varepsilon})$$

$$T_r^* = \left( \frac{T - T_0}{T_r - T_0} \right)^q$$

*Heaviside step function gives;  
0 in quasi-static  
1 in dynamic region.*

$$A(T) = A \left( 1 - \left( \frac{T - T_0}{T_m - T_0} \right)^p \right)$$

Thus the shortcomings of previously discussed models are effectively eliminated in this proposed model by introducing  $C$  and  $D$  parameters as shown in Equation 5.1. This modification eliminates the problems encountered in MJC, MZA and TVMZA models approximating the experimental data both in quasi-static and dynamic regimes as well as both at RT and higher temperatures. By this proposed modification;

i. Different strain rate sensitivity,  $C$ , for the quasi-static regime at an elevated temperature should be defined since SRS is quite different from that of room temperature. In other words,  $C$  is the isothermal strain rate sensitivity at elevated temperature, and its effect changes as temperature increases because of the preceding temperature term (see Equation 5.1).

ii. In dynamic regime, increased thermal softening rate at elevated temperatures is taken into account by modeling how much drop in flow stress occurs because of this thermal softening. So,  $D$  stands for the drop rate in strain rate hardening in

dynamic regime due to the temperature effects which is ultimately tied to thermoplastic heating.

The calibration is done in one step.

Step 1: Calibration of flow stress,  $\sigma = \sigma_a + \sigma^*$  according to the results of all experiments.

The parameters of proposed model are tabulated in Table 5.6 for aluminum alloys 5083, 7039, 2519 and 2139 and resulting flow stress plots as a function of strain, strain rate and temperature are presented in Figures 5.19 through 5.21.

Table 5.6 Parameters of Proposed Model for 5083, 7039, 2519 and 2139 Alloys

Model Parameters	5083	7039	2519	2139
$\sigma_a$ (MPa)	40	40	70	70
$A$ (MPa)	280	430	440	460
$T_m$ (K)	650	640	645	650
$T_0$ (K)	180	130	220	130
$C_0$ ( $10^{-5}$ MPa/K)	2.1	2	1.4	1.4
$w$	9	9	6	11
$p$	3	2.8	3	4
$q$	0.2	0.13	0.11	0.18
$\alpha_1$ ( $10^{-7}$ K $^{-1}$ )	1000	3000	4000	3500
$\alpha_2$ ( $10^{-8}$ K $^{-1}$ )	1000	1000	1000	400
$C$	0.16	0.5	0.25	0.2
$D$	<b>-0.2</b>	<b>-0.28</b>	<b>-0.16</b>	<b>-0.07</b>
$\dot{\epsilon}_{01}$	1	1	1	1

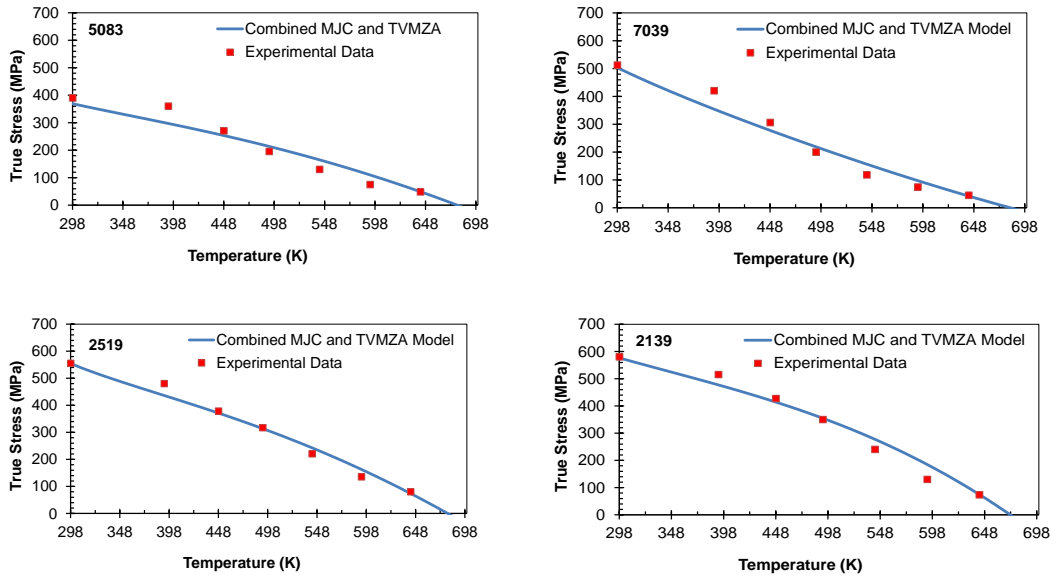


Figure 5.19 Flow stress at 10% offset strain as a function of temperature for 5083, 7039, 2519 and 2139 at a strain rate of  $10^{-3} \text{ s}^{-1}$ : experimental data versus the prediction of combined MJC and TVMZA model

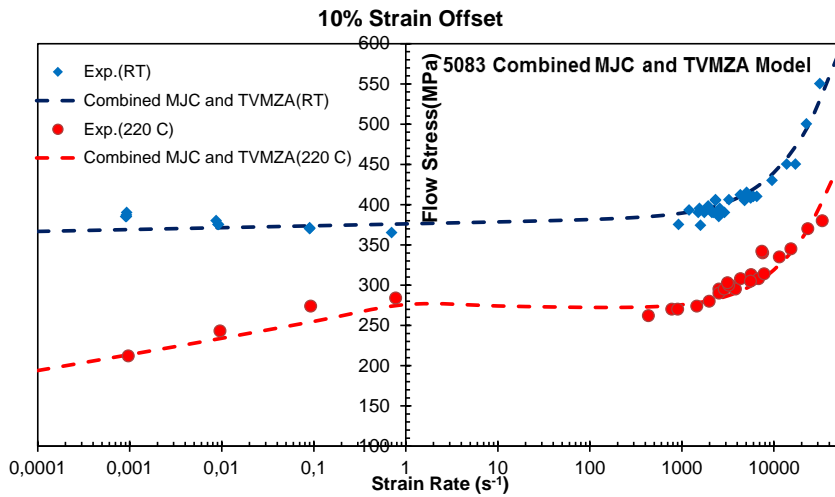


Figure 5.20 Flow stress at 10% offset strain versus strain rate for 5083, 7039, 2519 and 2139 alloys at RT and elevated temperature: experimental data versus the prediction of combined MJC and TVMZA model.



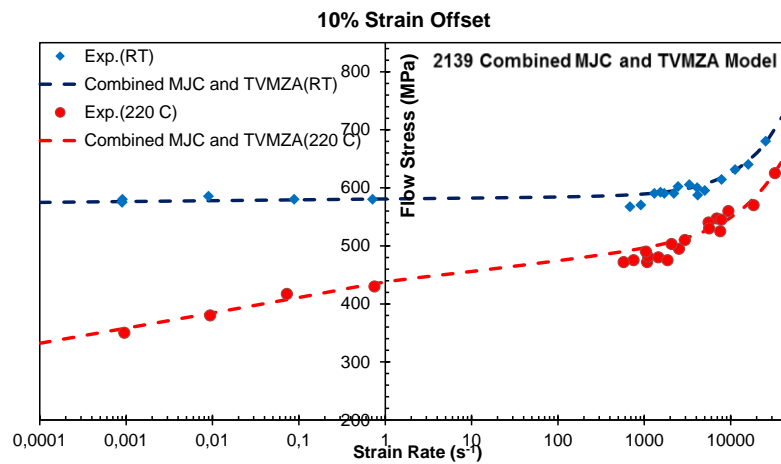
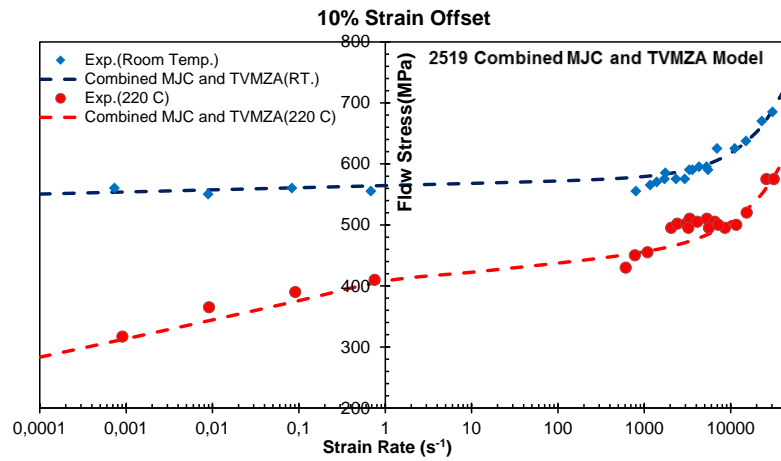
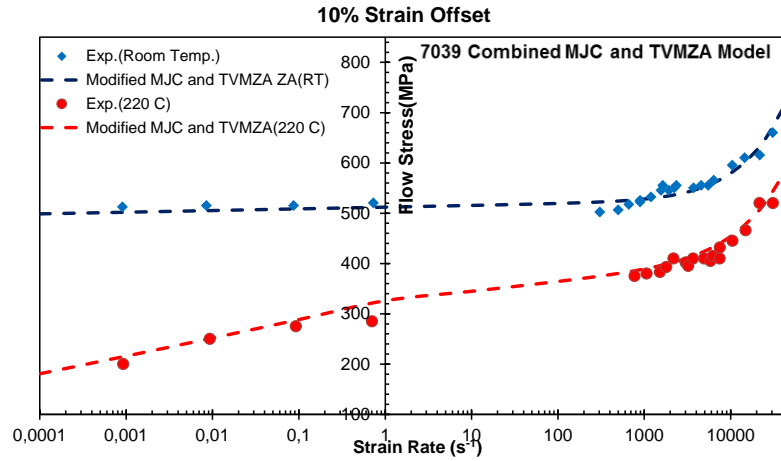


Figure 5.20 Continued.

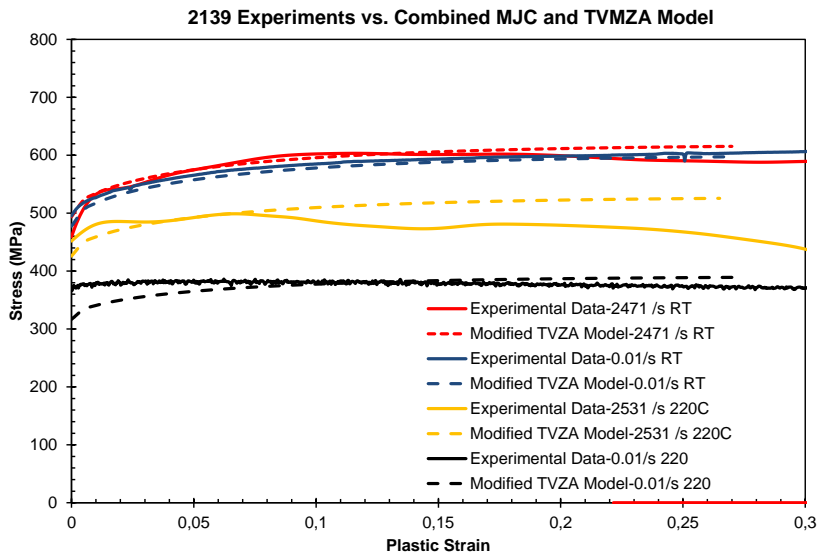
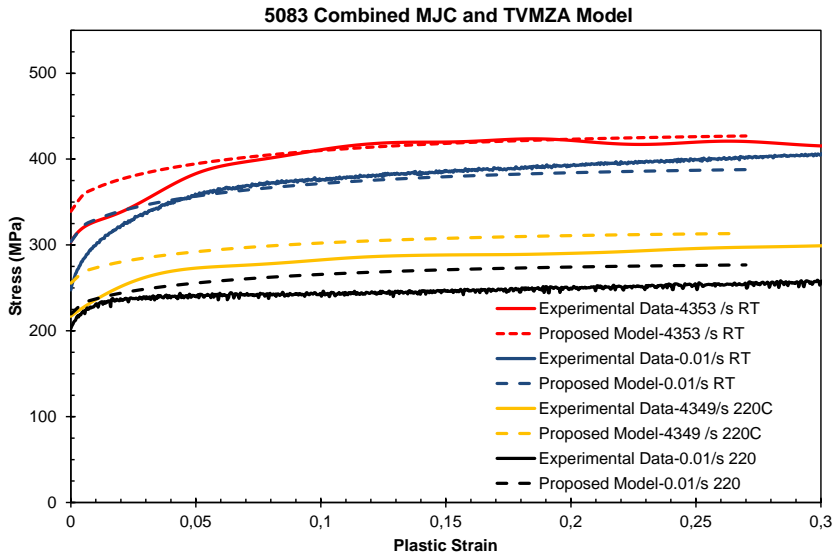


Figure 5.21 Flow stress versus strain for 5083 and 2139 at different strain rates and temperatures: experimental data versus the prediction of combined MJC and TVMZA model.

It is clearly seen from Figures 5.19, 5.20 and 5.21 that proposed model seems to provide a significantly better fit to the experimental data.

By this modification to TVMZA, the proposed model satisfactorily predicts the material behavior of aluminum alloys and captures the complex interaction of temperature and strain rate. Moreover,  $D$  parameter in the new model signifies a

material's propensity to thermal softening as a result of adiabatic deformation conditions at high strain rates. In this perspective, its value may become an important indication of a material's propensity to adiabatic shear failure since thermal softening is the main driver for the onset of localized shear instabilities in dynamic deformation processes. So, one can conclude that 2139 alloy has almost zero drop in flow stress due to thermal softening as it is seen in Table 5.7. The other alloys have the higher drop value in SRS.

Table 5.7 Coefficient of drop in flow stress in dynamic regime

Model Parameters	5083	7039	2519	2139
<i>D</i>	-0.2	-0.28	-0.16	-0.07

It is interesting to note that 2139 alloy has the highest ballistic performance among these alloys. The lower *D* value for 2139 is also consistent with lower propensity of this alloy to adiabatic shear banding as demonstrated in Figures 4.15-4.18. Although it is premature at this point to be fully conclusive, the new perspective in the proposed model, where increased thermal softening rate at elevated temperatures partly nullify the effect of strain rate hardening in dynamic regime, may also be used to assess the potential of a material in high strain rate applications such as terminal ballistics.



## CHAPTER 6

### SUMMARY AND CONCLUSIONS

Overall objective of current study is to investigate the dynamic behavior of high performance aluminum alloys (2139-T8, 5083-H131, 2519-T87 and 7039-T64) commonly used in lightweight armored military vehicles in a comparative manner and establish a robust experimental database as well as constitutive models to describe their dynamic response over a wide range of strain rates and temperatures typically encountered in penetration and impact events. To achieve this goal, an extensive experimental program has been undertaken that involved fully instrumented quasi-static and high strain rate experiments at both room temperature and elevated temperatures by using a series of servo-hydraulic test frames and state-of-the-art split Hopkinson pressure bar (SHPB) setups along with a high-speed data acquisition system. A brief summary of major findings and conclusions is presented in following subsections.

#### **6.1 Quasi-static and High Strain Rate Experiments**

An extensive set of experiments were conducted over a wide range of strain rates from  $10^{-3}$  to  $10^4$  s<sup>-1</sup> and varying elevated temperatures from room temperature to 370 °C. Then the strain hardening, strain rate hardening and thermal softening characteristics for each aluminum alloy were evaluated to develop a comprehensive analysis of their dynamic deformation behavior. Within this work, totally 669 experiments were conducted at various strain rates and temperatures. The main conclusions drawn from these experiments are presented as follows:

(1) An increasing in temperature significantly decreases the flow stress of all aluminum alloys. As the deformation temperature rises, the thermal activation energy that favors overcoming short-range barriers to dislocation motion increases,

while the stress needed to overcome these obstacles decreases monotonically as expected. However, the thermal softening of aluminum alloys seems to follow a power law dependence in the temperature range investigated rather than an exponential dependence that appears in some physically based models.

(2) Increasing temperature also affects the strain hardening behavior of alloys by decreasing and eventually completely eliminating strain hardening capacity. For example, strain hardening is not observed at 220 °C for 5083 and 7039 and similarly at 170 °C for 2519 and 2139 where a transition from strain hardening to almost elastic-perfectly plastic behavior occurs. Such a transition indicates the onset of dynamic recovery at the beginning of plastic deformation at these temperatures leading to an equilibrium between the rates of dislocation multiplication and annihilation, which results in a stress plateau. As the temperature goes up to 370 °C degrees, increased thermal energy further helps dislocation motion, thereby further reducing the flow stress. Some strain softening observed particularly in 2519 and 2139 alloys above 170 °C degree indicates the existence of severe dynamic recovery of the dislocations and even dynamic recrystallization (DRX), which effectively decreases the density of dislocations with increasing strain. This is considered to be an important finding because this experimentally observed strong coupling of strain hardening capacity with temperature is not adequately implemented in existing constitutive models.

(3) Temperature dependent flow stress curves also provide the necessary data to model the thermal softening behavior of these aluminum alloys. The experimental data obtained from these curves allow us to determine the athermal stress component for each alloy as the flow stress asymptotically approaches a plateau value at the high end of the temperature range investigated. The resulting thermal softening behavior for each alloy was used in modeling the thermal softening component of constitutive modeling effort.

(4) 5083 alloy has slight negative strain rate sensitivity (nSRS) while the other alloys (7039, 2519 and 1239) have strain rate insensitivity in quasi-static regime at room temperature. Mechanical response of 5083 also shows evidence of serrated

flow which is one of the common results of Dynamic Strain Aging (DSA) in 5xxx series of aluminum alloys. Interestingly, however, the negative strain rate sensitivity observed in 5083 disappears at elevated temperatures, suggesting that thermally activated dislocation kinetics dominates the mechanical response at higher temperatures rather than the diffusion controlled DSA which is dominant at low temperatures.

(5) Although none of the aluminum alloys showed any strain rate hardening in quasi-static loading regime at room temperature, the flow stress increases with increasing strain rate at the elevated temperature of 220 °C, showing a positive strain rate sensitivity (SRS). As the temperature is increased, flow stress required to overcome short-range barriers gradually decreases because of the increase in thermal activation energy. What this means is that the plastic flow process is increasingly governed by thermally activated mechanisms in which both the temperature and the strain rate are two important players. Therefore, strain rate hardening is observed at this elevated temperature even though it doesn't exist at room temperature. This constitutes another important experimental finding because temperature dependence of strain rate sensitivity is not accounted for in any of existing material models.

(6) In dynamic regime, all of the materials exhibited almost the same trend in their strain rate sensitivity such that although there was very mild strain rate sensitivity in the range of strain rates from  $10^{-3}$  to  $10^4 \text{ s}^{-1}$  the strain rate hardening significantly increased above  $10^4 \text{ s}^{-1}$ . This behavior is attributed to the argument that the deformation mechanism at lower strain rates is dominated by thermally activated dislocation motion while it is governed by dislocation drag mechanism at higher strain rates. Although it is experimentally observed, this change in rate controlling mechanism beyond a critical strain rate is not always considered in constitutive models.

(7) Test results establish a strong coupling of strain rate sensitivity (SRS) with temperature. All alloys exhibit the same dramatic decrease in flow stress at elevated temperatures as expected from the thermal softening behavior. However, at elevated

temperatures (220 °C), SRS observed in the range of strain rates from  $10^{-3}$  to  $10^4$  s<sup>-1</sup> was not only much higher than the one observed at room temperature but also comparable to the SRS at strain rates beyond  $10^4$  s<sup>-1</sup>. This finding is quite interesting because this experimentally observed SRS-temperature coupling is not addressed at all in existing constitutive models and remain to be the major source of their poor performance in quasi-static loading regime.

(8) Another important observation from the experimental data is that, unlike in quasi-static regime, strain rate sensitivity seems to be almost the same in dynamic loading regime irrespective of deformation temperature, although the flow stresses are significantly lower at elevated temperature. This behavior is in line with the underlying dislocation drag mechanism operating in this regime where the rate of hardening is proportional to the rate of deformation.

## 6.2 Constitutive Modeling

Five constitutive models were selected and their performances were investigated by using the results of experiments performed in this study. Plastic flow prediction of phenomenological (Johnson-Cook, Modified Johnson-Cook) and physics-based (Zerilli-Armstrong, Modified Zerilli-Armstrong, Turkkan-Vural Modified Zerilli-Armstrong) models were evaluated at varying temperatures and strain rates. The parameters of each constitutive model were calculated by using the experimental database established for aluminum alloys used in current study. Although some models (particularly the modified versions) performed much better than others, none of them was found to have a satisfactory predictive capability to capture the complex coupled behavior of aluminum alloys considered in this study. Therefore, a new modified ZA model was proposed in order to predict the rate and temperature dependent mechanical response of aluminum alloys. The following conclusions are drawn from the comparison of most commonly used constitutive models and their modified versions with the experimental data base generated in this study:

(1) Model verification studies and performance evaluation of results concluded that no single phenomenological or physically based model was developed and



introduced in literature which would successfully describe the mechanical behavior of aluminum alloys over a wide range of strain rates and temperatures.

(2) Failure of existing basic models stems from not only the lack of temperature coupling in strain hardening and strain rate hardening terms but also from using (or resulting in) a single SRS parameter, which results in failure to capture the strain rate effects in full spectrum of quasi-static and dynamic loading regimes. Some of these problems were addressed in modified versions of models; however, none of the modified models fully resolves these issues.

(3) To fulfill this gap, a modified model is proposed in this study by combining the salient features of MJC and TVMZA models. The model developed in this work has been proven to give a marked higher accuracy in capturing the experimental data in both quasi-static and dynamic regimes at both RT and elevated temperatures than JC, MJC, ZA, MZA and TVMZA models.

(4) Proposed model which is a modification to TVMZA and MJC models eliminates the shortcomings of currently available models by taking into account the temperature coupling of strain rate sensitivity in quasi-static regime where thermally activated dislocation glide is the dominant rate controlling mechanism.

(5) Additionally, a new parameter introduced in the proposed model represents a material's propensity to thermal softening as a result of adiabatic deformation conditions at high strain rates. In this perspective, its value may be used as an important indication of a material's propensity to adiabatic shear failure since thermal softening is the main driver for the onset of localized shear instabilities in dynamic deformation processes.

### **6.3 Adiabatic Shear Localization**

This study has also led to a detailed characterization of aluminum alloy armor materials' tendency to shear localization in the form of adiabatic shear bands (ASB) by using shear-compression specimens (SCS) in controlled dynamic experiments

followed by detailed microstructural examination. Analysis of shear localization curves obtained for each alloy along with post-mortem microstructural observations by optical microscopy resulted in the following conclusions;

(1) Dynamically loaded aluminum alloys exhibit three distinct deformation stages as the dynamic loading progresses. In the 1<sup>st</sup> stage, shear deformation is uniform with no sign of shear localization. In the 2<sup>nd</sup> stage, the signs of non-uniform shear are observed first in the form of large scale bends in otherwise uniform shear field. As the deformation continues further, towards the end of stage 2, localized shear bands of very small thickness starts developing at the sites of stress concentration. Finally in stage 3, these highly localized shear bands show signs of dynamic recrystallization (DRX), which is also taken as an indication of significant local temperature rise, and appear as white lines after chemical etching, which indicates severely localized shear. Adiabatic shear band(s) rapidly propagates and evolves to shear cracks by the end of stage 3.

(2) Equivalent stress-strain curves (also called shear localization curves) obtained from dynamically loaded SCSs can be conveniently used to determine macroscopic strain points ( $\epsilon_1$  and  $\epsilon_2$ ) separating these different deformation stages and also to extract some useful quantitative data that help and guide us in the assessment of shear localization behavior. These curves exhibit an initial strain hardening phase where flow stress increases with macroscopic strain until it reaches a maximum. This phase coincides with the 1<sup>st</sup> stage of uniform deformation. This is followed by a mild strain softening phase which indicates the formation of deformation instabilities in underlying microstructure and marks the 2<sup>nd</sup> stage of deformation as determined from post-mortem optical microscopy. The final phase in shear localization curves is characterized by a sudden and rapid increase in strain softening which is completely in line with the shear failure. The ease of determination of these phases (corresponding to distinct deformation stages) from shear localization curves provides a unique opportunity as it makes it possible to observe the progression of adiabatic shear banding from macroscopic curves without consulting to arduous post-mortem microscopy.

(3) While 5083, 7039 and 2519 alloys exhibit transformed shear bands (white shear bands) in stage 3 as a result of highly localized shear bands, 2139 alloy exhibits no sign of highly localized shear bands in stage 3 although some degree of localization is observed at the end of stage 2. Thus it can be concluded that 2139 has the lowest propensity to adiabatic shear localization since the homogenous deformation continues throughout the 2<sup>nd</sup> stage and there is no apparent shear localization. This lower propensity of 2139 to adiabatic shear localization is also considered to be one of the reasons for its higher ballistic performance.

#### **6.4 Concluding Remarks**

The use of high performance aluminum alloys in Army vehicles and structures is one of the most efficient ways to increase mobility and deployability. Deformation of these materials in army applications such as fragment impact, projectile penetration and air blast/shock waves involves high strain rates, large strains and rapid changes in temperature due to thermoplastic heating and often adiabatic deformation conditions. Therefore, design, analysis and optimization of components against military threats require development and use of robust constitutive models with reliable predictive capability under severe loading conditions. Although it is possible to computationally simulate and analyze these high speed terminal ballistics problems with today's computational power and advanced FE analysis codes, it is important to recognize that predictive capability of material constitutive models remains to be the bottleneck in the reliability of these simulations. Another important point is that even a good constitutive model may perform rather poorly if it cannot be well calibrated due to lack of high quality and relevant experimental data.

With this perspective in mind, the goal of current study was twofold. First, to establish a robust and extensive experimental database for aluminum alloys commonly used in lightweight armored vehicles (such as 2139-T8, 2519-T87, 5083-H131 and 7039-T64) in a wide range of strain rates and temperatures. This is important because generating such a database has a pivotal role not only in understanding the rate and temperature dependent mechanical response of materials

but also in calibrating existing models as well as developing new ones. Unfortunately, such databases are not shared in open literature as they are often produced and kept confidential by military or subcontracted private research labs. Second, by using this database, to conduct a comparative performance analysis of some selected constitutive models which are most commonly used and easily implemented in non-linear finite element codes such as AUTODYN, LS-DYNA, ABAQUS and ANSYS Explicit.

Both of these goals have been accomplished by generating a really extensive database for a wide range of strain rates and temperatures, and comparing the predictive capability of five different constitutive models against this database. The results show that majority of these models fails to capture rather complex behavior of high performance aluminum alloys. In particular, strong coupling of temperature with strain hardening and strain rate sensitivity that are experimentally observed in these alloys is not adequately incorporated into the mathematical structure of studied constitutive models. The strengths and weaknesses of each model have been exemplified and critically evaluated throughout the study by comparing predictions with experimental results. Furthermore, a new modified model is proposed in this study by combining the salient features of MJC and TVMZA models. This model has been proven to give a marked higher accuracy in capturing the experimental data in both quasi-static and dynamic regimes at both RT and elevated temperatures than JC, MJC, ZA, MZA and TVMZA models.

## CHAPTER 7

### RECOMMENDATIONS FOR FUTURE WORK

Although this study covers investigation in the dynamic behavior of high performance aluminum alloys over a wide range of strain rates and temperatures, with proposing a single constitutive model based on a robust experimental database, further investigation is needed for the other metals having different lattice structure such as BCC metals to correlate the proposed model.

There is also a need for further understanding of material's tendency to shear localization by observing the ASB microstructure of SCS that is pre-strained at elevated temperature. It should also cover a correlation study with local temperature rise due to thermoplastic heating.

Additionally, modern techniques such as the use of artificial neural network models should also be studied together with experimental data in order to predict dynamic behavior of material.

Finally, it needs to add a softening term to constitutive models resulting from adiabatic shear localization after critical strain.



## REFERENCES

- [1] A. Doig, *Military Metallurgy*. London: IOM Communication Ltd, 1998, p. 147.
- [2] Committee on Opportunities in Protection Materials Science and Technology for Future Army, *Opportunities in Protection Materials Science and Technology for Future Army Applications*. National Academies Press, 2011, p. 176.
- [3] B. E. Placzankis and E. A. Charleton, “Accelerated corrosion and adhesion assessments of CARC prepared aluminum alloy 2139-T8 using three various pretreatment methods and two different primer coatings,” 2009.
- [4] M. Vural and S. Tin, “Interim Progress Report for Award W911NF-10-1-0152,” 2012.
- [5] D. D. Showalter, B. E. Placzankis, and M. S. Burkins, “Ballistic Performance Testing of Aluminum Alloy 5059-H131 and 5059-H136 for Armor Applications,” no. May, 2008.
- [6] S. A. G. Thomas D. Wolfe, “Weldability of 2219-T851 and 2519-T87 Aluminum armor alloys for use in army vehicle systems,” *U.S. Army Lab. Mater. Technol. Rep.*, 1987.
- [7] E. S. C. Jonathan S. Montgomery, “Next Generation of Metallic Armor Leads the Way,” *AMCPTIAC Q.*, vol. 8, no. 4, 2004.
- [8] J. R. Fisher Jr., J.J., Kramer L.S. and Pickens, “Aluminum alloy 2519 in military vehicles.” *Advanced Materials & Process*, pp. 43–46.

- [9] B. Cho, A. and Bes, “Damage Tolerance Capability of an Al-Cu-Mg-Ag Alloy (2139).” *Mater. Sci. Forum*, pp. 603–608.
- [10] M. Vural and J. Caro, “Experimental analysis and constitutive modeling for the newly developed 2139-T8 alloy,” vol. 520, pp. 56–65, 2009.
- [11] J. D. Clayton, “Modeling effects of crystalline microstructure , energy storage mechanisms , and residual volume changes on penetration resistance of precipitate-hardened aluminum alloys,” *Compos. Part B*, vol. 40, no. 6, pp. 443–450, 2009.
- [12] M. A. Z. Elkhodary, K., Sun, L., Irving, D.L., Brenner, D.W., Ravichandran, G., “Integrated Experimental , Atomistic , and Microstructurally Based Finite Element Investigation of the Dynamic Compressive Behavior of 2139,” *J. Appl. Mech.*, vol. 76, no. September, pp. 1–9, 2009.
- [13] J. M. Boteler and D. P. Dandekar, “Dynamic Response of 5083-H131 Aluminum Alloy,” in *American Institute of Physics*, 2007, pp. 481–485.
- [14] S. J. Pérez-bergquist, G. T. R. G. Iii, E. K. Cerreta, C. P. Trujillo, and A. Pérez-bergquist, “The dynamic and quasi-static mechanical response of three aluminum armor alloys : 5059 , 5083 and 7039,” vol. 528, pp. 8733–8741, 2011.
- [15] K. A. Dannemann, S. Chocron, C. E. Anderson, and T. Tardec, “Comparison of Mechanical and Constitutive Response for Five Aluminum Alloys for Armor Applications,” San Antonio, TX, USA, 2010.
- [16] Z. Xin-ming, L. I. Hui-jie, L. I. Hui-zhong, G. A. O. Hui, G. A. O. Zhi-guo, L. I. U. Ying, L. I. U. Bo, and M. Science, “Dynamic property evaluation of aluminum alloy 2519A by split Hopkinson pressure bar,” pp. 1–5, 2007.
- [17] G. Johnson, “Model Behavior,” *Technology Today*, Spring 2009 pp. 2–5.
- [18] Donald J. Sandstrom, “Armor and Anti-Armor materials by design,” *Los Alamos Science Summer*, pp. 36–50, 1989.



- [19] M. A. Meyers, *Dynamic Behavior Materials*. John Wiley and Sons, 1994.
- [20] K. T. Ramesh, *Springer Handbook of Experimental Solid Mechanics Chapter 33 "High Strain Rate and Impact Experiments."* Springer, 2008, p. 1098.
- [21] O. Vohringer, "Deformation Behavior of Metallic Materials," *Int. Summer Sch. Dyn. Behav. Mater. ENSM, Nantes*, p. 7.
- [22] R. O. Smerd, "Constitutive Behavior of Aluminum Alloy Sheet at High Strain Rates," University of Waterloo, 2005.
- [23] P. S. Follansbee and G. T. Gray, "Dynamic deformation of shock prestrained copper," *Mater. Sci. Eng. A*, vol. 138, no. 1, pp. 23–31, May 1991.
- [24] U. F. K. Follansbee, P. S., "A constitutive description of the deformation of Copper based on the use of the mechanical threshold stress as an internal state variable," *Acta Mater.*, vol. 36, no. 1, pp. 81–93, 1988.
- [25] A.V. Granato, *Metallurgical Effects at High Strain Rates (edited by R. W.Hohde B. M. Butcher J. R. Holland C.H.Karnes)*. New York, 1973, p. 255.
- [26] F. E. H. and J. E. D. A. Kumar, "No Title," *Acta Met.*, vol. 16, p. 1189, 1968.
- [27] A. Rusinek and J. A. Rodríguez-Martínez, "Thermo-viscoplastic constitutive relation for aluminium alloys , modeling of negative strain rate sensitivity and viscous drag effects," *Mater. Des.*, vol. 30, no. 10, pp. 4377–4390, 2009.
- [28] Tonu Leemet, "The Characterization and Modeling of the Dynamic Behavior of Hard-to-Machine Alloys," Riga Technical University, 2012.
- [29] Y. B. Dodd, Bradley, *Adiabatic Shear Localization*, Second edi. Elsevier Ltd., 2012, p. 454.
- [30] C. Zener and J. H. Hollomon, "Effect of Strain Rate Upon Plastic Flow of Steel," vol. 22, 1944.

- [31] H. C. Rogers, “Adiabatic Plastic Deformation,” *Annu. Rev. Mater. Sci.*, vol. 9, pp. 283–311, 1979.
- [32] C. C. and Y. S. Bai Yilong, “On Evolution of Thermo-Plastic Shear Band,” *ACTA Mech. Sin.*, vol. 2, no. 1, pp. 1–7, 1986.
- [33] S. S. J. Donald E. Carlucci, *Ballistics Theory and Design of Guns and Ammunition*. CRC Press, 2008, p. 495.
- [34] L. E. Murr, A. C. Ramirez, S. M. Gaytan, M. I. Lopez, E. Y. Martinez, D. H. Hernandez, and E. Martinez, “Microstructure evolution associated with adiabatic shear bands and shear band failure in ballistic plug formation in Ti–6Al–4V targets,” *Mater. Sci. Eng. A*, vol. 516, no. 1–2, pp. 205–216, Aug. 2009.
- [35] L. Chen, Y. Li, and L. Wang, “A computational investigation of adiabatic shear plugging based on thermo-viscoplastic instability,” *Acta Mech.*, vol. 126, pp. 127–138, 1998.
- [36] Patrice Longère and André Dragon, *Adiabatic Shear : Pre- and Post-critical Dynamic Plasticity Modelling and Study of Impact Penetration . Heat Generation in this Context*, no. January. 2010, pp. 233–262.
- [37] J. Duffy, “Experimental Studies of Shear Band Formation Through Temperature,” *J. Phys. IV*, vol. 1, pp. 3–10, 1991.
- [38] A. Marchand and J. Duffy, “An experimental study of the formation process of adiabatic shear bands in a structural steel,” *J. Mech. Phys. Solids*, vol. 36, no. 3, pp. 251–283, Jan. 1988.
- [39] Tusit Weerasooriya, “The MTL Torsional Split-Hopkinson Bar.”, Materials Dynamics Branch, U.S. Army Materials Technology Laboratory, May 1990
- [40] D. Ñ. Rittel, Z. G. Wang, and A. Dorogoy, “Geometrical imperfection and adiabatic shear banding,” vol. 35, pp. 1280–1292, 2008.

- [41] B. B. Hopkinson, "A Method of Measuring the Pressure Produced in the Detonation of High Explosives or by the Impact of Bullets," *Phil. Trans., Royal Soc London, Ser. A*, pp. 411–413, 1913.
- [42] R.M. Davies, "A critical Study of the Hopkinson Pressure Bar," *Philos. Trans. R. Soc. London, Ser. A*, vol. 240, no. 821, pp. 375–457.
- [43] H. Kolsky, "An Investigation of the Mechanical Properties of Materials at very High Rates of Loading," *Proc. Phys. Soc. London, Sect. B*, no. 62, pp. 676–700, 1949.
- [44] G. T. (Rusty) Gray, *Characterization of Materials*, vol. 1, no. 1. Hoboken, NJ, USA: John Wiley & Sons, Inc., 2002, pp. 288–301.
- [45] D. Rittel, S. Lee, and G. Ravichandran, "A Shear-compression Specimen for Large Strain Testing," *Exp. Mech.*, vol. 42, no. 1, pp. 58–64, 2002.
- [46] D. Rittel, G. Ravichandran, and S. Lee, "Large strain constitutive behavior of OFHC copper over a wide range of strain rates using the shear compression specimen," *Mech. Mater.*, vol. 34, pp. 627–642, 2002.
- [47] N. B. M. Vural, A. Molinari, "Analysis of Slot Orientation in Shear-Compression Specimen (SCS)," *Exp. Mech.*, vol. 51, pp. 263–273, 2010.
- [48] W. H. C. Johnson, G R, "Constitutive Model and Data for Metals Subjected to Large Strains, High Strain Rates and High Temperatures," in *7th Int. Symp. on Ballistics*, 1983.
- [49] H. O. K. K. Marc André Meyers, Ronald W. Armstrong, *Chapter 14 Dynamic Deformation and Failure in Mechanics and Materials: Fundamentals and Linkages*. New York: John Wiley and Sons, 1999, pp. 489–594.
- [50] Meyers and Chawla, *Mechanical Behavior of Materials*. New York: Cambridge University Press, 2009.

- [51] F. J. Zerilli and R. W. Armstrong, “Dislocation mechanics based constitutive relations for material dynamics calculations,” *J. Appl. Phys.*, vol. 61, no. 5, pp. 1816–1825, 1987.
- [52] F. J. Zerilli, “Dislocation Mechanics – Based Constitutive Equations,” *Metall. Mater. Trans. A*, vol. 35, pp. 2547–2555.
- [53] A. R. W. Zerilli, Frank J, “Dislocation Mechanics Based Constitutive Equation Incorporating Dynamic Recovery and Applied to Thermomechanical Shear Instability,” *AIP Conf. Proc.*, vol. 429, pp. 215–218, 1997.
- [54] R. W. Armstrong and F. J. Zerilli, “Dislocation Mechanics Based Analysis of Material Dynamics Behavior,” *J. Phys.*, vol. 49, no. 9.
- [55] G. I. Taylor, “The Mechanism of Plastic Deformation of Crystals. Part I. Theoretical,” *Proc. R. Soc. A Math. Phys. Eng. Sci.*, vol. 145, no. 855, pp. 362–387, Jul. 1934.
- [56] G. I. Taylor and H. Quinney, “The Latent Energy Remaining in a Metal after Cold Working,” *Proc. R. Soc. A Math. Phys. Eng. Sci.*, vol. 143, no. 849, pp. 307–326, Jan. 1934.
- [57] P. S. Follansbee, “Rate Dependence of structure evolution in Copper and its influence on the stress-strain behavior at very high strain rates,” in *IMPACT’87 International Conference on Impact Loading and Dynamic Behavior of Materials*, 1987.
- [58] O. Anil Turkkan, “Rate and Temperature Dependent Material Response and Modeling of Al-Cu Alloy Systems Leading to Al2139-T8 Armor Material,” Illinois Institute of Technology, 2013.
- [59] R. E. Sanders, “Technology Innovation in Aluminum Products,” *JOM*, vol. 53, no. 2, pp. 21–25, 2001.

- [60] K. Doherty, R. Squillacioti, B. Cheeseman, B. Placzankis, and D. Gallardy, “Expanding the Availability of Lightweight Aluminum Alloy Armor Plate Procured From Detailed Military Specifications,” 2012.
- [61] J. C. Benedyk, “International Temper Designation Systems for Wrought Aluminum Alloys: Part I-Strain Hardenable Aluminum Alloys,” *Light Met. Age*, pp. 26–30.
- [62] Joseph C. Benedyk, “International Temper Designation Systems for Wrought Aluminum Alloys: Part II-Thermally Treated Aluminum Alloys,” *Light Met. Age*, pp. 16–22.
- [63] Sia Nemat-Nasser, *High Strain Rate Tension and Compression Tests in Mechanical Testing and Evaluation of ASM Handbook*. ASM International, 2000.
- [64] B. S. Weinong W. Chen, *Split Hopkinson (Kolsky) Bar Design, Testing and Applications*. New York: Springer, 2011.
- [65] G. F. Vander Voort and E. P. Manilova, “Metallographic Etching of Aluminum and Its Alloys.”
- [66] T. Zweg, “A Universal Method for the Mechanical Preparation of Aluminium Alloy Specimens with High Edge Retention and their Subsequent Colour Etching,” *Prakt. Metallogr.*, vol. 38, no. 2, pp. 3–6, 2001.
- [67] A. P. Dominique Francois, *Mechanical Behavior of Materials*. Springer.
- [68] M. Wagenhofer, M. Erickson, R. W. Armstrong, and F. J. Zerilli, “Influences of Strain Rate and Grain Size on Yield and Serrated Flow in Commercial Al-Mg Alloy 5086,” vol. 41, no. 11, pp. 1177–1184, 1999.
- [69] T. Naka and F. Yoshida, “Deep drawability of type 5083 aluminium ± magnesium alloy sheet under various conditions of temperature and forming speed,” vol. 90, pp. 19–23, 1999.

- [70] R. C. Picu, G. Vincze, F. Ozturk, J. J. Gracio, F. Barlat, and A. M. Maniatty, "Strain rate sensitivity of the commercial aluminum alloy AA5182-O," vol. 390, pp. 334–343, 2005.
- [71] W. A. Curtin, D. L. Olmsted, and L. G. H. Jr, "A predictive mechanism for dynamic strain ageing in aluminum–magnesium alloys," *Nat. Mater.*, vol. 5, no. November, pp. 875–880, 2006.
- [72] A. Benallal, T. Berstad, T. Børvik, O. Hopperstad, and R. N. De Codes, "On the Measurement and Evaluation of the Width of Portevin – Le Chatelier Deformation Bands with Application to AA5083-H116," pp. 329–338.
- [73] William F. Hosford, *Mechanical Behavior of Materials*. Cambridge University Press, 2005.
- [74] G. T. (Rusty) Gray, "High-Strain-Rate Deformation : Mechanical Behavior and Deformation Substructures Induced," *Annu. Rev. Mater. Res.* 2012., no. 42, pp. 285–303, 2012.
- [75] D.R. Lesuer, G.J. Kay, M.M. LeBlanc, "Modeling Large-Strain , High- Rate Deformation in Metals," *Third Bienn. Tri-Laboratory Eng. Conf. Model. Simulation, Pleasanton, CA,*.
- [76] E.L. Huskins, B. Cao, and K.T. Ramesh, "Strengthening mechanisms in an Al – Mg alloy," vol. 527, pp. 1292–1298, 2010.
- [77] Y. B. Xu, W. L. Zhong, Y. J. Chen, L. T. Shen, Q. Liu, Y. L. Bai, and M. A. Meyers, "Shear localization and recrystallization in dynamic deformation of 8090 Al – Li alloy," vol. 299, pp. 287–295, 2001.
- [78] Vili Panov, "Modelling of Behaviour of Metals at High Strain Rates," Cranfield University, 2005.
- [79] M. Vural, D. Rittel, and G. Ravichandran, "Large Strain Mechanical Behavior of 1018 Cold-Rolled Steel over a Wide Range of Strain Rates," *Metall. Mater. Trans. A*, vol. 34, no. December, pp. 2873–2885, 2003.

- [80] K. Domkin, "Constitutive models based on dislocation density Formulation and implementation into finite element codes," Luleå University of Technology, 2005.
- [81] F. H. Abed and G. Z. Voyiadjis, "A consistent modified Zerilli-Armstrong flow stress model for BCC and FCC metals for elevated temperatures," *Acta Mech.*, vol. 175, no. 1–4, pp. 1–18, Feb. 2005.

## CIRRICULUM VITAE

Surname, Name: Macar, Mehmet

Nationality: Turkish (TC)

Date and Place of Birth: 01.01.1971, Çorum

Marital Status: Married, a daughter and two sons

Cell Phone: (505) 787497

email: [mmacar@kho.edu.tr](mailto:mmacar@kho.edu.tr)

### EDUCATION

- 2013 – 2014 : Visitor Researcher in Illinois Institute of Technology, IL, USA  
1996 – 1999 : M.Sc. in Mechanical Engineering, Sakarya University, Sakarya  
1989 – 1994 : B.S. in Mechanical Engineering, METU, Ankara  
1985 – 1989 : Maltepe Military High School, İzmir

### CAREER

- 11/1994 - 05/1996 :Manager of Track Plant in 1<sup>st</sup> Base Maintenance Center  
Command, Sakarya  
05/1996 - 04/1999 :Manager of Main Battle Tank Plant in 1<sup>st</sup> Base Maintenance  
Center Command, Sakarya  
04/1999 - 07/2005 :R&D Manager of Vehicle Development in 1<sup>st</sup> Base Maintenance  
Center Command, Sakarya  
-Turkish Self-Propelled Howitzer Programme R&D Manager  
07/2005 – 05/2011 :Program Manager in Turkish Land Forces Command, Ankara  
- HK-33E Assault Rifle  
- 40 mm Grenade Launcher  
- Turkish Self-Propelled Howitzer  
- Ammunition Resupply Vehicle  
- Ammunition Surveillance Plant Modernization  
06/2011- Military Academy, Ankara